REVIEW

Check for updates

Two-dimensional layered metal oxides (2D LMOs) for next-generation electronic devices

Arpit Verma, [ID] * Alka Rani and Bal Chandra Yadav [ID] *

Two-dimensional layered metal oxides (2D LMOs) have emerged as a rapidly growing class of materials that combine the advantages of reduced dimensionality with the functional diversity of transition metal oxides. Their high surface-to-volume ratio, structural anisotropy, tunable bandgap, and variable oxidation states endow them with unique electrical, optical, and catalytic properties. Recent advances in atomic layer deposition, vapor-phase synthesis, and liquid-phase exfoliation have enabled the scalable fabrication of high-quality 2D LMOs with controlled stoichiometry and thickness. This review provides a comprehensive overview of their structure–property relationships, charge transport mechanisms, and interfacial phenomena, emphasizing how defect engineering, quantum confinement, and interlayer coupling can be exploited to tailor their performance. The integration of 2D LMOs into van der Waals heterostructures further enhances band alignment, charge transfer, and excitonic control, unlocking new opportunities for transistors, sensors, and spintronic and optoelectronic devices. Current challenges such as environmental stability, phase control, and large-scale processability are critically assessed. Finally, emerging computational and machine learning-guided approaches are discussed as pathways to accelerate the rational design of 2D LMOs for flexible, energy-efficient, and multifunctional electronic applications.

1. Introduction

With distinct mechanical, electrical, and structural characteristics, two-dimensional (2D) materials have attracted a great deal of scientific attention.[1] Unlike bulk materials, 2D materials solely depend on their surface characteristics, making their properties highly sensitive to substrate interactions, surface defects, and the presence of adatoms.[2,3] Their extreme thinness, combined with their intrinsic flexibility and mechanical strength, distinguishes them from conventional materials and enables novel functionalities. 2D materials exhibit exceptional characteristics including high electron mobility, tunable band structures, topologically protected states, and superior thermal conductivity, positioning them as promising candidates for next-generation technologies.[4] The continuous development of these materials is expected to revolutionize existing electronic and optoelectronic devices while unlocking new possibilities for spintronic applications and quantum computing.[2] Compared with other atomically thin materials, single or multilayer transition metal oxides have a relatively longer history. 2D LMOs contain a range of earth-abundant minerals that have been used for millennia as construction materials, lubricants, and pigments, among many other applications.[5] Strong interlayer ionic bondings are present in the majority of metal oxides. 2D metal oxides typically have dangling bonds introduced because of significant interlayer connections. This causes strong surface polarization, which causes surface instability.[6] The remarkable physical and chemical features of 2D metal oxides are the result of their structural reconstruction, electron confinement in 2D, and high surface-to-volume ratio. In addition, 2D LMOs exhibit a wide range of characteristics since they can adopt various binding arrangements.[6,7]

For the upcoming generation of electronic devices, 2D LMOs have emerged as one of the most promising materials. Because they are atomically thin, they offer ultra-thin device topologies with better performance and reduced energy consumption. Due to their high surface-to-volume ratio, which enhances control over electrical characteristics and makes surface functionalization easier, they are ideal for sensing and catalytic applications. The electrical properties of 2D LMOs can also be altered by layer stacking, doping, or straining. Their unique electronic band structure and high carrier mobility make them excellent choices for high-speed transistors, sensors, photodetectors, energy storage devices, and spintronic devices. However, scientists have not yet completely developed these materials in terms of their impact on the development of electronic devices as well as enhanced pooling and integration. These materials' powder can be exfoliated by sonication in appropriate solvents, and the exfoliated layers can then be removed by centrifugation. This approach aligns with classical solubility theory and

Nanomaterials and Sensors Research Laboratory, Department of Physics, Babasaheb Bhimrao Ambedkar University, Lucknow-226025, UP, India. E-mail: arpit20696@ gmail.com; balchandra_yadav@rediffmail.com

demonstrates high efficiency in solvents with Hildebrand solubility parameters near 21 $MPa^{1/2}$.[8] When smectite-type clay minerals were discovered to disperse well in water and produce a colloidal suspension as a result of spontaneous exfoliation or delamination, the history of nanosheets or exfoliated sheets began in the 1950s.[9,10] Since the 1970s, a variety of inorganic layered compounds, such as layered metal oxides, metal chalcogenides, and metal phosphates, have been exfoliated by using the right interlayer cations and solvents.[10–12] Resounding success of graphene has prompted a scientific interest in examining its analogues, including a vast variety of 2D materials like transition metal dichalcogenides (TMDCs), metal oxides, metal phosphates, and jarosites.[13] They show unique characteristics as a new class of nanoscale materials that are different from their bulk lamellar systems because of their limited thickness within a nanoscale range rather than a lateral dimension up to several tens of micrometers.[13]

Large specific surface areas seen in freestanding 2D nanoflakes allow for substantial contact with the environment even for little quantities of materials. Because there are fewer grain boundaries, 2D systems can enable more effective electron transport. They also often have superior mechanical stability.[14] The unusual optical, electrical, magnetic, and chemical characteristics of atomically thin 2D metal oxides make them a promising candidate for use in high-performance smart devices.[15] 2D metal oxide semiconductors (MOSs) can be broadly classified as either layered or non-layered based on their crystal structure. The study of physics in low-dimensional systems depends on nanosheets, a unique family of nanoscale materials, since 2D quantum confinement may result in interaction properties that vary from those of bulk lamellar systems.[10] Nanosheets have in fact steadily exhibited novel physical and chemical features like quantum confinement or surface impact.[10]

Through the selection of nanosheets and the coupling with heterogeneous species, sophisticated functionality or nanodevices may be rationally constructed with fine control over the synthetic organization on a molecular scale.[10] An MoS_2–MoO_3 hybrid nanomaterial synthesized by Yin *et al.* via heat-assisted partial oxidation of MoS_2 followed by annealing-driven crystallization has a p-type conductive nature.[16] When integrated into an n-SiC/p-MoS_2–MoO_3 heterojunction, the device exhibits multi-wavelength electroluminescence, demonstrating potential for optoelectronics, clean energy, and data storage applications. Crystalline α-MoO_3 belts were synthesized by Liu *et al.* via thermal vapor transport and exfoliated into 2D nanosheets using scotch-tape and bovine serum albumin (BSA)-assisted methods.[17] Raman analysis showed mode softening (5 cm^{-1}) of the Ag (818 cm^{-1}) vibration in monolayers, confirmed by DFT calculations, while BSA-exfoliated sheets displayed a blue-shifted absorption edge and an excitonic peak at 3.98 eV, demonstrating the potential for 2D α-MoO_3 lattice dynamics and optical studies. Two-dimensional nanomaterials exhibit unique electronic states arising from quantum confinement

Arpit Verma

Dr Arpit Verma is currently a Post-Doctoral Fellow at Aix-Marseille Université, France, in the Matériaux Divisés, Interfaces, Réactivité, ÉLectrochimie (MADIREL) laboratory, France. Prior to this, he served as a Post-Doctoral Research Associate at the Indian Institute of Technology (IIT) Ropar, India, from June 2024 to May 2025. He earned his PhD in Physics from Babasaheb Bhimrao Ambedkar University, Lucknow, India, in 2024, where he conducted his doctoral research in the Nanomaterials and Sensors Research Laboratory. He received his MSc degree in Applied Physics from the same university in 2018. His research focuses on the design and development of advanced materials, including electron and hole transport layers for high-efficiency perovskite solar cells, 2D materials, metallopolymers, and nanohybrid structures. His work emphasizes their applications in energy harvesting, photodetection, and chemical and biosensing technologies. He is a lifetime member of the Indian Science Congress Association and the Materials Research Society of India. Dr Verma has authored multiple peer-reviewed publications and remains actively engaged in interdisciplinary materials research.

Alka Rani

Ms Alka Rani received her MSc Physics degree from Bipin Bihari degree college (Bundelkhand University), Jhansi, UP, India in the year 2020. She is pursuing her PhD degree in the Nanomaterials and Sensors Research Laboratory, Department of Physics, under the supervision of Prof. B. C. Yadav from Babasaheb Bhimrao Ambedkar University, Lucknow, UP, India. She has been awarded a Joint CSIR-UGC Junior Research Fellowship (JRF) by the Government of India. Her area of research interest includes the synthesis and evaluation of optoelectronic properties of TMDCs, especially for energy conversion devices.

effects, reduced dielectric screening, and strong spin–orbit coupling. These properties enable tailored band structures, high charge carrier mobility, and exotic quantum phenomena, which are essential for applications in next-generation electronics, optoelectronics, energy storage, and quantum technologies.[18] In order to improve performance in energy applications, a magical combination of metal oxides and two-dimensionality produces amazing synergistic effects outside of the material itself. Thus, by merging 2D nanomaterials with electrical structure tailoring techniques, new developments in sustainable fuel generation and battery systems may be greatly accelerated.[18,19]

The development and prospects of 2D LMOs based on their structure, synthesis method, and potential for future electronic

Bal Chandra Yadav

Prof. (Dr) B. C. Yadav was born in Hardatt Nagar Girant, Shravasti, Uttar Pradesh, India. Prof. Yadav received his PhD degree in 2001 from the Department of Physics, University of Lucknow, India. Currently, he is Professor in the Department of Physics, School of Physical & Decision Sciences, Babasaheb Bhimrao Ambedkar University, Lucknow. Dr Yadav has worked as Head, Department of Physics, Department of Electronics and Communication

Engineering, Dean of various Schools and also as the Director of University Sophisticated Instrumentation Center (USIC). He is the recipient of prestigious Young Scientist Award-2005 awarded by the State Council of Science and Technology. Dr Yadav was also selected in 2011 for a Brain Pool International Fellowship of South Korea. He is the recipient of Research & Academic Excellence Awards for the year 2020, 2021, 2022, and 2023 by BBA University, Lucknow. He was also awarded for publishing papers in High Impact Factor Journals by BBA University, with an incentive grant of Rs. 2.00 lakhs, 10 June 2014. National Academy of Sciences, India, has nominated Dr Yadav as a member. He has been selected five times in the list of World's Top 2% Scientists by Stanford University, USA, for significant academic and research work. Prof. Yadav has published more than three hundred and fifty research/review papers in reputed international journals and authored two books. Dr Yadav has also guided 26 PhD, 03 MPhil and 13 MTech students. Dr Yadav has convened 03 International Conference/symposium, 01 National Conference and 01 National Workshop. His current interests of research also include the development of self-healing materials for energy harvesting devices, synthesis of metal oxides nanoparticles, metallopolymers, etc., characterizations and their applications as physical, chemical and biosensors. His current interests of research include the design and development of metal oxide nanoparticles, metallopolymers, nanohybrid materials, and self-healing materials, along with their applications as physical and chemical sensors, photosensors, flexible sensors, and energy-storing devices.

applications are covered in detail in this review paper. This review presents current obstacles to creating and using 2D LMOs, including property control, scalability, and stability. The structure, inherent characteristics, and synthesis processes which define 2D LMOs' functional diversity are also covered in this review. The review focuses on electronic tuning strategies that maximize the electrical, optical, and chemical functionality of these materials through morphology engineering (thickness engineering and pore ordering), defect engineering (lattice strain, amorphization, and vacancy control), and heterostructure engineering. The article also outlines a wide range of electronic and optoelectronic devices, including high-mobility electronics, high-k dielectrics, resistive switching devices, energy storage devices (like batteries and supercapacitors), thermoelectrics, spintronic devices, and gas/biosensors. These devices show the diversity and growing importance of 2D LMOs in basic science and technology applications. Finally, the review concludes by summarizing the accomplishments and proposing a line of future investigation to look beyond present-day borders and realize the complete potential of 2D LMOs for future electronic devices.

2. Current challenges in 2D LMOs

With their fascinating physical and chemical characteristics, 2D metal oxides have never stopped to astound us and reassure us of their promising future. However, in order to make them more interesting and diversified, a number of concerns relating to fundamental research and business obstacles must be resolved. A far wider variety of options for 2D materials are being constrained by the small number of parent materials with acceptable layered host crystals.[13] Co_3O_4 has drawn particular interest among the several 2D LMOs on the market due to its low toxicity, strong chemical stability, and high theoretical capacity. However, it has been difficult to employ in practice owing to its weak electrical conductivity, quick capacity loss, and poor capacity retention. To enhance their performance, several efforts have been made to hybridize Co_3O_4 with carbon-based materials. However, ternary $NiCoO_4$ has stronger electrical conductivity and electrochemical activity because it contains two distinct cations.[20] The manufacturing of 2D LMOs is made possible by subsequent electronics, although there are still a number of challenges to be solved. It is still challenging and expensive to mass-produce 2D LMOs of high quality. They must also be stable in various weather situations to be used properly. Minimizing contact resistance and integrating 2D LMOs with other materials are difficulties. Atomic design defects must be comprehended and managed if the material quality and device performance are to be improved. The on-going objective is to create cutting-edge characterization techniques to look into their nanoscale characteristics. More thorough and meticulous examinations are needed to have a better grasp of their nature and possible toxicity. The external fabrication challenges originate from processing and device integration aspects. These include substrate-induced strain, lattice mismatch, interfacial charge traps, and contamination introduced during synthesis or transfer processes.[21] Such factors often distort the lattice or

modify the band alignment at the interfaces, thereby suppressing carrier injection and altering device performance. These limitations are linked to the electronic structure and bonding characteristics of metal oxides. However, the external fabrication challenges stem from synthesis and device integration processes, including substrate-induced strain, lattice mismatch, interfacial charge trapping, and stoichiometric variations during thin-film deposition.[22] These extrinsic factors often degrade charge transport or alter band alignment at interfaces, affecting the overall device efficiency. By distinguishing between these two categories, the review highlights that addressing the performance bottlenecks of 2D LMOs requires a combined strategy improving their intrinsic properties through defect and phase engineering while mitigating external challenges through advanced fabrication control, interface optimization, and substrate engineering.

For 2D LMOs to fully affect the future of electronics, a number of challenges must be addressed. Due to its fascinating capabilities in energy storage and conversion, 2D nanostructured transition metal oxides, such as TiO_2, MnO_2, Co_3O_4, V_2O_5, and MoO_3, have gained significant attention as the next generation of 2D materials since the discovery of graphene.[23] The majority of metal oxides have poor electrical conductivity. RuO_2 is recognized as a metallic oxide with the greatest electrical conductivity up to 10^4 S cm^{-1} and is one of the potential candidates.[24] One of the main objectives of materials chemistry is to provide methods for accurately modifying nanoscale structures. The synthesis of structurally well-defined layered components, which can be essential for various applications, depends on achieving this kind of control. These include the design of tailored catalysts for enhanced reaction efficiencies, the fabrication of photonic band gap materials for advanced optical devices, the development of high-performance electronic components, and the creation of selective chemical separation systems. By fine-tuning nanoscale architecture, researchers can engineer materials with optimized properties, paving the way for innovations in energy, sensing, and quantum technologies.[25]

3. Two-dimensional layered metal oxides (2D LMOs): structure, properties and synthesis

Most of the 2D nanoflakes are created using solvothermal or hydrothermal processes. Hydrothermal and solvothermal synthesis both have the benefits of being straightforward, scalable, inexpensive, requiring low processing temperatures,
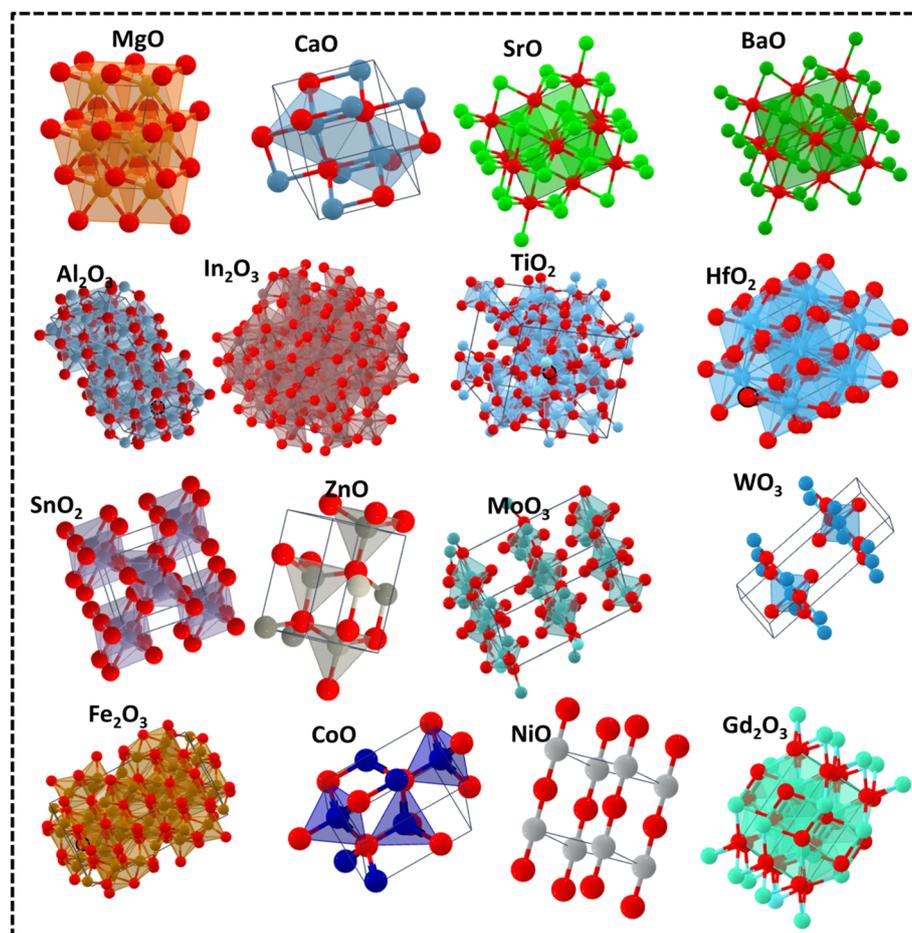

Fig. 1 Structures of some 2D metal oxides. Adopted from Material Project.[27,28]

and working with flexible substrates.[14] Fig. 1 provides a concise overview of the different structures of 2D LMOs. Generally, these materials are binary or complex oxides featuring one or more metallic elements, exhibiting diverse crystalline structures that consist of stacking monolayer *via* van der Waals interaction. The structures include ZnO, CaO, SnO, BaO, Al_2O_3, In_2O_3, TiO_2, HfO_2, SnO_2, ZnO, MoO_3, WO_3, Fe_2O_3, CoO, NiO and Gd_2O_3. Among the various liquid-exfoliation techniques, liquid-phase exfoliation stands out as one of the simplest and most effective methods. This approach involves sonicating stacked crystalline materials in specifically chosen stabilizing liquids, which help prevent re-aggregation and promote efficient exfoliation. Liquid-phase exfoliation has become a popular method for creating high-quality nanosheets for a variety of applications in electronics, energy storage, and catalysis because of its scalability, affordability, and compatibility with a broad range of layered materials.[8] Nanosheets that are stabilized against liquids, such as specific solvents or solvent blends, aqueous surfactant solutions, or polymer solutions, are produced by tendency to exfoliate the crystals by the sonic energy.[8] It is thought that solvent stabilization is simpler when solvents with the proper surface-energy or solubility characteristics interact with nanosheets through van der Waals interactions with a strength that is comparable to the internanosheet binding strength.[8] The exfoliation of hydrous chlorides is shown in

Fig. 2(A), where heating causes a large quantity of water and gases to be released, which exfoliates the 2D TMO sheets.[26] Table 1 summarizes the structural, optical, and electrical properties of various 2D LMOs and compares them with their bulk counterparts. It clearly shows that when these oxides such as MgO, CaO, TiO_2, MoO_3, MnO, and NiO are reduced from their bulk form to monolayers or ultrathin nanosheets, their electronic structures undergo significant modifications. The bandgap values, which are relatively large in bulk materials (indicating insulating behavior), decrease substantially in the 2D forms, leading to a transition from insulator to semiconductor. This bandgap reduction arises from quantum confinement, surface state effects, and changes in orbital hybridization at reduced dimensions.

Fig. 2(B) shows a production method where metal cations are mixed with graphene oxide to generate interconnected nanocrystals, when graphene oxide is removed, give rise to the 2D character of TMO.[29] Fig. 2(C) shows how metal ions are coated on graphene oxide by the mixing of metal precursor suspension sheets in the production process for crumpled 2D TMO. Crumpled 2D TMO is formed in part due to the attraction of metal ions by negative zeta potential of graphene oxide.[30] Since many 2D LMOs are valence compounds, ion-exchange techniques of exfoliation are typically employed. These methods call for the existence of charge-balancing counterions that sit
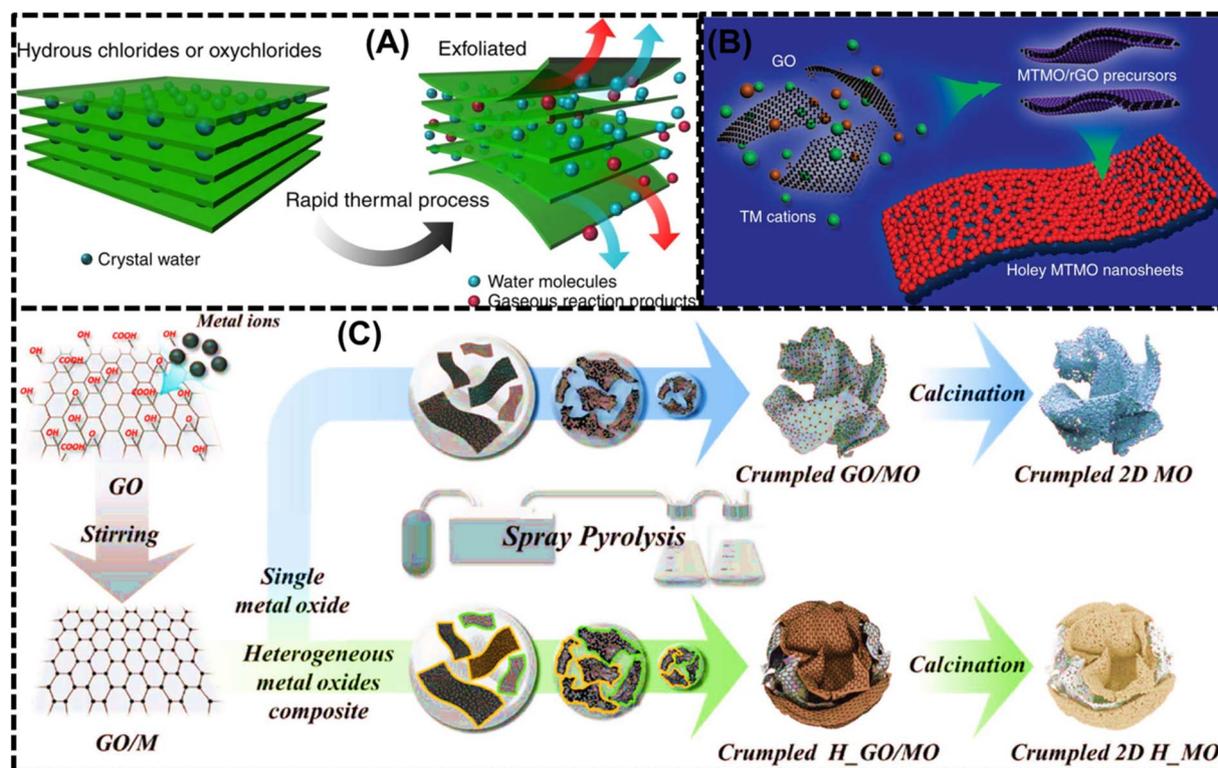

Fig. 2 (A) Schematic of the exfoliation of hydrous chlorides, in which during heating a large amount of water and other gases are released, which exfoliates the 2D TMO sheets. Reprinted with permission from ref. 26 copyright of Nature 2016. (B) A schematic strategy for the synthesis of 2D TMOs in which metal cations are mixed with the graphene oxide. Reprinted with permission from ref. 29 copyright of Nature 2017. (C) Schematic of the synthesis process of crumpled 2D TMOs, in which metal ions are coated onto GO by mixing a metal precursor suspension with the sheets. Reprinted with permission from ref. 30 copyright of WILEY-VCH Verlag 2019.

Table 1 2D LMOs and their structural, optical and electrical properties

LMOs	Layer	Bandgap (eV)	Electrical properties	Work function	References
MgO	Bulk	7.8	Insulator 10^{-14} to 10^{-16} Ω^{-1} cm^{-1}	4.22	31 and 32
	Monolayer	3.37	Semiconductor	3.31	32 and 33
	Spherical shape	5.90	—	—	34
	Ultrathin MgO nanosheets	5.83	—	—	34
CaO	Bulk	5.5	Insulator	—	35
	2D CaO (100)	2.03 eV	Semiconductor	4.54	36 and 37
TiO$_2$	Bulk	3.0–3.2	Insulator or weakly conducting	4.2	38 and 39
	Monolayer	1.19–2.76 eV	Semiconductor	—	40
MoO$_3$	Bulk	3.2–3.5	Insulator or weakly conducting	6.8 in vacuum and 5.32 in air	41 and 42
	Monolayer	2.6–2.9	Semiconductor	6.4	43 and 44
MnO	Bulk	3.46	Insulator	—	45
	2D MnO (100)	0.88	Semiconductor	—	46
NiO	Bulk	3.5–4.0	Insulator	5.2–5.6	47 and 48
	2D NiO (100)	1.21	Semiconductor	4.81	49 and 50

between the layers. The interlayer distances between the sheets are increased and their ability to exfoliate is enabled by replacing these counter-ions with bigger ones such as tetra-butylammonium ions.[8] Saupe *et al.*[25] showed that exfoliating K$_4$Nb$_6$O$_{17}$ results in a colloidal suspension of individual nanosheets following acid exchange with tetra(*n*-butyl)ammonium hydroxide in water.[19,25] These sheets spontaneously roll into loosely bound tubular structures. The tubular morphology can be permanently stabilized by precipitating the colloidal suspension with alkali cations, offering a controlled approach to fabricating nanostructured materials with tailored properties. During this process, the intercalation and subsequent replacement of alkali ions weaken the interlayer electrostatic interactions, promoting the delamination of the layered oxide into single sheets. These exfoliated nanosheets exhibit a strong tendency to self-assemble into tubular morphologies, driven by surface energy minimization and charge imbalance at the sheet edges. Using a layered protonic manganese oxide, H$_{0.13}$MnO$_2$·0.7H$_2$O, in a tetra(*n*-butyl)ammonium hydroxide (TBAOH) solution, Omomo *et al.* synthesised 2D MnO$_2$ and investigated its exfoliation and swelling behavior.[51] At moderate TBA ion concentrations, the layered manganese oxide underwent typical intercalation, forming a TBA-intercalated phase with a gallery height of 1.25 nm. However, osmotic swelling occurred when there was a notable excess of TBA ions present, which resulted in a large increase in interlayer spacing, ranging from 3.5 to 7 nm. For a variety of applications, this adjustable swelling behavior offers important insights into the controlled exfoliation and processing of 2D manganese oxide nanosheets.[51]

In layered 2D metal oxide materials composed of M–O, where M = V, Mo, or Mn octahedral, the in-plane atoms are connected by strong chemical bonds, whereas the stacking layers are connected by weak van der Waals interactions.[15] As a result of the strong chemical connections that connect all of the atoms, the majority of layered 2D morphologies are not layered and instead have a lot of unsaturated dangling bonds on their surfaces or along their edges. Examples of these surfaces include TiO$_2$, SnO$_2$, In$_2$O$_3$, and ZnO, which have high activity and high energy. Traditional LMOs are represented by the materials MoO$_3$ and V$_2$O$_5$.[15] Each layer of MoO$_3$ is primarily made up of disordered MoO$_6$ octahedral crystals, and 2D V$_2$O$_5$ typically has an orthorhombic crystal structure made up of zigzag double chains of V$_2$O$_5$ pyramids with square bases that are joined by comer-shared bridge oxygen atoms.[15,52] A simple technique for creating stacked MnO$_2$ nanosheets with a high specific surface area and exceptional specific capacitance was disclosed by Zhao *et al.*[53] Because of the reactive nature of the carbon atoms in the graphene framework, the method uses graphene oxide (GO) as a template and makes use of its capacity to enable the *in situ* reduction of MnO$_4^-$ ions to Mn(IV). MnO$_2$ completely replaces the template because of the consistent contact between MnO$_4^-$ ions and each layer of graphite, which is ensured by strong hydrophilicity of GO. During the *in situ* reduction of MnO$_4^-$ to Mn(IV), GO not only provides a uniform platform for the nucleation and growth of MnO$_2$ layers but also introduces oxygen-containing functional groups (such as hydroxyl, epoxy, and carboxyl) that can induce defect formation within the MnO$_2$ lattice. These defects, mainly oxygen vacancies and lattice distortions, enhance the electronic conductivity by creating localized donor states and facilitating electron hopping between Mn^{4+} and Mn^{3+} centers. This method suggests that layered 2D manganese oxides may be created using other graphene-like materials such as reduced graphene oxide (rGO) and graphitic carbon nitride (g-C$_3$N$_4$). The resulting nanostructure exhibits great potential for use in catalytic, adsorption, and degradation processes. Furthermore, using graphene oxide as a template not only accentuates its special two-dimensional structure but also offers a flexible way to create other metal oxides with unique planar architectures and enhanced functionality, which makes this approach extremely promising for further development.[53] MoO$_3$ is a wide bandgap, n-type material with superior dielectric characteristics that belong to the 2D materials family. The band structure of MoO$_3$ can be easily modified by ionic intercalation, allowing for control over its properties. This allows it to be manufactured in diverse forms, from semi-metallic to insulating, as needed.[54,55] Ion intercalation frequently alters the stoichiometry of materials by creating oxygen vacancies, which enhances the density

of states at the Fermi level and increases the concentration of charge carriers. In the case of MoO_3, stacked MoO_6 octahedral units comprise the thermodynamically stable orthorhombic α-MoO_3 phase.[55] Weak van der Waals forces hold these layers together as they are piled along the (010) vertical direction, making intercalation and exfoliation operations simple. Because of its structural flexibility, α-MoO_3 is a potential material for use in electrical devices, energy storage, and catalysis.[55] Corner-sharing rows along the (100) direction and edge-sharing MoO_6 octahedra along the (001) direction make up each double layer of α-MoO_3. Layers from the parent crystal can be easily exfoliated due to this special arrangement. Long rectangular crystals are formed when massive MoO_6 crystals preferentially break in the (001) direction during mechanical exfoliation. The weaker bonding of doubly coordinated O_2 atoms in contrast to the more strongly coordinated triply coordinated O_3 atoms is the reason for this behavior.[31] Rahman *et al.* used wet chemical etching as a top-down, economical method to create MoO_3 in the orthorhombic phase.[55] This method successfully generated high-quality MoO_3 nanosheets by adjusting the ratio of etchant to water to 1 : 500. Furthermore, it should be noted that in the thickness range under investigation up to 100 nm, the etch rate was independent of the original crystal thickness.[55]

Among various 2D LMO families, several sub-families stand out as particularly promising for electronic and energy device applications due to their distinct electronic structures and physicochemical properties. Transition metal oxides (TMOs) such as TiO_2, MoO_3, and NiO are among the most attractive candidates for electronic and optoelectronic devices.[56] TiO_2 exhibits high dielectric strength, tunable bandgap, and excellent environmental stability, making it suitable for high-k dielectrics, photocatalysis, and resistive switching devices. MoO_3, with its high work function and layered structure, supports efficient charge transfer and serves as a superior hole-transport layer in organic electronics and photodetectors. Similarly, 2D NiO demonstrates p-type semiconducting behavior and high chemical stability, useful for transparent electronics and spintronic applications.[6] For energy storage and conversion, sub-families such as MnO_x, CoO_x, and V_2O_5 are particularly promising.[57,58] Their multiple oxidation states enable fast redox reactions and high theoretical capacitance, making them ideal for supercapacitors, batteries, and catalytic energy devices. The layered structure of these oxides facilitates rapid ion diffusion and structural reversibility during charge–discharge cycles.

Chen *et al.* reported creating single-crystal WO_3 nanosheets with a thickness of 4–5 nm by laterally attaching small WO_3 nanocrystals during the solid–liquid phase of an arc discharge process.[59] Nanosheets made of six repeating monoclinic WO_3 cells along the c-axis were produced using this technique. Orthorhombic V_2O_5, however, has a multilayer anisotropic structure with deformed VO_6 octahedra as its building blocks. Ultrathin flakes are easily exfoliated from the bulk material by the weak van der Waals interactions between neighboring layers, opening the door to the creation of 2D V_2O_5 nanosheets with potential uses in various industries.[59] Rui *et al.* successfully

exfoliated few-layer V_2O_5 nanosheets with a thickness ranging from 2.1 to 3.8 nm by directly exfoliating bulk V_2O_5 crystals in a formamide solvent.[60] This process has tremendous promise for a number of applications, including energy storage and catalysis, by producing thin nanosheets while preserving the integrity of materials. By effectively exfoliating $HnbO_8$ sheets, Takagaki *et al.* created 2D single-crystal metal-oxide nanosheets from layered $HnbO_8$.[61] In this cation-exchangeable layered metal oxide, H^+ ions are intercalated between the 2D $Nb_3O_8^-$ anion nanosheets composed of NbO_6 octahedra. The ion-exchange process weakens the electrostatic interactions between layers, facilitating exfoliation into single nanosheets while introducing point defects such as oxygen vacancies and distortions in Nb–O coordination. These structural defects play a key role in modulating the electronic structure of the material, and they can create localized energy states near the conduction band, thereby enhancing n-type conductivity through increased carrier density. Among other advantages, exfoliated 2D single-crystal nanosheets offer a more precise and comprehensive interpretation of the surface structure and the functional groups on the surface, making them valuable for a range of catalysis and materials science applications.[61] By soft-chemically delaminating layered $RbTaO_3$, Fukuda *et al.* successfully synthesised tantalum oxide nanosheets with open channels.[62] A protonated sample was shaken with a tetra-butylammonium hydroxide (TBAOH) solution for almost two weeks at room temperature. By modifying the TBAOH dosage to match the exchangeable protons in the oxide, effective exfoliation was achieved. This ion-exchange-driven exfoliation influences the defect density of the nanosheets. The replacement of protons can generate oxygen vacancies and edge defects, which modify the local electronic environment. Such defects can serve as charge carriers or trap sites, thereby affecting the electrical conductivity and carrier mobility of the exfoliated sheets. The open-channel morphology also facilitates ion transport and surface accessibility, enhancing the electrochemical performance. Overall, this approach not only produces high-quality 2D TaO_3 nanosheets but also provides a controllable route to engineer defects and tune electrical properties. The resulting unilamellar crystallites' unique structural properties make them promising for various applications, including high-k dielectric materials and lithium-ion batteries, where their enhanced surface area and channel structure may be used.[62] New properties emerge for 2D metal oxides over other 2D materials, tabulated in Table 2. The ultra-thin atomic-scale dimensions of 2D metal oxide materials contribute to these intriguing properties such as high thermal stability, good electrical conductivity, high mechanical strength and environmental friendliness. These attributes position 2D metal oxides as ideal candidates for use in high-energy-density supercapacitors and batteries.

Oxide nanosheets are frequently created by the chemical exfoliation of a parent material that has layers in an exfoliating solution; this process is the end result of significant swelling and weakening of the connection between the layers.[10] The nanosheets' exceptionally high 2D anisotropy is often associated with certain physicochemical properties. Over the last 10

Table 2 Advantages of 2D metal oxides over other 2D materials

Advantages of 2D LMOs	Explanation
High thermal stability	2D metal oxides have a higher thermal stability than other 2D materials, which means they can withstand higher temperatures without breaking down or losing their structural integrity. This makes them suitable for use in high-temperature applications[63]
Good electrical conductivity	Many 2D metal oxides have good electrical conductivity, which makes them useful for electronic applications, such as in transistors or sensors[64]
High mechanical strength	2D metal oxides have a high mechanical strength, which means they are less likely to break or deform under stress. This makes them suitable for use in structural applications[65]
Wide range of chemical properties	There are many different types of metal oxides, each with its own chemical properties. This means that there is a wide range of 2D metal oxides available, each with its own unique characteristics and potential applications[66]
Environmental friendliness	Some metal oxides, such as iron oxide or titanium oxide, are environmentally friendly and can be used in applications such as water treatment or air purification[67]

years, functional nanosheet crystallites made by exfoliating layered materials have been the focus of much research due to their theoretical appeal and practical relevance. Such as Fukuda et al.[62] synthesized by calcining a combination of Rb_2CO_3 and Ta_2O_5 at 1173 K for 20 hours, $RbTaO_3$ with a monoclinic layered structure was created. This product was then reacting with HCl for three days, and lastly the protonated sample was shaken in tetrabutylammonium hydroxide (TBAOH) and centrifuged at 2000 rpm. However, the host layers' chemical makeup and chemistry, as well as the forces that keep them stacked, all play a role in the exfoliation process.[10] The layer composition, layer charge density, and ionic guest species would be intrinsic components. The polarity of solvents and dielectric properties are crucial to the exfoliation process.[10] 2D LMOs are particularly beneficial for developing next-generation electronic devices because of their unusual qualities, including their peculiar atomic structure and many other features. Atomically thin sheet-like structures with weak van der Waals bonds between each layer comprise bonded metal cations and oxygen anions. These materials have superior heat conductivity in the in-plane direction, great mechanical strength, and semiconducting to metallic characteristics because of their layered structure. These 2D LMOs exhibit remarkable optical properties, and because of their high surface-to-volume ratio, they might be surface-functionalized for use in sensing and catalytic applications. Two-dimensional LMOs may be produced using various techniques, each having pros and cons. In liquid exfoliation, bulk metal oxide crystals are dispersed in a solvent and exfoliated into 2D layers. In chemical vapor deposition (CVD), precursors are added to a reaction chamber and heated to high pressures to grow 2D LMO layers on a substrate. In solvothermal synthesis, metal precursors and solvents are heated to high pressures to form 2D LMOs. Chemical exfoliation and template-assisted growth are also employed to produce 2D LMOs. Researchers are still exploring and improving these synthesis methodologies to produce high-quality, large-scale 2D LMOs for various electrical device applications.

Solid-state synthesis method provides a convenient approach for preparing functional layered oxides; however, the range of accessible compositions is often constrained by the interplay between thermodynamics and kinetics. A major limitation of this method is in the requirement for atomic diffusion, which necessitates high reaction temperatures and consequently favors the formation of thermodynamically stable phases.[68] Table 3 shows how a preparation method produces different morphologies and properties. The template-assisted technique involves introducing a structure directing or capping agent as a soft template to control and direct the in-plane crystal growth.[69] Sigallon et al.[70] employed a hydrothermal synthesis approach for the growth of ZnO nanowires using a template assisted method within the etched tracks of poled PVDF membranes. Vertically aligned ZnO nanowires with high aspect ratios were successfully grown on an Au seed layer, forming a Schottky like contact inside the cylindrical nanopores of poled β-PVDF. Although the hard template method is an effective approach for synthesizing crystalline oxides, it faces several limitations that hinder its efficient use. These include poor control over pore size and undesired nucleation outside the template pores, leading to reduced yield, and complex, high-cost processing steps.[71] Moreover, during template removal, the use of harsh chemical conditions such as HF etching can potentially damage the nanomaterial structure.[72] In the liquid-phase exfoliation of layered metal oxides, the yield is generally low (2–5%) because an equilibrium forms between the exfoliated nanosheets and the deflocculated aggregates.[73]

Wang et al.[83] developed the adaptive ionic layer epitaxy method to overcome this challenge and enable the synthesis of inorganic nanosheets at the water–air interface. The adaptive layer epitaxy (AILE) method is a representative water–air interface approach for synthesizing 2D nanosheets. In this process, an ionic surfactant is dissolved in water to form a closely packed monolayer at the water–air interface. Using AILE, they successfully fabricated few nanometers thick, freestanding single-crystalline ZnO nanosheets with lateral dimensions reaching several tens of micrometers,

Table 3 2D LMOs produced by different methods, and their structure and thickness

Materials	Structure	Crystal system	Thickness (nm)	Methods	References
h-TiO$_2$	Layered	Hexagonal	0.45	Metal gas interface	74
h-Al$_2$O$_3$	Layered	Hexagonal	0.62	Metal gas interface	74
α-MoO$_3$		Orthorhombic	4	PVT, mechanical exfoliation	75–77
WO$_3$		Monoclinic	0.72	ALD	78
ZnO	Nonlayered	Hexagonal	0.6	Liquid metal printing	79
TiO$_2$	Nonlayered	Tetragonal	2	Liquid metal printing	80
ZnO		Wurtzite structure		Template assisted	70
Ga$_2$O$_3$	Layered	Monoclinic	2.8 nm	Liquid metal-based spin coating exfoliation	81
MnO$_2$	Layered	Rhombohedral	0.8	Ion exchange exfoliation	82
MoO$_3$	Layered	Orthorhombic		Chemical etching	55
ZnO nanosheets		Hexagonal	2.012	Adaptive ionic layer epitaxy (AILE)	83

formed beneath oleyl sulfate monolayers at the water–air interface. Compared to the ionic surfactant monolayer templating method, nonionic surfactants offer the advantage of easier removal through simple solvent extraction.[84]

4. Electronic tuning strategies for 2D LMOs

The characteristics of 2D layered metal oxides (2D LMOs) may be changed in a variety of ways, making them more suitable for certain applications. Examples of how doping with foreign substances enhances conductivity by adding rate providers and changing the band structure are nitrogen or boron-doped 2D LMOs.[85] The electronic properties tuning strategies in the 2D layered metal oxides are given in Fig. 3. Strain engineering by mechanical deformation or substrate-caused stress has been shown to influence lattice houses and bandgap in studies on MoO$_3$ and WO$_3$. By stacking layers or creating heterostructures with other 2D materials, including graphene, quantum confinement effects can be produced that are suitable for electrical devices.[86] Thickness tailoring in α-MoO$_3$ nanosheets was shown to increase carrier mobility from ~0.5 cm^2 V^{-1} s^{-1} for bulk-like layers to ~1100 cm^2 V^{-1} s^{-1} for few-layer nanosheets.[87] Defect engineering, such as oxygen vacancy creation in TiO$_2$ nanosheets, enhanced conductivity by an order of magnitude while modifying the optical absorption edge from 3.2 eV to 2.9 eV.[88] These examples quantitatively illustrate how morphology, defects, and
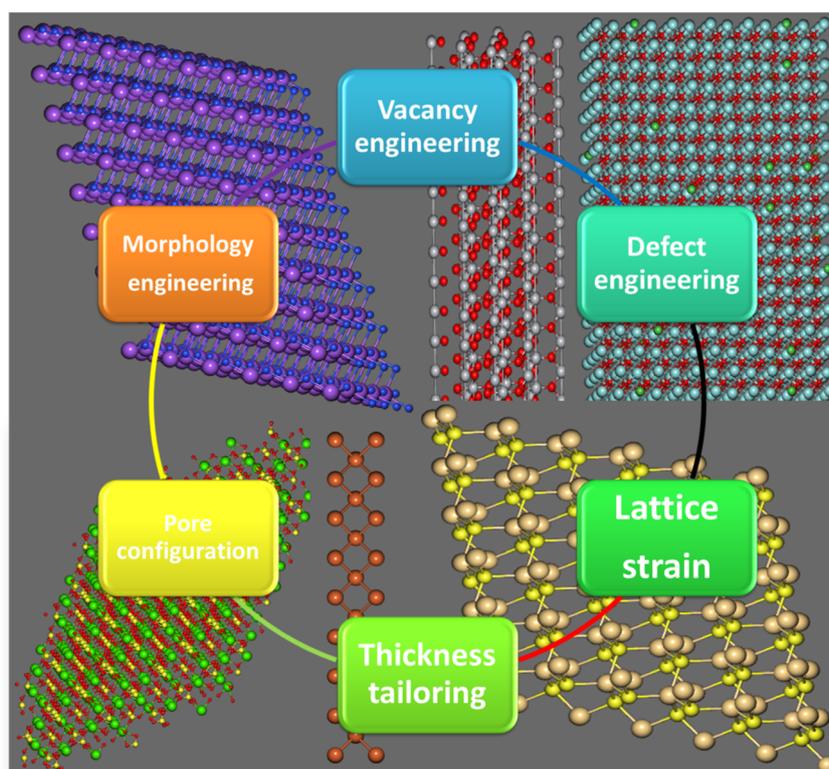

Fig. 3 Electronic property tuning strategies in 2D layered metal oxides.

heterostructure formation directly influence carrier mobility, dielectric response, and optical behavior of 2D LMOs. As demonstrated by field-effect transistors and electrolyte-gated devices, the bandgap and service attention may be dynamically changed by using an external electric powered area or electrochemical gating. Reactivity and performance are tailored by edge and grain boundary engineering, and interactions in fuel and biosensing are made possible through floor functionalization.[89] It is feasible to induce the effects of quantum confinement by inducing photoexcited rate vendors in 2D LMOs or by combining them with quantum dots or nanoparticles.[90] Temperature changes and external influences also influence the band structure and magnetic characteristics. There is a great deal of potential for 2D LMO optimization in modern electric and optoelectronic devices, sensors, and electrical systems when these approaches are combined. Through continuous study, the full potential of 2D LMOs to influence nanoelectronics and beyond is still being uncovered.

4.1 Morphology engineering

By using morphology engineering, 2D LMOs may have their structure and shape altered at the nanoscale to achieve certain purposes.[91] By changing the layer thickness in materials like MoO_3, researchers can take advantage of the quantum confinement phenomenon, in which electric characteristics are modified as a result of confinement inside a few atomic layers.[92] Powerful chemical reaction catalysts, 2D LMOs, like WSe_2, may contain grain barriers designed to enhance surface reactivity and catalytic efficacy. By creating certain nanostructures on 2D LMOs, such as nanopatterns on graphene oxide, which improve photodetection and sensing performance, improved mild-count number interactions are made possible. Additionally, the selective molecular interactions needed for biosensors and targeted drug delivery systems are facilitated by surface functionalization of 2D LMOs, such as TiO_2, with certain chemical compounds. In order to fine-tune the characteristics of 2D LMOs for a range of applications, from biological devices and environmental sensors to electronics and electrical garages, researchers may carefully control the morphology of 2D LMOs using growing procedures and substrate management. Because of current trends in morphology engineering, 2D LMOs are increasingly capable of supporting innovative nanotechnologies.[93] Fig. 4(A) shows the fabrication of $MoSe_2/MoO_x$ device and Fig. 4(B) the optical images of the device, whereas Fig. 4(C) the cross-sectional image of the device with the Raman shift in
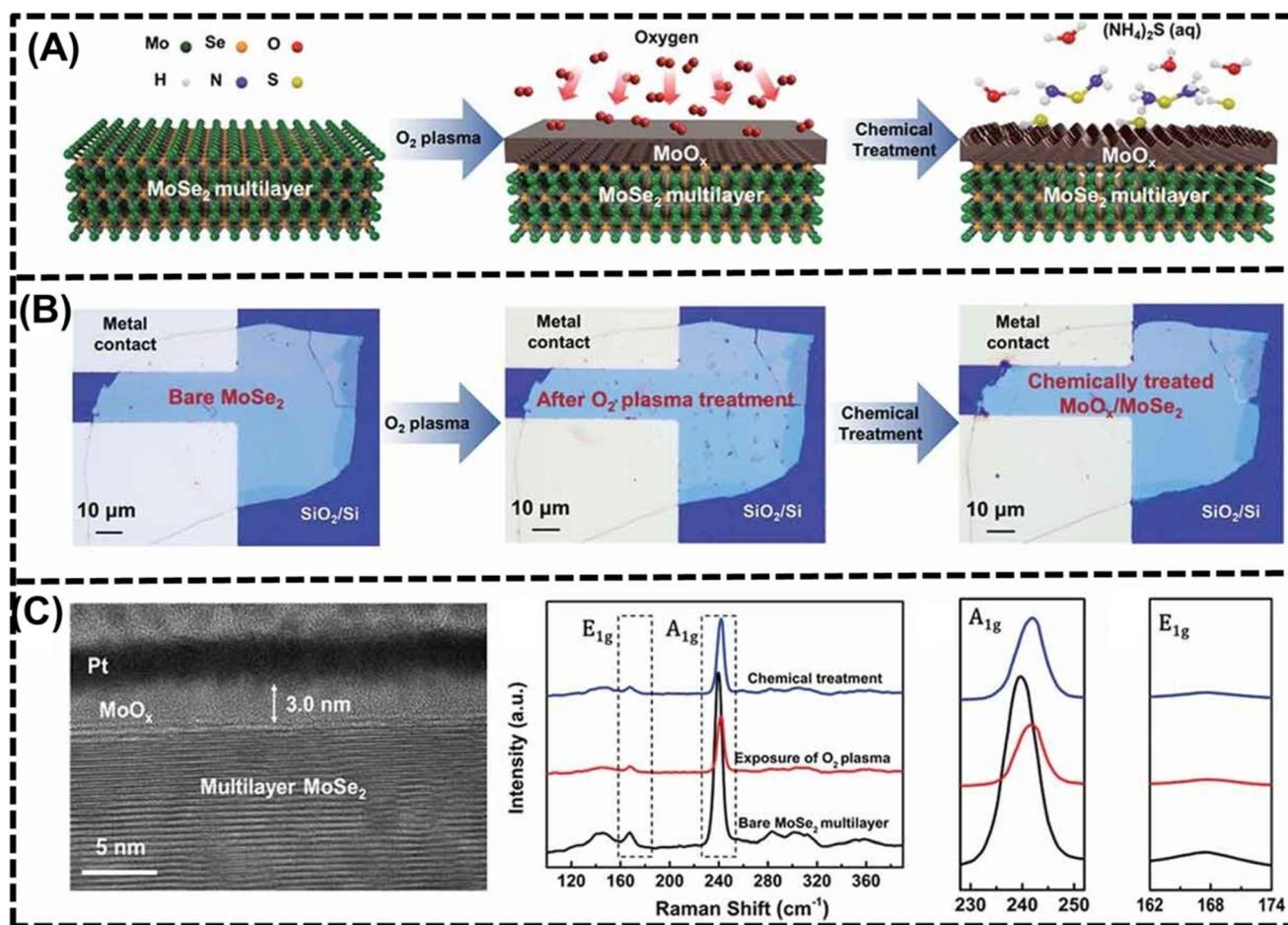

Fig. 4 Surface morphological engineering by the O_2 plasma treatment: (A) fabrication of the $MoSe_2/MoO_x$ device, (B) optical images of the device and (C) cross-sectional image of the device with the Raman shift in the device after chemical treatment and O_2 plasma treatment. Reprinted with permission from ref. 94 copyright of Taylor and Francis 2022.

the device after chemical treatment and O_2 plasma treatment. Field-effect transistors (FETs) based on two-dimensional materials are improved by a two-step surface engineering approach that customizes $MoSe_2$ multilayers.[94] MoO_x/$MoSe_2$ heterojunction is formed by O_2 plasma exposure, and surface roughness is corrected by dipping in an $(NH_4)_2S(aq)$ solution. When $MoSe_2$ is chemically etched, the ON/OFF current ratio drops to 5.7×10^4 from 1.1×10^5 in bare $MoSe_2$ FETs.[94] After chemical treatment, $MoSe_2$ with a greater surface roughness of 4.2 ± 0.5 nm was achieved. This treatment improves the surface-area-to-volume ratio and provides a regulated thickness with acceptable electrical property fluctuation.

4.1.1 Thickness tailoring. The thickness of 2D LMOs can be specifically tailored for advantageous functionalities by manipulating the range of atomic layers.[95] One of its most outstanding benefits is the thickness-established properties of
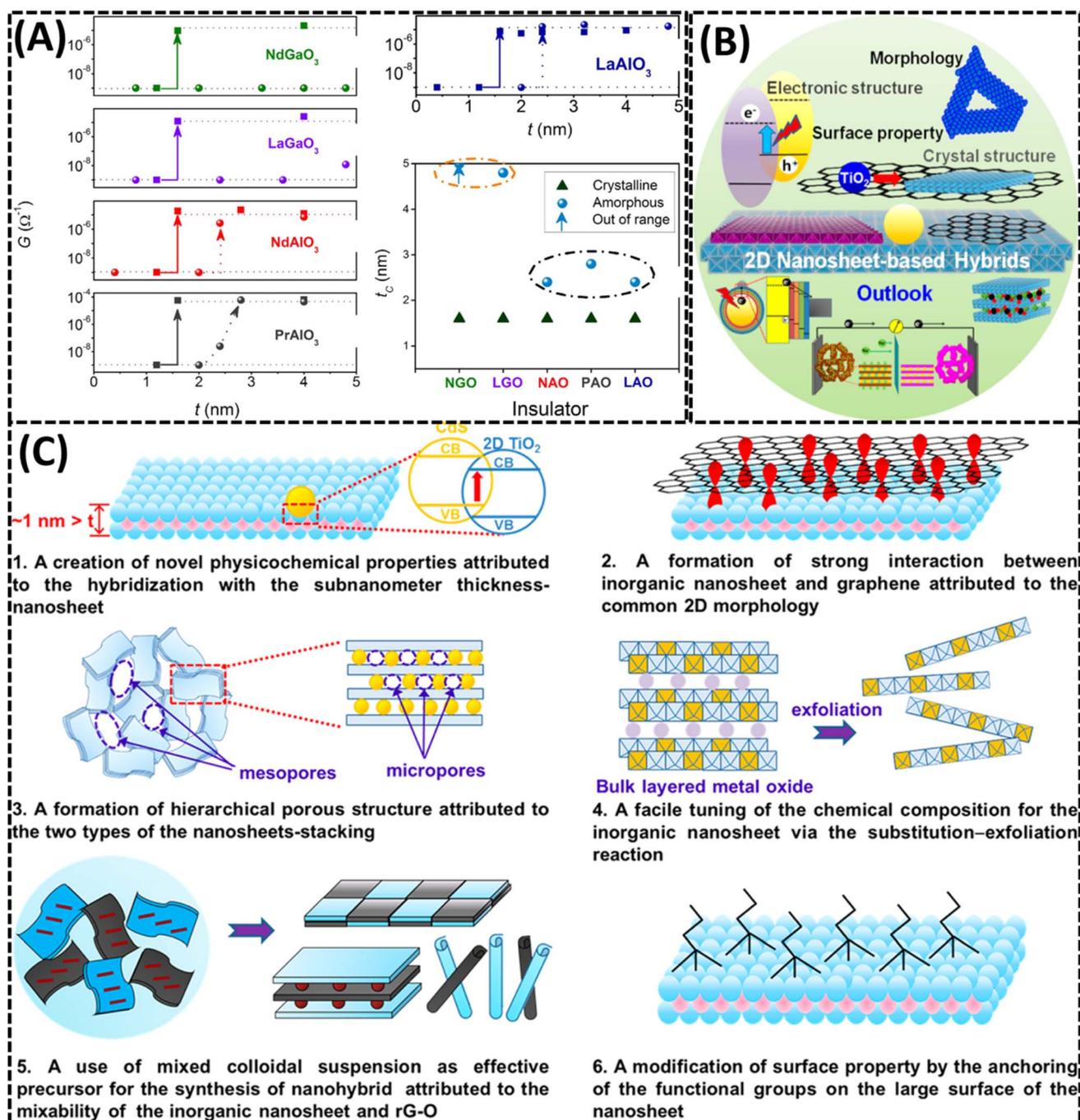

Fig. 5 (A) Conductance of crystalline (solid squares) and amorphous (solid spheres) materials that depends on their thickness ABO_3/STO, in which $NdGaO_3$, $LaGaO_3$, $NdAlO_3$, $PrAlO_3$, and $LaAlO_3$ are all included in ABO_3. Reprinted with permission from ref. 99 copyright of Nature 2015. (B) Surface-functionalized and thickness-tailored electronic device. (C) Process of thickness modulation and surface functionalization. Reprinted with permission from ref. 100 copyright of the American Chemical Society 2014.

2D materials, which may be exploited by appropriately altering the number of layers.[96] Examples include the emergence of quantum confinement effects, where the electrical band structure and optical characteristics are altered as a result of the constrained mobility of charge suppliers inside a narrow region, when the thickness is decreased to a monolayer or a few layers.[97] Due to their tunable bandgaps and stepped forward light-depend interactions, monolayer 2D LMOs are ideal for opto-electronic devices such as photodetectors and light-emitting diodes (LEDs).[98] Changjian Li demonstrates the thickness dependent properties for the metal-insulator transition in crystalline and amorphous forms of $LaAlO_3$, $PrAlO_3$, $NdAlO_3$,

$NdGaO_3$, and $LaGaO_3$.[99] At 4 unit cells, crystalline interfaces show a dramatic switch in conductance, with a 4-order (10^{-9} Ω^{-1} to 10^{-5} Ω^{-1}) change, as shown in Fig. 5(A). Although strain is induced by gallate and aluminate, the polar nature predominates. However, amorphous $AAlO_3$/STO critical thickness, which is dependent on the B-site cation oxygen affinity and experimental circumstances, is less than $AGaO_3$/STO interfaces ($\geq$5 nm), ranging from 2.4 to 2.8 nm. An electronic device based on 2D layers is presented in Fig. 5(B). A process for the surface functionalization and thickness modulation is presented in Fig. 5(C).[100] Larger layers of 2D LMOs can still perform their unique electric and mechanical tasks while also providing new
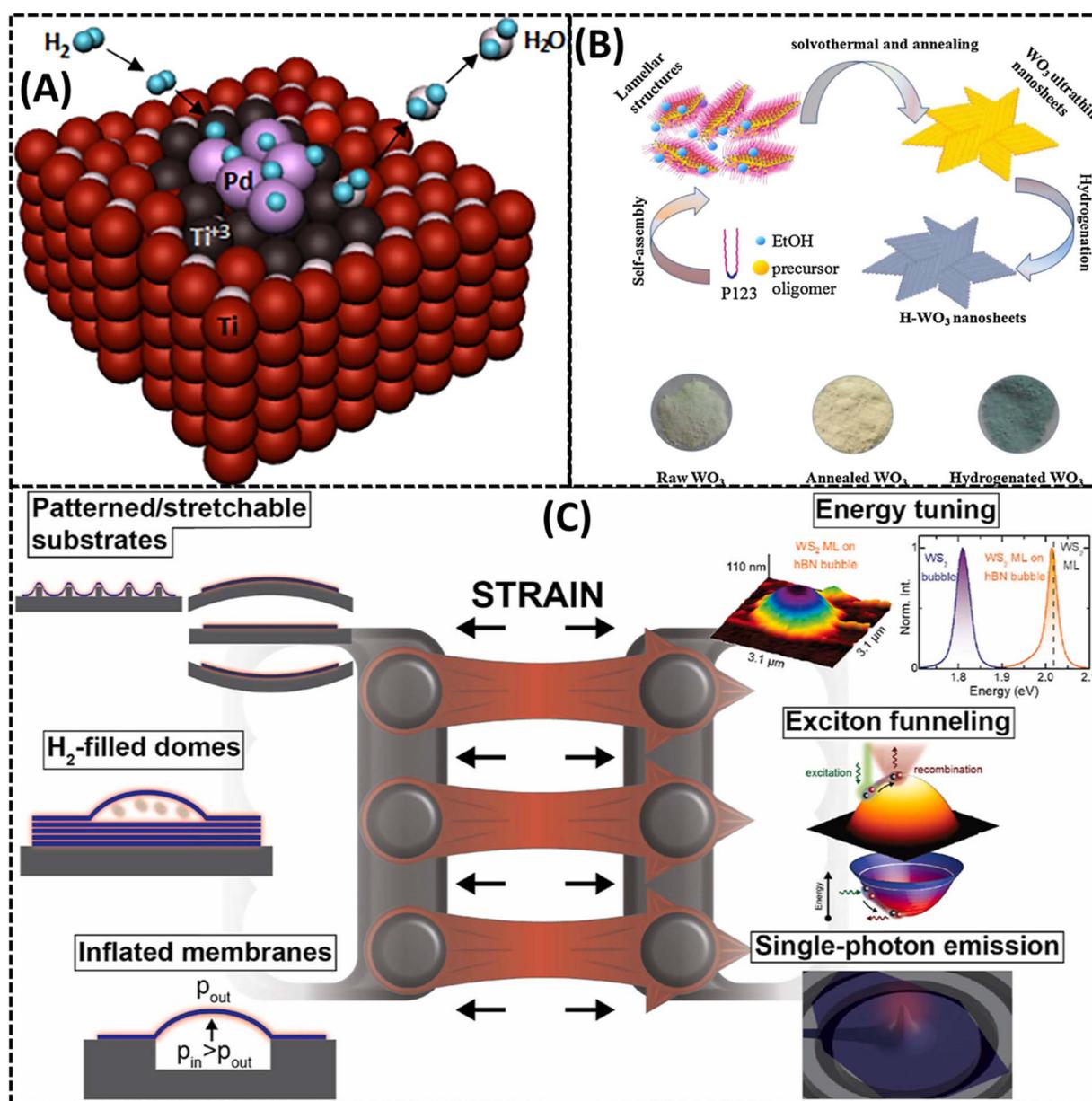

Fig. 6   (A) Pd defect as a reduction promoter at the 2D TiO_2 and 3D Pd interface. Reprinted with permission from ref. 107 copyright of Elsevier 2023. (B) Preparation procedure for the 2D WO_3 nanosheets, and the colors of the raw, annealed and hydrogenated WO_3 samples. Reprinted with permission from ref. 108 copyright of Elsevier 2017. (C) Tuning of optical properties by strain engineering in 2D materials. Reprinted with permission from ref. 110 copyright of Elsevier 2022.

ones. In FETs, thicker 2D LMOs, for instance, can provide increased electron mobility, leading to improved tool performance. Because researchers can carefully adjust their thickness to optimize their characteristics for specific applications in electronics, photonics, catalysis, energy storage, and more, 2D LMOs are extremely flexible materials with significant potential for future innovations.

4.1.2   **Pore configuration.** Pores are empty gaps or holes seen in the atomic structures of 2D layered metal oxides (LMOs) or in the spaces between their layers. The distribution and arrangement of these pores play a crucial role in defining the special qualities and possible uses of these materials. In applications where effective molecular transport and large surface area are crucial, such as gas sensing, energy storage, and catalysis, the size, morphology, and connectivity of the pores can have a substantial impact on the performance of the material.[101] The fraction of the fabric that pores have taken up is known as the porosity of 2D LMOs. Porous 2D LMOs are ideal for catalysis, fuel sensing, and power storage applications because of their increased porosity, which offers more floor space and improved accessibility to active sites.[102] The size and shape of the pores have an impact on the diffusion of molecules and ions inside 2D LMOs. Smaller, regular pores may encourage efficient mass transport, whereas larger and atypical holes should have a better storage capacity for gases and liquids. This connectivity is necessary for applications like ion delivery in supercapacitors and electrolytes for batteries. Researchers may also design the pore configuration of 2D LMOs using templating techniques.[103] By using sacrificial templates, certain pore topologies and dimensions may be created throughout the synthesis phase, allowing for fine-grained control of the material's properties. By changing the synthesis conditions and precursors, it is possible to tailor the pore configuration in 2D LMOs. The fabric may be tailored for a variety of purposes, including length-selective petrol separation and controlled medication administration in biological settings. Defects and facet pores in 2D LMOs can provide catalytically active sites and increase reactivity.[104] These imperfections can be created to enhance the performance during specific chemical processes. Pore arrangement in 2D LMOs is a crucial factor that affects how well they function in different applications. By developing and modifying the pore houses, scientists may also fully realize the potential of these materials for specialized and efficient application in areas such as catalysis, separation, sensing, and power storage technologies.

4.2   Defect engineering

Defects must be deliberately supplied and regulated in the atomic structure of 2D LMOs in order to change their characteristics and abilities.[105] Defects in 2D LMOs may be due to larger or missing atoms, atomic vacancies, dislocations, or impurities introduced during the synthesis process. The 2D LMO electrical band structure of 2D LMO may be altered by defects, changing its bandgap, electric conductivity, and service mobility. Scientists can control electrical characteristics to give a range of electronic devices the necessary conductive or

semiconductive behavior by purposefully generating defects. By acting as active sites for catalytic processes, defects in 2D LMOs may increase their catalytic interest.[106] By controlling the kind and concentration of defects, researchers may develop efficient catalysts for certain processes in electrical conversion and environmental packaging. In Fig. 6(A), the focus is on the role of a Pd defect as a reduction promoter at the interface between 2D TiO_2 and 3D Pd.[107] This suggests that the presence of Pd defect sites plays a crucial role in promoting reduction reactions at the interface of TiO_2 and Pd. In Fig. 6(B), the preparation procedure for 2D WO_3 nanosheets is outlined, accompanied by the visual representation of the color of raw, annealed, and hydrogenated WO_3 samples.[108] The color changes across these stages can provide insights into structural modifications or chemical transformations undergone by the WO_3 nanosheets during the preparation process. Defects may have a significant influence on 2D LMO capacity to sense gases.[109] By adding defects, the flat chemistry and reactivity may be altered, increasing the sensitivity and selectivity towards certain gases, which is beneficial for fuel sensing and environmental monitoring. The mechanical properties and power of 2D LMOs may be enhanced by defects acting as dislocation movement pinning sites. This quality is what makes them useful in nanocomposites and flexible electronics. As a result of disorder engineering, the optical properties such as moderate absorption and emission may get regulated. Growing materials for products like photodetectors and light-emitting devices, which need precise optical performance, is essential. By modifying the results of defects at the mobility and dispersion of charge carriers in 2D LMOs, researchers may also change the delivery of charge and improve the functionality of the electronic devices.

4.2.1   **Lattice strain.** Lattice stress is a property of 2D LMOs, which is a term used to describe the distortion or deformation of crystal lattice brought on by external forces like mechanical strain or pressure brought on by substrate contacts.[111] Lattice pressure may significantly influence the physical and chemical characteristics of 2D LMOs, which may lead to a variety of intriguing phenomena and potential applications. Lattice pressure can affect the mechanical properties of 2D LMOs, such as their stiffness, tensile strength, and adaptability. Bendable electronics and other mechanical applications can benefit from the ability to be made more elastic by applying mechanical pressure.[112] Lattice strain has the power to modify the bandgap and other electrical characteristics by controlling the band structure of 2D LMOs. This pressure-induced bandgap modulation is crucial for controlling optoelectronic properties, including light emission and absorption.[113] The number of active chemical sites can increase as a result of localized defects and distortions brought about by lattice stress. Due to their advanced reactivity, strapped 2D LMOs can serve as potent catalysts in catalytic applications. The results of the lattice stress, carrier mobility and scattering techniques can influence the electric conductivity and rate shipping behavior of 2D LMOs.[114] The rate of carrier mobility of a material can be affected by strained regions, which will impact how effectively it conducts strength. Because the stress-precipitated alterations in the lattice are reversible, real-time property modification is

possible.[115] Due to its reversibility, strain engineering is an effective method for dynamically improving the properties of 2D LMOs in a wide range of applications. In 2D LMOs grown on substrates, strain at the interface can be caused by a lattice mismatch between the substrate and the materials. This interfacial pressure has significant effects on the electric and mechanical characteristics of 2D LMOs, making it useful for device engineering. In 2D LMOs, lattice stress provides a flexible mechanism to change the properties and change them for special applications. In order to create flexible strain-tunable photonic devices based on 2D semiconductors, Salvatore Cianci et al. customized the optical characteristics of the 2D materials, as shown in Fig. 6(C).[110] The capacity of these materials to acquire desirable properties in areas like electronics, photonics, catalysis, and mechanical systems may be hastened by the use of stress engineering in nanotechnology and other domains.

4.2.2 Amorphization. 2D LMOs undergo amorphization, a process that transforms their initial crystalline structure into an amorphous, non-crystalline state.[116] In the amorphous segment, the atoms are produced in a disorganized manner and lack long periodicity. This alteration in form significantly affects the properties. For instance, the electrical, optical, and mechanical characteristics can change when crystalline 2D LMOs become amorphous.[117] Major effects of amorphization include defects and new active websites in the fabric. Amorphous 2D LMOs may be more reactive as a result of these disadvantages, which makes them perfect for catalytic and energy storage applications. The chaotic shape also helps to induce strain and flaws, which might change the fabric's mechanical and electrical characteristics.[118] Researchers can alter a certain functionality of the structure by using the outcomes of pressure. It is important to fully comprehend the amorphization process in order to assess its effect on the stability and long-term performance of 2D LMO-based devices. Amorphization can occasionally cause material degradation and restrict realistic use. Despite these challenges, researchers believe that amorphous 2D LMOs are distinct materials with distinctive properties that provide appealing potential for the current programme in nanotechnology and related fields. More research into the characteristics and behavior of amorphous 2D LMOs will help them reach their potential and pave the way for the development of cutting-edge additives and devices for upcoming technologies.

4.2.3 Vacancy engineering. Vacancies are intentionally introduced to and changed within the crystal lattice of 2D LMOs in order to control their properties and capabilities.[119] Utilizing such voids, which also provide a wealth of choices for material design and alertness-specific customization, significantly influenced the behavior of 2D LMOs.[120] Band structure, electrical conductivity, and carrier mobility of 2D LMOs may all be altered by vacancy engineering. Vacancies function as distribution centers, which impacts the quality of electric transportation. Second, by serving as active sites for beneficial chemical processes, these deliberate defects can improve the catalytic efficiency of 2D LMOs. Researchers may develop effective catalysts for techniques like water splitting and CO_2

reduction by carefully modifying the density and distribution of vacancies, advancing the era of green energy. Furthermore, 2D LMOs' optical characteristics are harmed by vacancy engineering, which has an impact on their mild emission and absorption characteristics. They are therefore excellent choices for photonics and optoelectronic applications.[121] The mechanical and thermal properties of the materials may also be modified by vacancy engineering. This is feasible because vacancies might operate as pressure spots, which would change mechanical energy, and they might switch phonon scattering, which would influence heat transfer. Furthermore, charge storage sites may also operate as vacancies, which may potentially influence the capacity of 2D LMOs in batteries and supercapacitors to store energy. The performance of the electrocatalyst in Zn–air batteries (ZAB) and water splitting is examined by Xiaolin Hu in relation to its electronic structures and attributes, such as given in Fig. 7(A)–(C).[122] Excellent electrochemical efficiency for both hydrogen and oxygen is demonstrated by three-dimensional core–shell NiCoP/NiO heterostructures with controlled oxygen vacancies grown on carbon fabric. The hybridization of the NiO shell and the NiCoP core creates a synergistic electronic coupling effect that optimizes local electronic structures. In ZAB and water splitting applications, the hierarchical nanoarrays improve mass transfer, active site exposure, and overall electrochemical performance. By carefully adjusting vacancies, researchers can enhance the charge storage capability and electrochemical performance of power storage devices. Understanding how vacancies impact how the material degrades in unique environmental situations is essential to the long-term performance of these devices. Additionally, there is still research being done on vacancy engineering in 2D LMOs, which has the potential to reveal new material features and make it easier to introduce new materials and devices for various applications.

4.3 Heterostructure engineering of 2D metal oxides

Heterostructure engineering of 2D LMOs refers to the actual positioning of multiple 2D LMOs and other 2D materials to create vertically stacked or lateral interfaces, generating novel systems with exceptional properties and features.[124] Due to the concept of heterostructures, which makes use of the varied properties of certain 2D materials and allows for the customization of their collective behavior, advanced electric and optoelectronic devices now offer exciting new prospects.[125] Vertical heterostructures, which can be multi-layered structures with atomically thin surfaces, are made by stacking different 2D LMOs and other 2D materials on top of one another.[126] Band engineering, confinement, and charge transfer are all made possible by these interactions. For instance, forming a vertical heterostructure from a monolayer of MoO_3 and a monolayer of WO_3 may result in type-II band alignment, where electrons and holes are spatially separated.[127] This makes it possible to effectively separate the photodetection and solar power conversion applications. A number of 2D LMOs are coupled in a single surface to create lateral heterostructures, which offer a clean interface between
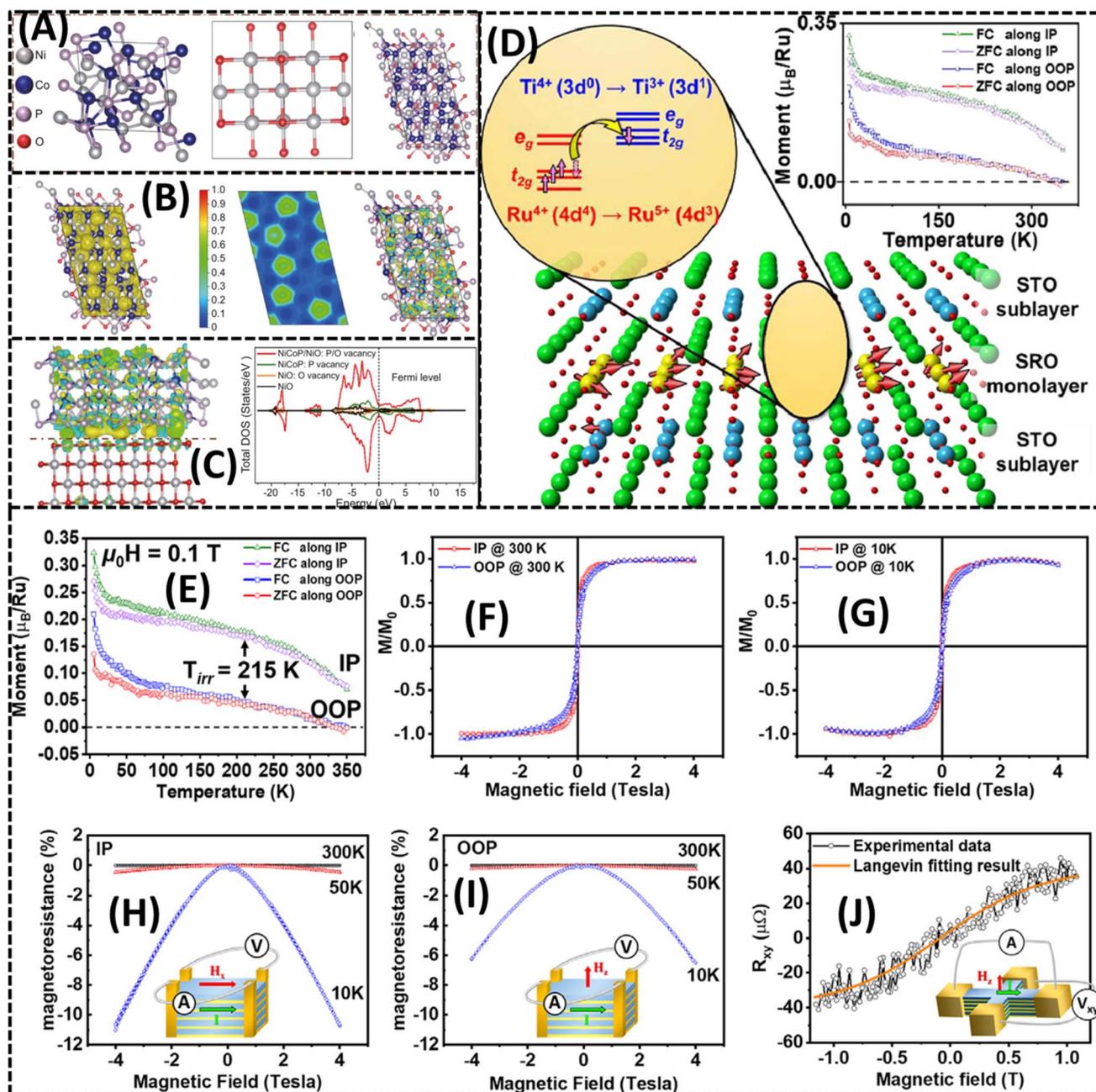
Fig. 7 (A–C) DFT-optimized structures of NiCoP, NiO and NiCoP/NiO heterostructures with their electronic local function and density of states. Reprinted with permission from ref. 110 copyright of Elsevier 2022. (D) Origin of ferromagnetism based on high-quality SrRuO$_3$-monolayer-based superlattices. (E) Temperature-dependent magnetization curves with an applied field of 0.1 T for both in-plane and out-of-plane zero field cooling (ZFC) and field cooling (FC). (F) At 300 K, magnetization was seen as a function of normalized field in both the IP and OOP directions. (G) At 10 K, normalized field-dependent magnetization was seen in both in-plane and out-of-plane orientations. (H and I) Magnetoresistance curves measured with an applied field in the in-plane and out-of-plane directions, respectively, at 300 K, 50 K circle and 10 K (insets: device and field direction). (J) Transverse magnetoresistance depending on field, recorded at 300 K (inset: device and field direction). Reprinted with permission from ref. 123 copyright of Elsevier 2021.

various materials. This method makes it possible to create heterojunctions with unique electrical properties. For instance, by establishing a lateral heterostructure between MoO$_3$ and WO$_3$, researchers may create a p–n junction that can be used in transistors and diodes. Heterostructures can induce stress in 2D LMOs because of lattice mismatch, changing their electric and mechanical characteristics. Heterostructures

provide more degrees of freedom for strain engineering, allowing for further customization of performance. By modifying the layer stacking and lattice alignment for certain purposes, researchers may change the bandgap, electrical mobility, and other characteristics.[128] The interfaces in heterostructures play a significant role in driving the overall performance. By atomically tailoring the interface, it is also

possible to improve device performance, reduce recombination losses, and improve switching properties.[129] Specific phenomena, like moiré patterns, can be produced by careful interlayer control and employed in a variety of quantum and sensor applications. Heterostructures offer an adaptable foundation for making functional devices with unusual properties.[130] These include ultrafast transistors, high-efficiency photodetectors, and adjustable lasers. The numerous combinations of 2D LMOs and other 2D materials in heterostructures enable the unattainable electrical, optical, and mechanical capabilities. One of the fascinating areas of materials science and nanotechnology is heterostructure engineering of 2D LMOs. The distinctive properties of various 2D substances and their interactions can be used by researchers to develop revolutionary devices with improved performance and capabilities. A gradual transformation of next-generation electric, optoelectronic, and quantum technologies is anticipated as a result of the continued study of heterostructures. Liu *et al.* are investigating the ferromagnetism in $SrRuO_3$-monolayer-based superlattices, as shown in Fig. 7(D).[123] For both field cooling (FC) and zero field cooling (ZFC), temperature-dependent magnetization curves are shown in Fig. 7(E) along the in-plane (IP) and out-of-plane (OOP) directions when a field of 0.1 T is applied. By displaying magnetization as a function of the normalized field at 300 K in both IP and OOP directions, Fig. 7(F) offers details on the system's magnetic response under different field strengths. The magnetic characteristics are further elucidated at a lower temperature (10 K) in Fig. 7(G), where the normalized field-dependent magnetization is displayed. At various temperatures (300 K, 50 K, and 10 K), the magnetoresistance curves in Fig. 7(H) and (I) show how resistance varies with an applied magnetic field in the IP and OOP directions, respectively. Fig. 7(J) shows transverse magnetoresistance at 300 K as a function of the field, offering more details on how the material reacts to an applied magnetic field. All together, these curves and observations help to clarify the type and properties of ferromagnetism in $SrRuO_3$-monolayer-based superlattices.

5. Potential electronics applications

2D LMOs offer a lot of potential for a variety of electronic applications because of their special qualities and tunability. They may be transformed into highly effective FETs, resulting in quicker and more powerful electronic devices. Due to their wide surface area and surface activity sensitivity, efficient circuits are ideal for gas and biosensors because they enable selective detection. Furthermore, enhanced optical communication in 2D LMO light detectors, and other devices provides high-performance photoelectric conversion. They are also used in energy storage, where they boost lithium-ion batteries' efficiency and supercapacitors' capacity. Because of its mechanical flexibility, it may also be utilized in wearable technology and flexible electronics. Lateral confinement in 2D nanosheet structures alters the electronic structure and influences electron-transport processes due to the quantum confinement effect.[131] The conductivity and other electrical characteristics of the material may vary significantly as a result of this impact. There are many possible uses for 2D metal oxides, as shown in Fig. 8. Oxide nanosheets have different electrical behaviors even if their 2D shapes are comparable. The majority of oxide nanosheets that have been synthesised thus far are made of d^0 transition metal oxides, which include Ti^{4+}, Nb^{5+}, Ta^{5+}, and W^{6+}. These metal ion-unoccupied d-orbitals interact with the surrounding ligands' full p-orbitals. Because of this, they have special electrical qualities that make them extremely adaptable to a wide range of uses. These d^0 oxide nanosheets are suitable as semiconducting or insulating materials but are not very interesting electrically. MnO_2 and RuO_2 nanosheets, which are either redox-active or semi-metallic, are a couple of the outliers.[131] These oxides are distinguished by their electronic structure, which either has a d-shell that is vacant or orbitals that are completely filled. As a result of photon absorption and a gap energy between the valence and conduction bands, which are primarily produced by the oxygen 2p and metal 3d or 4s orbitals, respectively, these oxides separate charge.[132,133] A two-atom electronic transition that stabilizes the charge separation and allows carriers with a significantly longer lifetime to 10–100 ns to migrate may be the cause of
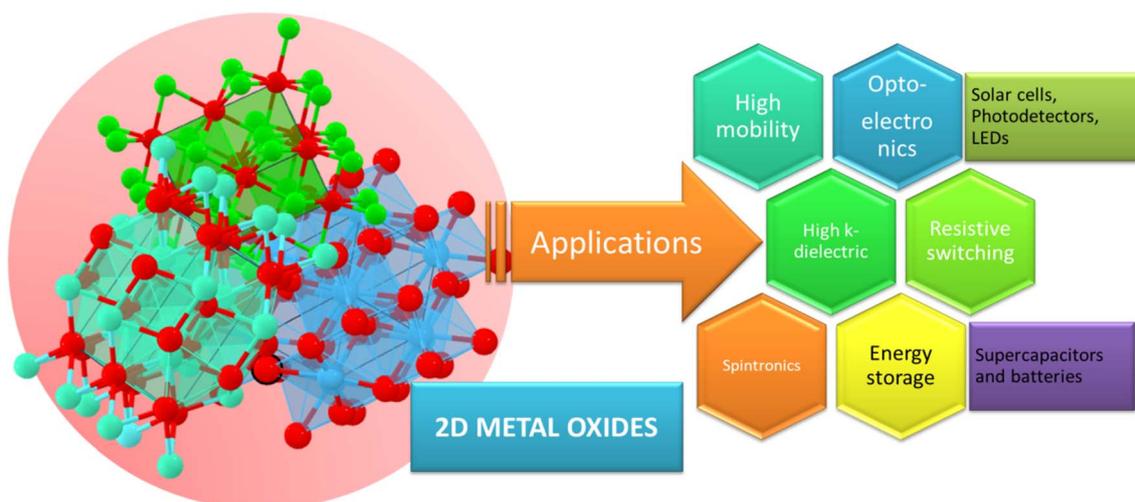

Fig. 8 Potential applications of 2D metal oxides.

the development of photoconductivity in these oxides.[133] However, because of their wide band gaps, which must be excited by UV light, they are less effective at using solar energy.[132] We anticipate that some very complex nanostructured systems, such as those with effective photoelectric energy conversion and photocatalytic activities, may be created by synthesis. To do this, understanding basic semiconductor properties like band gap energy and flat band potential is crucial.[134] Titanium anatase nanosheets are shown by Sakai *et al.* to have flat band potentials of 1.27 V and 1.15 V with band gap energies of 3.8 eV and 3.2 eV, respectively.[134] Consequently, the valence band's upper edge is 0.5 eV lower and the conduction band's lower edge is 0.1 eV higher in titania nanosheets than in anatase. This suggests that the electron–hole pairs photogenerated by titania nanosheets have stronger reduction and oxidation capabilities than anatase, which increases their potential for use in photocatalysis and other energy-related technologies. Additionally, we categorized the reported 2D oxides into their groups based on the periodic table (summarized in Table 4). These materials have favorable physiochemical characteristics such as exceptional dielectric resistance, low electrical conductivity, high thermal conductivity, and a spectacular refractive index. Owing to the outstanding properties exhibited by these oxides, which are aligned with the characteristics of the respective elements in their present periodic group, they find applications across diverse fields, as outlined in Table 4.

5.1 Optoelectronic applications

The broad bandgap of the majority of 2D oxides is clearly seen in Table 5. These imply that 2D oxide-based photodetectors can attain a broad detection range and operate efficiently in the UV region. Due to the quantum size effect, the optical

characteristics of 2D oxides differ from those of their bulk counterparts. The band gaps of 2D TMOs are displayed in Fig. 9(A), which also offers details on their electrical properties and uses.[157] UV-visible absorbance spectra for bulk and 2D MoO_3 solution are shown in Fig. 9(B), providing information about the optical absorption characteristics of the 2D material.[158] Due to their transparency, mechanical flexibility, and manufacturing simplicity, atomically thin 2D nanosheets have special benefits in optoelectronic that are compatible with the highly developed silicon-based platform.[159,160] 2D LMOs have a great deal of potential for use in a wide range of optoelectronic applications including high-performance photovoltaic cells for the conversion of solar energy, high-performance photodetectors for optical communications and imaging, and emission materials in light-emitting diodes (LEDs).[161] Some 2D LMOs have laser qualities and may be exploited, which make them appropriate for low-power laser technology. They can also be utilized in photoelectrochemical cells for solar water splitting and optical modulators for signal processing and transmission. The Tauc plots and UV-vis absorption spectra for 2D WO_3 synthesised using various carboxylic acid auxiliary agents (citric acid, oxalic acid, and tartaric acid) are shown in Fig. 9(C) and (D).[162] This provides a comprehensive picture of the band gaps and optical properties of 2D WO_3 synthesized under different conditions. Due to their customizable bandgaps, high carrier mobility, and potent light–matter interaction, 2D LMOs are an intriguing possibility for enhancing the optoelectronic properties. A practical framework for the development of UV photodetectors is offered by high-performance 2D photodetectors with a planar geometry and a number of remarkable features. Over time, interest in 2D oxides, a type of 2D material composed of the O element and a metallic or quasimetallic element.

Table 4 Different 2D metal oxides based on different element groups

Group	Metal oxide	Possible applications	Ref.
2	Magnesium oxide (MgO)	Electronics, catalysis, sensors	135
3	Aluminum oxide (Al_2O_3)	Catalyst supports, ceramics, abrasive materials	136
	Gallium oxide (Ga_2O_3)	Transistors, solar cells, gas sensors	137
	Indium oxide (In_2O_3)	Gas sensors, transparent conductive coatings	138
4	Titanium dioxide (TiO_2)	Solar cells, photocatalysis, gas sensors	139
	Zirconium dioxide (ZrO_2)	Ceramic materials, fuel cell membranes	140
	Hafnium dioxide (HfO_2)	Transistor gates, high-k dielectrics	141
5	Vanadium oxide (V_2O_5)	Gas sensors, battery electrodes, electrochromic devices	142
	Niobium oxide (Nb_2O_5)	Gas sensors, photocatalysis	143
	Tantalum oxide (Ta_2O_5)	Capacitors, dielectrics, sensors	144
6	Chromium oxide (CrO_3)	Corrosion protection, photocatalysis	145
	Molybdenum oxide (MoO_3)	Gas sensors, electrochromic devices, battery electrodes	54
	Tungsten oxide (WO_3)	Electrochromic devices, gas sensors, photocatalysis	146
7	Manganese oxide (MnO_2)	Supercapacitors, catalysts, batteries	147
8	Iron oxide (FeO)	Magnetic materials, catalysts	148
	Cobalt oxide (Co_3O_4)	Gas sensors, electrochromic devices, battery electrodes	149
9	Nickel oxide (NiO)	Supercapacitors, gas sensors, catalysts	150
12	Zinc oxide (ZnO)	UV filters, photocatalysis, gas sensors	151
	Cadmium oxide (CdO)	Solar cells, gas sensors, transparent conductive coatings	152
13	Aluminum oxide (Al_2O_3)	Catalyst supports, ceramics, abrasive materials	153
	Gallium oxide (Ga_2O_3)	Transistors, solar cells, gas sensors	154
	Indium oxide (In_2O_3)	Gas sensors, transparent conductive coatings	138
14	Silicon dioxide (SiO_2)	Integrated circuits, insulators, gas sensors	155
	Germanium oxide (GeO_2)	Optical fibers, gas sensors	156

Table 5 Optical, electronic, and electrical properties of 2D metal oxides

Metal oxide	Crystal structure	Lattice constant (Å)	Bandgap (eV)	Optical properties	Electronic properties	Electrical properties	Ref.
Group 2							
MgO	Rocksalt	4.21	7.8	UV transparent	Wide bandgap	Insulator	31
CaO	Rocksalt	4.81	5.5	UV transparent	Wide bandgap	Insulator	35
SrO	Rocksalt	5.15	5.4	UV transparent	Wide bandgap	Insulator	169
BaO	Rocksalt	5.82	4.3	UV transparent	Wide bandgap	Insulator	170
Group 3							
Al_2O_3	Corundum	4.75	8.8	UV transparent	Wide bandgap	Insulator	171
Group 4							
TiO_2	Rutile	4.59	3.0–3.2	UV transparent	Wide bandgap	Insulator or weakly conducting	38
	Anatase	3.78	3.2–3.5	UV transparent	Wide bandgap	Insulator or weakly conducting	41
Group 6							
MoO_3	Hexagonal	3.96	2.6–2.9	Transparent	Narrow bandgap	Semiconductor	43
WO_3	Orthorhombic	7.31 × 7.33 × 7.33	2.5–2.7	Transparent	Narrow bandgap	Semiconductor	146
Group 14							
SnO_2	Rutile	4.73	3.6–3.8	Transparent	Wide bandgap	Semiconductor	172
Group 12							
ZnO	Hexagonal	3.25	3.3–3.4	UV transparent	Wide bandgap	Semiconductor	173
Group 13							
Fe_2O_3	Hematite	5.03	2.2–2.2	Transparent	Narrow bandgap	Semiconductor	174
Group 9							
CoO	Rocksalt	4.26	2.7–3.0	Transparent	Narrow bandgap	Semiconductor	175
NiO	Rocksalt	4.17	3.5–4.0	Transparent	Narrow bandgap	Semiconductor	47

Because O may be combined with additional elements or in a range of stoichiometric ratios.[157] Fortunately, the presence of O helps most 2D oxides display remarkable air stability, and constituent elements of the materials reside in comparatively stable valence states. By spontaneously oxidizing liquid metals, 2D metal oxides like β-Ga_2O_3, β-TeO_2, and β-Bi_2O_3 may be created in an air environment. These materials also exhibit outstanding UV detecting capabilities. For example, Huihui Yu et al.[163] showed the response of 2×10^4 A W^{-1} with a good detectivity of 6.83×10^{14} Jones at a visible-blind wavelength of 254 nm, demonstrating the UV detection capabilities of 2D ZnO nanosheets. It is possible to use gallium oxide (β-Ga_2O_3), a particularly significant III–VI semiconductor with a broad band gap of 4.9 eV, as an alloy in sun-blind photodetectors. Due to several uses, such as missile tracking and ozone layer monitoring, the solar blind spectrum range has drawn a lot of interest.[164] Wei Feng et al.[164] produced 2D Ga_2O_3 polycrystalline, with a thickness in the region of 10 nm, displaying an extremely high photoresponsivity of 3.3 A W^{-1} at a solar blind wavelength of 254 nm with a good detectivity of 4.0×10^{12} Jones, and the MSM device exhibits an external quantum efficiency of 1600%.

Future infrared optoelectronic devices are likely to benefit from non-layered 2D materials, because of the synergistic effects of both the photoconductive and the bolometric mechanisms. This combination leads to exceptional sensitivity to light across a wide range of intensities. Such materials hold great promise for various optoelectronic applications including imaging, sensing, and communications, as they can detect a broad spectrum from ultraviolet (UV) to long-wavelength infrared (LWIR). At a wavelength of 10.6 μm, Fe_3O_4 nanosheets produced by space-confined chemical vapor deposition have a photoresponsivity of 561.2 A W^{-1}. With a detectivity of 7.42×10^{14} Jones and an external quantum efficiency of 6.6×10^3%, the material demonstrated its potential for sophisticated infrared detecting applications.[166] Particularly in free space ultraviolet communication, the detection of the polarization state at DUV wavelength is essential. Near the earth's surface, solar blindness results in a high signal-to-noise ratio and no noise because the atmosphere's ozone molecules absorb nearly all of the DUV radiation.[167] The use of polarization-sensitive photodetection will be demonstrated as a cutting-edge communication solution for non-line-of-sight communication and terrain characteristics. With a responsivity of 335 A W^{-1} in the region of pW illumination intensities, monoclinic β-Ga_2O_3 allows for the polarization sensitive detection of deep-ultraviolet light.[167] Solar blindness results in a high signal-to-noise ratio and no noise near the earth's surface because nearly all of the DUV radiation is absorbed by ozone molecules
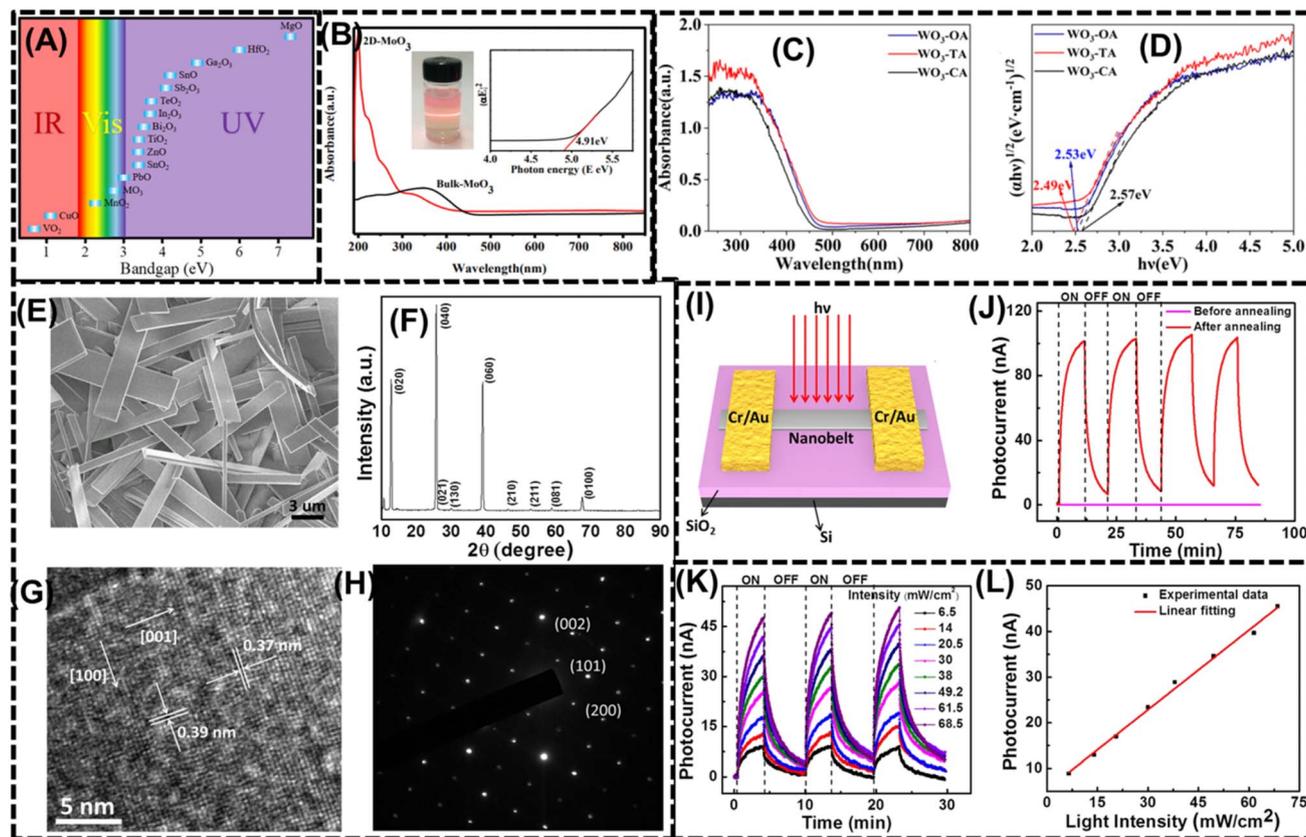
© 2026 The Author(s). Published by the Royal Society of Chemistry

Fig. 9 (A) Band gaps of 2D TMOs. Reprinted with permission from ref. 157 copyright of John Wiley & Sons 2022. (B) UV-visible absorbance spectra of the bulk and 2D MoO_3 suspension. Reprinted with permission from ref. 158 copyright of the Royal Society of Chemistry 2016. (C and D) UV-vis absorption spectra and related Tauc graphs of 2D WO_3 synthesised in citric acid (CA), oxalic acid (OA), and tartaric acid (TA) as carboxylic acid auxiliary agents. Reprinted with permission from ref. 162 copyright of MDPI 2022. (E–H) SEM image, XRD pattern, HRTEM image, and corresponding SAED pattern of 2D MoO_3 nanobelts. (I) Photodetector device based on a single MoO_3 nanobelt. (J) Time-dependent photoresponse of the photodetector device under 660 nm laser with an applied bias of 0.1 V. (K) Time-dependent photoresponse characteristics of the MoO_3 nanobelt device at 532 nm with variable laser power and 0.1 V bias. (L) Plot of the photocurrent as a function of laser illumination intensities. Reprinted with permission from ref. 165 copyright of Nature 2014.

in the atmosphere. This makes the detection of the polarization state in DUV wavelengths essential, particularly in free space ultraviolet communication.[167] Fig. 9(E)–(H) shows the structural properties of 2D MoO_3 nanobelts using SEM, XRD, HRTEM, and related selected area electron diffraction (SAED) patterns. Xiang *et al.* disclosed the nanobelts' structural, crystallinity, and shape properties.[165] The photodetector device based on a single MoO_3 nanobelt is presented in Fig. 9(I), illustrating a possible use for the material that was synthesized. The time-dependent photoresponse of the photodetector device under 660 nm and 532 nm laser illuminations, respectively, is shown in Fig. 9(J) and (K), which offer insights into operation in various scenarios. A plot of the photocurrent *vs.* laser illumination intensities is shown in Fig. 9(L), which provides a numerical evaluation of the MoO_3 nanobelt photoresponse. When taken as a whole, these illustrations add to a thorough knowledge of the optical, structural, and photoresponsive characteristics of 2D TMOs, especially WO_3 and MoO_3, with possible ramifications for optoelectronic uses. Table 5 shows the optical and electrical and electronic properties of 2D metal oxides. The crystal structure, lattice constant and band gap of these metal oxides are given in this

Table 5. The optical characteristics of 2D oxides are very different from those of their bulk counterparts because of the quantum size effect. Most 2D oxides have special electrical properties and are semiconductors. For instance, 2D MoO_3 can display varied forms of conductivity and, in certain situations, even insulating qualities depending on how it is formed. Due to their highly adjustable electrical behavior, 2D oxides have potential uses in energy devices, electronics, and optoelectronics.[157] MgO is an insulator characterized by a substantial bandgap close to 7 eV contributing to its insulating properties. The relatively smaller bandgap observed in MgO nanoparticles enhances their reactivity.[168]

5.2 Polarization and polaritons arising from polar phonons

The optical properties of 2D LMOs have attracted much attention, with the promise of their use in future optoelectronic devices.[176] Among these properties, the formation of polaritons as quasiparticles resulting from the strong coupling between photons and lattice modes, namely longitudinal optical (LO) phonons, is one that has witnessed an extremely vigorous area

of research. In 2D materials, such coupling leads to strange polariton modes with characteristic dispersion properties, strong confinement, and enhanced light–matter interactions. Such features enable functionalities difficult to achieve in conventional three-dimensional materials, thus making 2D metal oxides a promising platform for mid-infrared and terahertz photonics. Juraschek *et al.* shows that monolayer $LiNbO_3$ enables strong light confinement, offering high-quality 2D phonon–polaritonic propagation in the terahertz regime comparable to hBN.[177] This confinement can enhance nonlinear optical effects and control correlated phases such as the paraelectric-to-ferroelectric transition observed in $SrTiO_3$ and $KTaO_3$. Thus, $LiNbO_3$ stands out as a promising 2D platform for advanced optoelectronic and polaritonic applications. Wang *et al.* showed that phonon polaritons (PhPs) in a single natural α-MoO_3 crystal exhibit highly directional, diffraction-free propagation with lateral confinement ratios up to $\lambda_0/50$.[178] Unlike complex metasurfaces or twisted heterostructures requiring precise magic angles or graphene doping, this system achieves high-quality canalization under simple conditions. Such efficient PhP control enables nanoscale energy transfer, imaging, and nonlinear optical applications. Coupling of the photons and the LO phonons in 2D metal oxides is described by using the Lyddane–Sachs–Teller (LST) relation between the static and high-frequency dielectric constants with the longitudinal and transverse phonon frequencies. For example, in α-MoO_3, in-plane polar phonon frequencies range between approximately 545 cm^{-1} and 995 cm^{-1}, or 67 and 123 meV, and dielectric constants along different crystallographic directions between 4.5 and 6.8.[179] These parameters determine the splitting of the upper and lower polariton branches and directly influence the resulting wavelength and propagation characteristics of the polaritons. Experimental research using infrared nano-imaging has shown the presence of long-range highly localized phonon polaritons in α-MoO_3 with propagation lengths of more than 5 μm for mid-infrared wavelengths (∼10 μm), which confirms the capability of 2D oxides to support long-lived polaritonic modes.[180]

One of the fascinating properties of polaritons in 2D metal oxides is their external tunability by strain, electric fields, or chemical functionalization. In mechanically exfoliated α-MoO_3 flakes, uniaxial strain as low as 1–2% can adjust the polariton resonance by ∼5–10 meV, allowing for direct tunability of wavelength and optical mode confinement.[181] Similarly, chemical doping of systems like TiO_2 nanosheets with cationic Nb^{5+} or W^{6+} modifies the local dielectric environment and carrier concentration, triggering observable phonon polariton energy shifts.[182] Such tunability is significant for the nanophotonic device design as it allows dynamic modulation of light propagation, absorption, and emission at the nanoscale. Hyperbolic dispersion is another interesting property exhibited by a few 2D metal oxides. Hyperbolic phonon polaritons occur when the dielectric permittivity along orthogonal directions has opposite signs, resulting in highly anisotropic light propagation.[183] For instance, in α-MoO_3, the dielectric tensor exhibits hyperbolic dispersion within the mid-infrared range, enabling modes with extremely large in-plane wavevectors.[184] The high-momentum

polaritons enable sub-diffractional confinement of light with effective mode volumes several orders of magnitude smaller than free space wavelength. Increasing light–matter interactions, the hyperbolic polaritons are especially suitable for sensing, nano-imaging, and amplified nonlinear optics. Experimental techniques such as scattering-type scanning near-field optical microscopy (s-SNOM) and Fourier transform infrared (FTIR) spectroscopy have played a crucial role in mapping the dispersion and propagation of polaritons in 2D metal oxides. With s-SNOM studies on α-MoO_3 and V_2O_5, polariton wavefronts of wavelengths as short as 200–300 nm have been mapped, far below the diffraction limit.[185] These results highlight the promise of 2D oxides to confine electromagnetic energy at sizes compatible with nanoscale photonic integrated circuits. In addition, numerical simulations based on finite-difference time-domain (FDTD) methods have validated experimental results, providing quantitative details on mode profiles, propagation length, and confinement factor. Phonon–electron interaction in 2D metal oxides also helps with complex optical phenomena such as strong coupling and enhanced nonlinear responses. In materials like Nb-doped TiO_2 nanosheets, free carriers give rise to plasmon–phonon hybridization, resulting in coupled plasmon–phonon polaritons, whose energies are tunable by tens of meV.[186] Hybrid modes share both phonon polariton confinement and the high field intensities of plasmonic resonances, which offer the prospect of realizing mid-infrared modulators, nanoscale detectors, and energy-preserving optoelectronic switches.

Applications of polaritons in 2D metal oxides extend beyond photonics to sensing and energy technology. Polariton-supported infrared sensing, for instance, has been proved to exhibit higher sensitivity for sensing the molecular vibration in adsorbed analytes. In α-MoO_3 flakes, infrared absorption was enhanced up to 15 times by local field enhancement of phonon polaritons, enabling the detection of trace levels of organic molecules.[187] Similarly, TiO_2 and V_2O_5 nanosheet polaritons have also been used to enhance the photocatalytic performance, where restricted electromagnetic fields drive the generation of excitons as well as efficiency in charge separation, thus enhancing speeds of reaction under mid-infrared light. From a device perspective, the integration of 2D metal oxides into van der Waals heterostructures further advances the potential for polaritons. Tunable hybrid polaritons with controlled group velocity and direction of propagation can be achieved through the overlap of α-MoO_3 or other 2D oxides with graphene or hexagonal boron nitride.[188] In a demonstration experiment, the combination of α-MoO_3 and monolayer graphene allowed for electrical gating to control the wavelength of the polariton within ∼50 nm, proving the usability of electrically reconfigurable nanophotonic devices.[189]

Theoretical studies also provide critical insights into the fundamental mechanisms of polariton creation and propagation.[190] Phonon frequencies, dielectric functions, and electron–phonon coupling amplitudes have been computed using density functional theory (DFT) and density functional perturbation theory (DFPT) calculations in various 2D metal oxides.[191] For example, calculations for monolayer V_2O_5 suggest polar

phonon frequencies at 750–950 cm^{-1} and strong in-plane dielectric anisotropy, consistent with measurements of hyperbolic polariton modes.[192] Such computational predictions guide material selection and device design by predicting which 2D oxides will host strong, tunable polaritons. Sufficient challenges are still in the real-world utilization of polaritons in 2D metal oxides despite remarkable advances. High-quality, large-size flakes with minimal defects and controlled thickness are necessary to produce, as defects can create damping and scattering that limit polariton lifetimes. Interlayer interactions in heterostructures need precise control to achieve required polariton dispersion. To overcome these issues, the further improvement of synthesis techniques such as chemical vapor deposition, liquid-phase exfoliation, and molecular beam epitaxy is essential. Polaritonics on polar phonons in 2D metal oxides is a newly developing and technologically significant field.[193] The combination of strong light–matter interaction, hyperbolic dispersion, external-stimulus tunability, and integration in heterostructures provides a unique platform for next-generation nanophotonic, sensing, and optoelectronic devices. With continued innovation in the synthesis of materials, characterization, and theoretical modeling, polariton-based 2D metal oxide devices have the potential to usher in revolutionary progress in infrared photonics, mid-infrared sensing, and energy-efficient optoelectronics.

5.3 High mobility electronics

High-mobility 2D charge carriers can exist in both integer and fractional quantum states, and due to their relatively broad band gap, low power switching, and availability of vast area growth methods, 2D metal oxide semiconductors are emerging as promising alternatives for next-generation thin-film electronics.[194–196] The 2D carriers also show remarkable phenomena when their mobility increases, including denominator fractional states. Zero-resistance states are caused by microwaves and the 2D metal–insulator transition.[197] Extreme mobility SrTiO$_3$ heterostructures were effective in producing 2D electrons. It was shown that the transition to the 2D superconducting state occurred in addition to the well-known 2D Shubnikov–de Haas oscillation. Excellent charge carrier mobility enables electrons and/or holes to flow quickly through materials in high mobility devices. Compared to conventional silicon-based electronics, which typically have 200–250 cm^2 V^{-1} s^{-1} for holes and 100–1500 cm^2 V^{-1} s^{-1} for electrons, some 2D LMOs including MoO$_3$ have higher charge carrier mobilities. The high electron and hole mobilities of 2D LMOs enable high-speed electronic devices with improved performance, reduced power consumption, and increased signal processing capacity. For next-generation high-frequency transistors, high-performance sensors, and other electronic devices where high mobility is required for optimal device functioning, these qualities have enormous promise.

Another oxide that is anticipated to have high electron–electron correlation effects that are reflected by the interaction parameter is the MgZnO/ZnO heterointerface.[197] Low-temperature magnetotransport of 2D electron gas occurs with an increased electromobility of 300 000 cm^2 V^{-1} s^{-1} in a magnetic field up to 26 T.[197] Charge-transport properties are thought to be less susceptible to orientation in spherical ns-type orbitals, despite the fact that these orbitals are often the relevant atomic orbitals for electron transport in metal oxides. The energy band structure of monolayer, bilayer, and trilayer MoO$_3$ is examined using two computational methods: the optB88-vdW functional (Fig. 10(A)) and the HSE06 functional (Fig. 10(B)).[198] Fig. 10(C) and (D) provide a visual representation of the charge distribution in the valence band maximum (VBM) and conduction band minimum (CBM) of monolayer MoO$_3$, respectively. These images illustrate where electrons are most likely to be found in these critical energy states, offering insights into the electronic structure of the material. In particular, the isosurface value in Fig. 10(D) is set to 0.1 electrons per cubic bohr, which helps reveal fine details in the charge density distribution. Such results are important for understanding how charge carriers behave in the material. In contrast, in conventional semiconductors like silicon and organic materials, charge transport is primarily governed by highly directional hybridized sp-type orbitals, which create well-defined pathways for electron movement.[199,200] This comparison highlights the potential differences or similarities in charge transport mechanisms between MoO$_3$ and more traditional semiconductors. Effective charge transfer is made possible by the covalent bonds formed by the sp^3 hybridization of silicon atoms, which results in a well-defined band structure. Charge carriers can move across organic semiconductors due to the overlapping π-orbitals produced by the sp^2 hybridization of carbon atoms in conjugated systems. The electrical characteristics and charge transport efficiency of silicon and organic semiconductors are significantly influenced by the directed bonding nature of the orbitals. It has been suggested that long-range structural order has little influence on the hopping rate in n-type metal oxide semiconductors, giving them a distinct advantage over conventional semiconductors due to their unique charge transport properties. In contrast, p-type metal oxide semiconductors rely heavily on the directional nature of oxygen 2p orbitals for hole transport. This dependence leads to much lower mobilities, especially in disordered p-type oxide transistors. The fundamental difference in transport mechanisms between n-type and p-type oxides underscores the challenges in optimizing the performance of p-type materials, making them less efficient than their n-type counterparts.[195,199,201] Fig. 10(E) presents the current–voltage (I–V) and capacitance–voltage (C–V) characteristics of a HfO$_2$-based capacitor with an aluminum (Al) top electrode and a heavily doped n-type silicon (n$^+$-Si) bottom electrode. These measurements offer insights into the dielectric behavior and charge storage capability of the capacitor structure. Meanwhile, Fig. 10(F) shows the drain current versus gate-source voltage (I$_{DS}$–V$_{GS}$) characteristics of a device composed of an Al/SnO$_2$ (20 nm)/HfO$_2$/n$^+$-Si stack. This plot reveals how the device responds electrically under varying gate voltages, highlighting its potential for transistor applications and providing key information on its switching behavior and threshold voltage.[202] Similarly, Fig. 10(G) and (H) showcase various characteristics such as I$_{DS}$–V$_{DS}$, I$_{DS}$–V$_{GS}$, μ$_{FE}$–V$_{GS}$, and
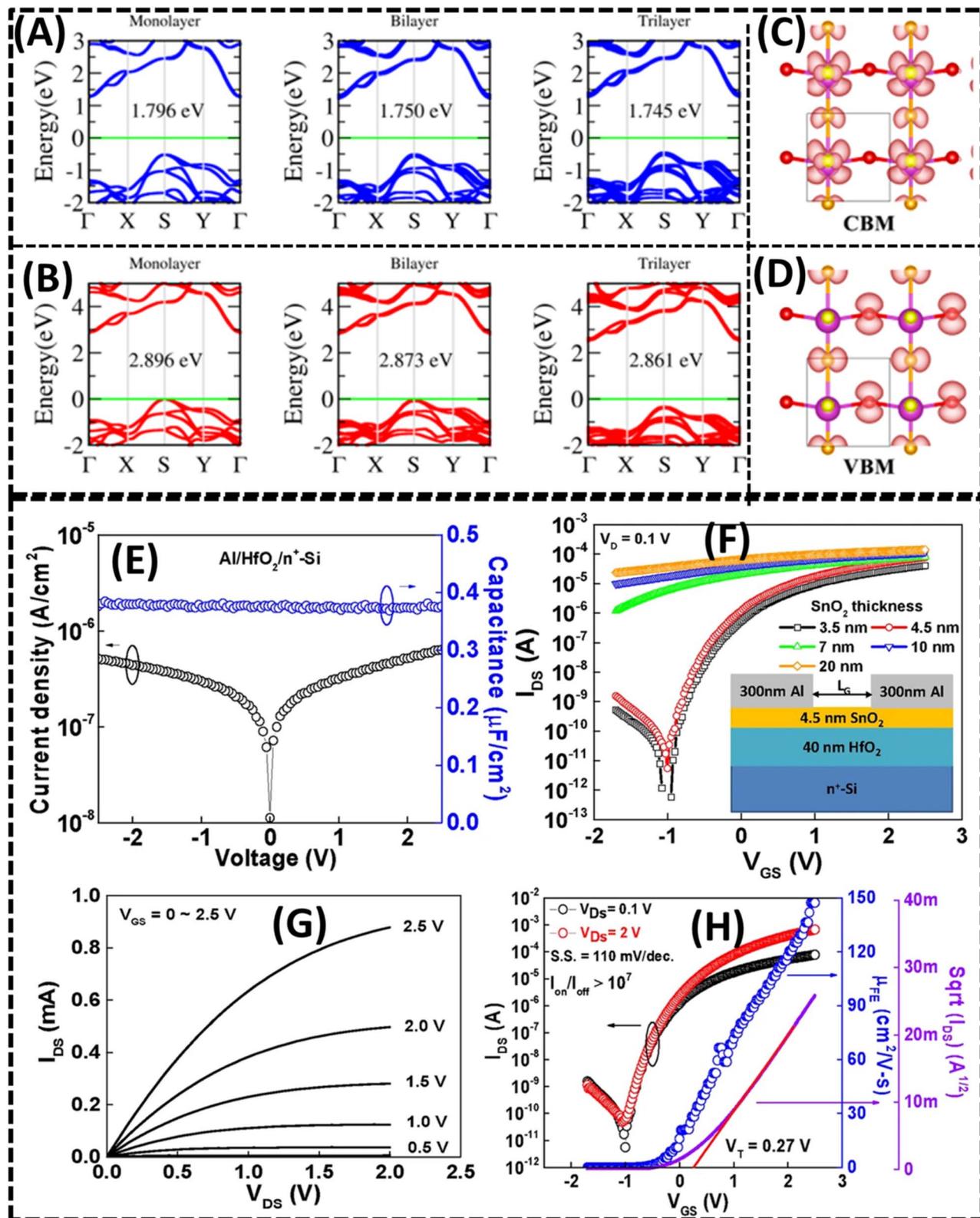
Fig. 10 Energy band structure of monolayer, bilayer, and trilayer MoO_3 using the (A) optB88-vdW functional and (B) HSE06 functional. (C) Charge densities of the conduction band minima (CBM) for monolayer MoO_3. (D) Charge density of valence band maxima (VBM) for monolayer MoO_3 in which the isosurface value is set to 0.1 e bohr^{-3}. Reprinted with permission from ref. 198 copyright of the American Chemical Society 2017. (E) Current–voltage (I–V) and capacitance–voltage (C–V) characteristics of the capacitor of HfO_2 with top Al and bottom n$^+$-Si electrodes. (F) I_{DS}–V_{GS} characteristics of Al/SnO_2 (20 nm)/HfO_2/n$^+$-Si. (G and H) I_{DS}–V_{DS}, I_{DS}–V_{GS}, μ_{FE}–V_{GS}, and (I_{DS})$^{1/2}$–V_{GS} characteristics of Al/SnO_2 (4.5 nm)/HfO_2–n$^+$-Si with a gate length of 50 μm. Reprinted with permission from ref. 202 copyright of Nature 2016.

$(I_{DS})^{1/2}$–V_{GS} for an Al/SnO$_2$ (4.5 nm)/HfO$_2$–n$^+$-Si structure with a gate length of 50 μm. These results collectively provide a comprehensive understanding of the electrical performance and characteristics of the studied devices. Together, these results demonstrate the potential of these structures for advanced electronic applications and underscore the effectiveness of integrating SnO$_2$ and HfO$_2$ in high-performance device architectures.

5.4 High k-dielectrics

Comprehending the influence of size on high-k thin films is crucial due to the increasing need to develop smaller devices for enhanced effectiveness and performance. Researchers have tried to increase capacitance in smaller places using high-k materials, but nearly invariably, nanoscale devices have produced lower capacitance values than anticipated. These low values have hampered the performance of thin-film capacitors and hindered further device miniaturization.[203] High k-materials are being actively sought for applications in nanoelectronics such as memory, capacitors, gate insulators, energy storage, and high-frequency modulation in communication devices.[203] A number of material systems are now being studied as possible substitutes for SiO$_2$ as the gate dielectric material in sub-0.1 μm complementary metal–oxide–semiconductor (CMOS) technology. Wilk, Wallace, and Anthony have determined a number of important factors to consider while choosing a different gate dielectric. These consist of film morphology, thermodynamic stability, permittivity, band gap, band gap alignment, and interface quality. These elements are essential for guaranteeing that the substitute material can satisfy the demanding performance and dependability specifications for CMOS devices of the future.[204] Material systems including Ta$_2$O$_5$, SrTiO$_3$, and Al$_2$O$_3$ are the most often researched high-k gate dielectric competitors. Their dielectric constants range from 10 to 80, and they have been used mostly due to their maturity in memory capacitor applications.[204] Depending on the polarity of the applied bias, Ta$_2$O$_5$ displays both Frenkel–Poole and Schottky transport mechanisms under normal voltage bias circumstances. A defect band, located near the conduction band in the Ta$_2$O$_5$ thin film, has been identified as the origin of the transient current observed in the material. This defect band plays a crucial role in the charge transport process, influencing the material's electrical behavior under different bias conditions.[204,205]

In Fig. 11, various aspects of a MOS (metal–oxide–semiconductor) capacitor structure and field-effect transistors (FETs) are presented. In Fig. 11(A), the HfO$_2$/Ga$_2$O$_3$ MOS capacitor structure is depicted along with its band diagram, providing a schematic representation of the energy levels in the device.[206] The observed and computed ideal capacitance–voltage (C–V) curves for a 40 nm HfO$_2$ layer over Ga$_2$O$_3$ are shown in Fig. 11(B). Favorable electrical properties for the capacitor are indicated by the observed positive shift in the C–V curves, as well as exceptionally low hysteresis and stretch-out. A $1/C^2$–V plot obtained from the C–V sweeps is used for further analysis in Fig. 11(C), producing an apparent carrier density of 2.1×10^{17} cm^{-3}. This

analysis provides insights into the electronic properties of the material and confirms the high-quality performance of the capacitor structure. This plot helps in determining the carrier concentration in the semiconductor. If the ideal stoichiometry could be achieved, 2D LMOs would be insulating dielectrics. However, during low-temperature deposition procedures, it is difficult to attain the optimal stoichiometry of low temperatures to completely oxidized metals.[207] These metal oxides are readily reduced because the additional electrons created by the oxygen vacancies occupy the d-orbitals of neighboring metal atoms. The primary group metal oxide has limitations in terms of both reduction and the corresponding rise in conductivity.[207,208] The manufacture of microelectronic devices that work consistently at ever-smaller dimensions is driven by the rising demand of semiconductor industry.[209] Future device development will be critically impacted by the requirement for insulating films of nanometer-scale thickness that exhibit good compatibility with semiconductor technology.[209] Conventional SiO$_2$ dielectric gate thickness has poor insulating character with substantial leakage current due to quantum tunneling when the film thickness scales down to 10 nm, resulting in significant energy consumption and declining device dependability.[209,210] However, high dielectric constant (high-k) metal oxide gate dielectrics provide high capacitance without requiring a thick layer, enabling effective charge injection and thus lowering tunneling leakage currents.[209] For applications requiring an additional degree of freedom to fine-tune photonic heterostructures or demanding spin coherence in quantum devices, 2D van der Waals MoO$_3$ has also been demonstrated to be a competitive alternative to h-BN as a 2D dielectric insulator.[211] The three crystal axes of MoO$_3$ have some of the highest recorded refractive indices for 2D materials. By reporting line-width narrowing and decreased inhomogeneous widening of 2D excitons and optically active quantum emitters in a prototype monolayer transition metal dichalcogenide semiconductors, researchers also show that MoO$_3$ is suitable for dielectric encapsulation.[211] Kim et al.[212] showed that a TiO$_2$ thin film with a high dielectric constant of 83–100 was produced at 250 °C utilizing the atomic layer deposition technique. Due to its excellent dielectric constant, (Ba, Sr)TiO$_3$ is the most promising material for high-k thin films. Among the binary metal oxides, rutile-structured TiO$_2$ has an extremely high k value along the c-axis and 90 along the x-axis.[213] Since Ti vacancies are found in Ti$_{0.87}$O$_2$ nanosheets, oxygen vacancies are not anticipated in this system. These nanosheets have been shown to behave as high-k nanoblocks, and their multilayer films show a high dielectric constant of 125 at thicknesses as little as 10 nm. TiO$_6$ octahedral, an essential component of Ti-based dielectrics, is present in the 2D structure of elemental Ti$_{0.87}$O$_2$ nanosheets.[203,214] By enabling customization of composition and film structures, oxide nanosheets meet these objectives. Next-generation electronic devices need materials with outstanding high-k performance more than 100, such as Ca$_2$Nb$_3$O$_{10}$ nanosheets, which display this even at nanoscale thickness. High-k dielectrics, also known as high-k materials, have a greater dielectric constant (k) than typical silicon dioxide (SiO$_2$) dielectrics. The dielectric constant measures this capacity, and a larger k value shows the ability of material to retain more charge when an electric field is applied. High-k dielectrics
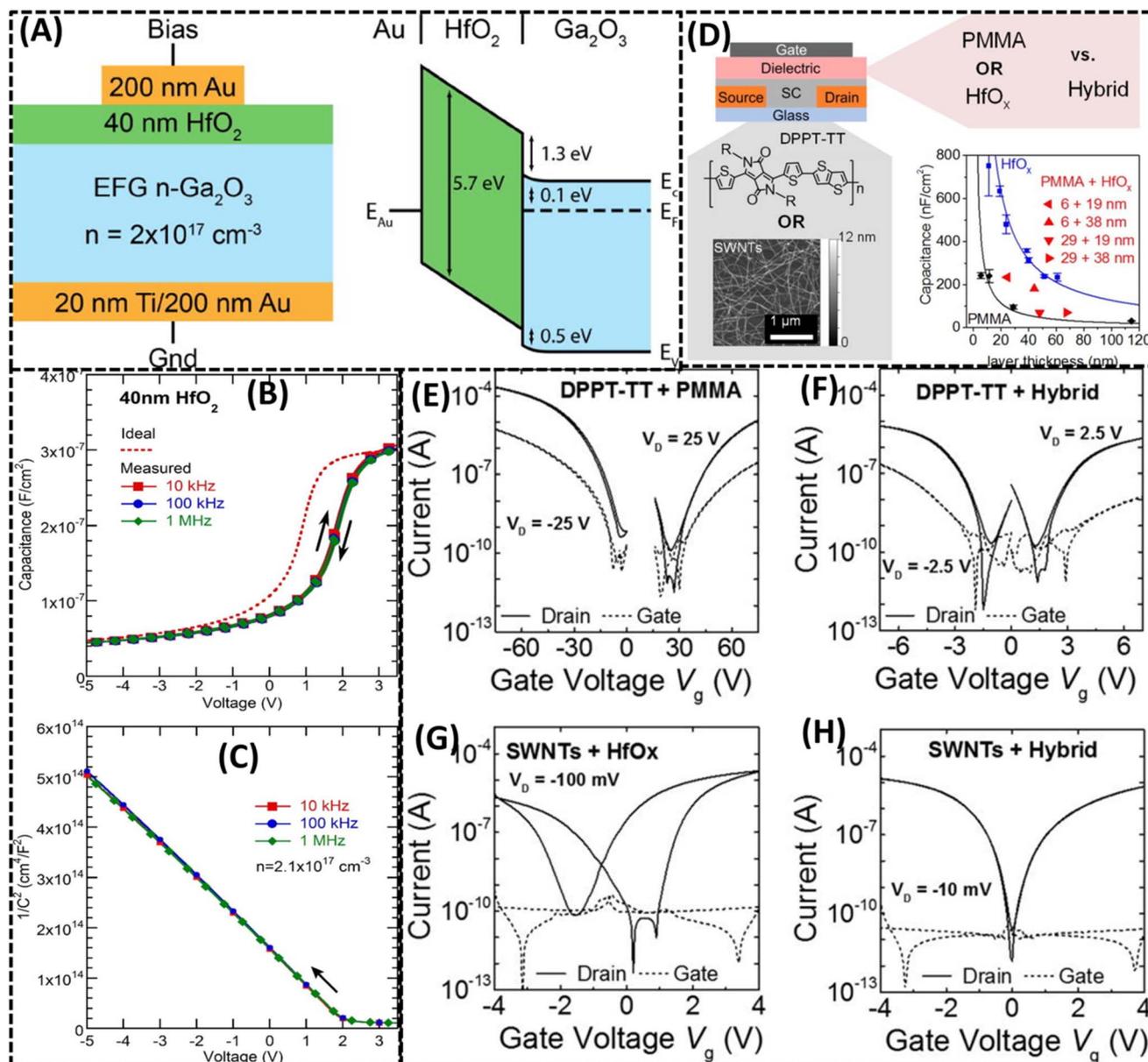
Fig. 11 (A) HfO_2/Ga_2O_3 MOS capacitor structure with their band diagram. (B) For 40 nm HfO_2 on Ga_2O_3, ideal $C-V$ curves were measured and calculated; these curves show a positive shift with little stretch-out and hysteresis. (C) $1/C^2-V$ plot for $C-V$ sweeps from 3.5 V to −5 V, which results in an apparent carrier density of 2.1×10^{17} cm^{-3}. Reprinted with permission from ref. 206 copyright of AIP Publishing 2018. (D) Top-gate and bottom-contact FET architecture with capacitance as a function of total layer thickness using various semiconductors (DPPT-TT and SWNT network) and dielectrics (HfO_x, PMMA *vs.* hybrid dielectric). Transfer properties of FETs with (E) PMMA and (F) PMMA/HfO_x. The semiconductor is DPPT-TT. Network SWNT FETs with (G) HfO_x dielectric and (H) PMMA/HfO_x dielectric exhibiting transfer performances with channel widths of 125 and 40 μm. Reprinted with permission from ref. 215 copyright of AIP Publishing 2015.

are used in semiconductor devices to overcome the limitations of SiO_2 in modern integrated circuits. As transistors and other electronic components are miniaturized in semiconductor technology to boost the efficiency and decrease the power consumption, the thickness of the gate dielectric (insulating layer) must be decreased. However, the tendency of gate dielectric of traditional SiO_2 thickness decrease leads to a rise in leakage current and power dissipation because of quantum mechanical tunneling effects. Fig. 11(D) shows the top-gate, bottom-contact FET shape with various semiconductors (DPPT-TT and SWNT network) and

dielectrics (HfO_x, PMMA *vs.* hybrid dielectric).[215] The capacitance provides important information about the dielectric characteristics of the FETs, and is displayed as a function of the total layer thickness. The transfer characteristics of FETs using DPPT-TT as the semiconductor, each including a different dielectric material are shown in Fig. 11(E) and (F). In particular, the transfer properties of PMMA are displayed in Fig. 11(E), whereas PMMA/HfO_x is featured in Fig. 11(F). These curves show how input and output of the transistor are related, giving important details regarding its electrical operation, such as how it switches and how efficient it is
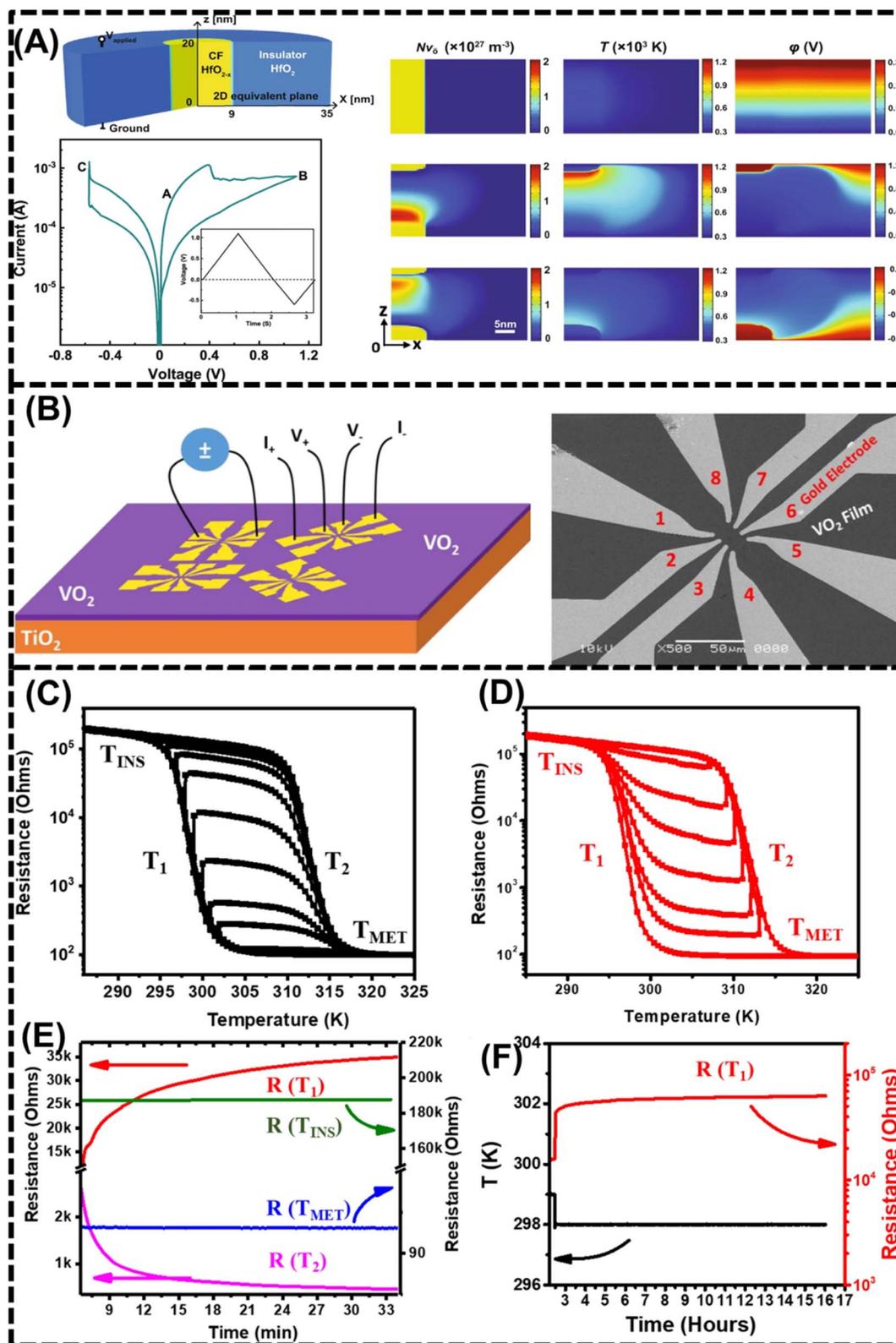
Fig. 12 (A) Simulation size and geometry for the phase-field of resistive switching with current–voltage hysteresis behavior, and simulated 2D spatial profiles of concentration N_v, with applied potential of 0.3 V, 1.1 V and −0.57 V set state. Reprinted with permission from ref. 217 copyright of Nature 2020. (B) Diagram of the device design showing a VO_2 film grown on a TiO_2 substrate with photolithographically produced Au electrodes for two-probe and four-probe configurations, along with the accompanying picture from a scanning electron microscope. (C) When cool-down is reversed during the transition close to T_1, there are several stable resistance states. (D) Conditions in the scenario where warming reversed during the transition close to T_2. (E) When the temperature is fixed at T_1 during cooling or (F) at a certain T_2 during heating, the time-evolution of various resistive states shows the insulating state at T_{INS}, the metallic state at T_{MET}, and an intermediate state. When the temperature is changed from 299 K to 298 K, the stability of the intermediate state following initial relaxation is displayed by the $R(T_1)$ on a linear scale vs. longer time scale. Reprinted with permission from ref. 220 copyright of Nature 2020.

overall. Fig. 11(G) and (H) present the transfer characteristics of network SWNT FETs with different dielectrics, including HfO$_x$ (Fig. 11(G)) and PMMA/HfO$_x$ (Fig. 11(H)). The channel width and channel lengths are specified for each case, demonstrating the impact of dielectric materials on the transistor behavior. High-k dielectrics enable the use of thicker gate dielectric layers while yet maintaining high capacitance, reducing leakage current and improving transistor performance. There are a few common high-k dielectric materials including hafnium oxide (HfO$_2$), zirconium oxide (ZrO$_2$), and aluminium oxide (Al$_2$O$_3$). High-k dielectrics, which have eased the development of complex transistors and memory components and opened the way to more potent and energy-efficient electronic devices, are essential to modern semiconductor technology.

5.5 Resistive switching

By applying an electrical field, a novel kind of memory device known as a non-volatile resistive switching (NVRS) device also known as an atomristor or memristor in atomically thin materials allows the device resistance to transition from a high-resistance state to a low-resistance state.[216] In Fig. 12(A), the simulation size and geometry for the phase-field of resistive switching are depicted, showcasing the current–voltage hysteresis behavior. Simulated 2D spatial profiles of concentration (N_v) are illustrated at different applied potentials, providing insights into the resistive switching mechanism.[217] Although lateral structures in 2D structures can provide a second terminal for field-effect control, they are unable to achieve the same integration density as two-terminal vertical memory devices. Furthermore, a large switching voltage of up to 20–100 V is required since the gas fluttering the 2D structure between two lateral electrodes has been on the order of micrometers. Resistor switching is a phenomenon in which resistance of a material may flip between high and low states without any need for heat. The presence of external electricity or other sources of energy may result in this shift in resistance. Resistor switching "ON" and "OFF" states of device are represented by two resistance states that correspond to different electrical conductivity levels. The resistor switching process produces and removes conductive hairs or material flaws. When a high enough voltage is supplied, conductive channels form, leading to an ON state with low resistance. However, these conductive channels may be linked or detached by the opposing voltage applied, creating a high-resistance state (OFF state) that results in resistive random access memory (RRAM) or resistive random access memory (ReRAM) outcomes. Due to its potential application in non-volatile memory systems, resistive switching devices have attracted a lot of attention. Compared to traditional memory technologies like flash memory, these devices provide advantages such as faster switching rates, reduced power consumption, and improved resistive switching scalability. Additionally, research has been conducted in related domains including memristive systems and neuromorphic computers, where it may be utilized to replicate biological synapses and some aspects of neuron behavior. Although research in this area is still in its early stages, it might play a significant role in neuromorphic computing systems and non-volatile memory. However, conventional thinking in metal oxides maintains that resistance switching cannot scale below a few nanometers because of excessive leakage. The initial demonstration of NVRS in monolayer MoO$_3$ and h-BN sandwiched between two metal electrodes changed the state of knowledge. By decreasing the inter-electrode spacing to sub-nanometer, this produced the thinnest memory cells with switching voltages of 0.5–3 V.[218,219]

Fig. 12(B) presents the schematic of the device structure, which consists of a VO$_2$ film grown on a TiO$_2$ substrate. The device is equipped with Au electrodes, fabricated using photolithography, and is designed to operate in both two-probe and four-probe measurement configurations. This setup enables precise characterization of the electrical properties of the VO$_2$ film, facilitating the study of its transport behavior and phase transition characteristics.[220] An additional picture of the real gadget is provided by the accompanying scanning electron microscopic image. In Fig. 12(C) and (D), depending on whether the heat-up or cool-down process is reversed, there are several stable resistance states during the transition close to T_1 and T_2. These states provide insights into the device's intricate resistive switching behavior. The time-evolution of several resistive states is shown in Fig. 12(E). These states include the metallic state at T_{MET}, the insulating state at T_{INS}, and an intermediate state when the temperature is set at T_1 during cooling or at a specific T_2 during heating. This dynamic perspective aids in comprehending how resistive states change throughout time. The stability of the intermediate state following the first relaxation while adjusting the temperature from 299 K to 298 K is demonstrated by Fig. 12(F), which displays the resistance (R) at T_1 on a linear scale across a larger time scale. This information is crucial for assessing the reliability and durability of the resistive states. The findings contribute to understanding the underlying mechanisms and the stability of different resistive states, offering valuable insights for potential applications in memory devices or other electronic systems. One of the most promising next-generation nonvolatile memories, resistive random access memory, has been regarded a good choice for 2D layered materials. Most devices still have poor environmental stability, defect-inducing complexity, and uncontrollability as a result of many sorts of defects.[221] Wang *et al.*[221] developed layered memory cells with good unipolar nonvolatile resistive switching behavior and high-quality 2D α-MoO$_3$ nanosheets that can be thinned to 8.6 nm. This memory device exhibits good temperature endurance, allowing for lower SET/RESET voltages and a memory window greater than 104 at 380 K, indicating its potential for use in real-world applications.[221] For use in the upcoming generation of nonvolatile memory applications, binary transition metal oxides for resistive switching memory devices are gaining a lot of attention.[222] Binary LMO materials have been investigated because of their basic compositions that are easy to control during manufacturing. In resistive switching access memory, the names unipolar and bipolar switching behaviors have been used to describe the switching behavior between a high-resistance state and a low-resistance state.[222] When sandwiched between two electrodes and subjected to an applied voltage, many 2D LMOs display changed conductivity, which offers significant potential for the creation of resistive switching components like memristor.[5]

Yang *et al.*[222] enumerate the steady and repeatable bipolar resistive switching behavior of bipolar electrical features of Ti/MnO_2/Pt devices. The dependence of memory behavior on cell size and operating temperature leads one to believe that the locally produced conducting filaments are responsible for the conducting mechanism in low-resistance states.[222] Recently, there has been a lot of interest in devices that take advantage of the creation of a conductive interface between two insulating oxides, which is usually the outcome of a two-dimensional electron gas.[223] It is shown how to use a 2D electron gas between an amorphous Al_2O_3 layer and a $SrTiO_3$ substrate to create a non-volatile resistive switching device.[223] It is suggested that this switching mechanism is filamentary in nature and forms inside the Al_2O_3 layer as a result of oxygen vacancies being forced into the insulating Al_2O_3 from the interface by a strong electric field.[223] Miron *et al.*[223] demonstrates that at a current compliance of 0.1 mA and a voltage range of −6 to −4 V, the Pt/Al_2O_3/STO structure was visible. Following formation, 10 *I–V* sweeps were used to examine the structures. A forward voltage sweep from 7.5 to −7.5 V makes up each plot. When it comes to set and reset events, the *I–V* findings show strong and abrupt switching.[223] On the lattice-matched substrate of $SrTiO_3$, heteroepitaxial Pt/Pb($Zr_{0.52}Ti_{0.48}$)O_3/$SrRuO_3$ junctions display highly repeatable switching events at well-defined electric fields.[224] Given that the normal *I–V* characteristic displays two separate stable resistance states, the observed resistive switching might be due to the ferroelectric barrier's polarization reversal.[224] Qin *et al.*[225] reported on the behavior of universal resistive switching in nominally symmetric epitaxial grown tunnel junctions made up of two 20 nm-thick $LaSrMnO_3$ electrodes spaced apart by a ferroelectric $PbZrTiO_3$, ferroelectric $BaTiO_3$, or paraelectric $SrTiO_3$ tunnel barrier. These devices demonstrate enormous resistive switching resistance of 10^6 Ω with junctions of thin barriers up to 2–3 nm.[225] However, nonvolatile resistive switching memory made of a Pt/Co:ZnO/Pt structure demonstrates magnetic modulation along with alternating set and reset processes in addition to stable bipolar resistive switching properties.[226]

5.6 Supercapacitor batteries and thermoelectric applications

Three different forms of energy conversion and storage technologies, namely batteries, thermoelectric applications, and supercapacitors, all have significant uses. Reversible charges at the electrode-electric interface are also known as electrical double-layer capacitors (EDLCs) or supercapacitors. In contrast to traditional batteries, which use a chemical process to expel and store energy, supercapacitors do so using electricity. They can be charged and drained considerably more quickly than batteries due to their enormous capacity. In contrast to batteries, they typically have low voltage. Supercapacitors are utilized in a range of sectors, such as the automotive, electronics, and renewable energy systems, for short-term energy storage, peak voltage flexibility, and quick power delivery. One kind of energy storage device is a battery, which releases chemically stored electricity. It consists of a minimum of two electrical cells connected in parallel or series. Supercapacitors

have a larger capacity than batteries; however, batteries may charge and discharge more slowly. It is widely used in many applications, such as grid-scale energy storage, electric automobiles, portable devices, electric vehicles, and lithium-ion, lead-acid, nickel, and metal hydride batteries, depending on the energy level and cycle life. Different battery types may be added to the system to satisfy various demands. Thermoelectric materials may convert heat energy into electricity or the other way around due to the Seebeck effect. An electric current is created when there is a temperature differential within the item. However, the Peltier effect causes a temperature differential when an electrical current passes through the substance. Remote power sources, electronic device cooling, and power generation from waste heat all employ thermoelectric materials. The performance of thermoelectric materials is currently being improved for widespread use in energy conversion applications, although their efficiency is still limited. γ-WO_3 favors Li^+ transport with a diffusion barrier of 0.25 eV and a coefficient of 9.31×10^{-8} cm^2 s^{-1}, while h-WO_3 supports K^+ transport with a lower barrier of 0.11 eV and a higher coefficient 2.12×10^{-5} cm^2 s^{-1}.[227] Alkali-metal insertion induces n-type conductivity, small polaron formation, and tunable visible-NIR absorption, making WO_3 promising for iontronic and chromogenic devices. Damien Hanlon *et al.*[8] revealed that the photoluminescence of exfoliated MoO_3 was different, indicating a decoupling of the monolayers during exfoliation. Due to the poor electrical conductivity of MoO_3, they created supercapacitor electrodes using liquid-exfoliated MoO_3. These electrodes had a comparatively low capacitance of 2 F g^{-1} at 10 mV. Beyond the percolation threshold, the addition of CNT increased capacitance by 100 times, resulting in an extremely high capacitance of 540 F g^{-1} at just 0.1 mV.[8] Since waste heat may be transformed into electricity without harming the environment, efforts to find novel thermoelectric materials have redoubled in an effort to create effective TE power generators for the production of clean energy.[228] The applications of 2D LMOs for thermoelectric (TE) materials include four main areas: cooling, energy scavenging, sensing, and thermopower wave sources. Without lowering the Seebeck coefficient and electrical conductivity, it is possible to develop thermoelectric materials with an extremely low thermal conductivity.[5] For the figure of merit *ZT* to be competitive with alternative cooling or scavenging techniques, it should ideally be greater than 2. By enhancing phonon scattering directed along the planes, 2D structures may be able to lower the thermal conductivity of 2D LMOs relative to their bulk.[5]

A two-dimensional structure is composed of an extremely thin layer of material that is semi-infinitely large in one dimension and nanoscale thick in another. Since electron mobility may be limited parallel to the layers and phonons mostly scatter at interfaces, it is expected that 2D materials will lower the overall thermal conductivity of 2D LMOs when compared to their bulk counterparts.[229] In 2D systems, the thermal conductivity of electrons is mostly determined by the layer thickness. In contrast to phonons, electrons are limited to two-dimensional travel parallel to the layers due to quantum confinement, which has a substantial impact on their transport characteristics. Furthermore, by reducing scattering effects and

encouraging more effective charge carrier movement inside the restricted structure, greater confinement is anticipated to improve the electron thermal conductivity.[229] When Ba was incorporated into Sr_2TiCoO_6, electrical conductivity measurements revealed a semiconductor to metal transition, making this material a possible choice for high-temperature TE applications. In this multilayer material, the maximum TE figure of merit ZT was discovered to be 0.29 at 1223 K.[228] The parent compound of high-temperature superconductivity is La_2CuO_4, whose superconducting characteristics are intimately related to excess oxygen content and phase transition-induced structural alterations. This material's electrical and thermal transport behavior is greatly influenced by its basic layered structure, which is made up of 2D CuO_2 planes inside a unit cell. In addition to its superconducting qualities, $LaCuO_4$ and its doped forms have demonstrated potential for thermoelectric uses. Ceramics made from $La_{1.98}Y_{0.02}CuO_4$, for example, have an exceptionally high thermoelectric power factor (TPF) of 103 μW $m^{-1} K^{-2}$. Furthermore, this material has been reported to have a figure of merit (ZT) of 0.17 at 330 K, which is substantially greater than that of undoped La_2CuO_4 at the same temperature. These results imply that minor compositional changes might significantly improve thermoelectric performance, which makes materials based on La_2CuO_4 an appealing option for energy conversion applications.[230] Thus, the Fermi level in 2D systems depends strongly on morphology and temperature. This Fermi level can also be changed using a variety of doping techniques and methods, and as predicted, improved electrical
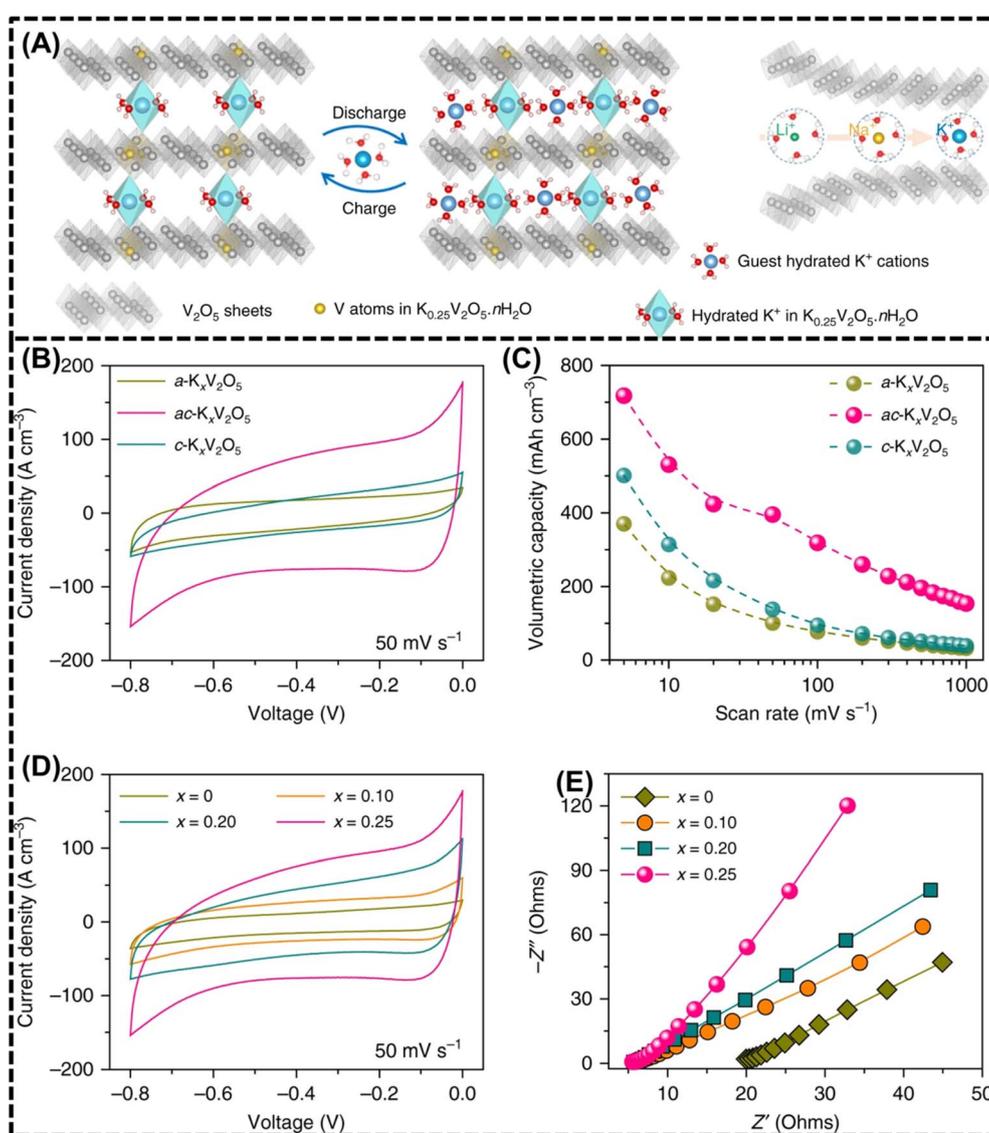

Fig. 13 (A) Schematic illustration of hydrated-ion storage in layered V_2O_5, showing limited intercalation in orthorhombic V_2O_5 with narrow interlayer spacing and enhanced ion accommodation. (B) Example CV curve for Au-supported nanopore microelectrodes that have been annealed at 25, 200, and 300 °C. (C) Volumetric capacities of nonporous $Au/K_xV_2O_5$ ($x = 0.25$) microelectrodes at different scan rates. (D) CV curves of nanoporous microelectrodes annealed at 200 °C with 0.5 M K_2SO_4 at a scan rate of 50 mV s^{-1}. (E) EIS spectra of nanoporous Au/ac-$K_xV_2O_5$ microelectrodes annealed at 200 °C ($x = 0$, 0.1, 0.2, and 0.25). Reprinted with permission from ref. 232 copyright of Nature 2019.

conductivities have been shown in a variety of 2D LMOs, including MoO_3, CoO_2, and ZnO structures.[229] Since the discovery of the excellent p-type material Na_xCoO_2, many cobaltites with hexagonal CoO_2 sheets that are structurally similar to those in $NaCoO_2$ have been prepared and studied from the TE point of view. It has also been shown that sheets of $Ca_3Co_4O_9$ and $Bi_2Sr_2Co_2O_9$ exhibit TE properties.[231] The hydrated ion storage methods in layered V_2O_5, especially in the $K_xV_2O_5$ system, are shown in Fig. 13(A). The $K_{0.25}V_2O_5 \cdot nH_2O$ molecular pillars, which anchor the V_2O_5 bilayers and affect ion intercalation behavior, are highlighted in the diagrams. Two structural configurations are shown: one with a high interlayer gap, in which the electrochemical performance is improved by the effective intercalation of hydrated Li^{2+}, Na^+, and K^+ cations supported by an enlarged structure, which, in turn, is supported by molecular pillars. As observed in the orthorhombic V_2O_5 phase, the second configuration has a short interlayer gap that limits charge storage capacity and ion mobility.[232] Fig. 13(B) presents the representative cyclic voltammetry (CV) curves for nanoporous Au-supported $K_xV_2O_5$ microelectrodes, annealed at different temperatures (25 °C, 200 °C, and 300 °C). The data presented in Fig. 13(C) and (D) offer important insights into the electrochemical performance of $Au/K_xV_2O_5$-based microelectrodes and the effects of structural phase and potassium content on their charge storage behavior. Fig. 13(C) shows the volumetric capacities of nonporous $Au/K_xV_2O_5$ ($x = 0.25$) microelectrodes across different structural phases: amorphous, partially crystalline, and crystalline, measured at various scan rates, revealing how annealing-induced phase changes influence storage capacity. Meanwhile, Fig. 13(D) displays cyclic voltammetry (CV) curves for nanoporous $Au/ac-K_xV_2O_5$ microelectrodes with different potassium contents ($x = 0$ to 0.25), all annealed at 200 °C and measured at a scan rate of 50 mV s^{-1} in a 0.5 M K_2SO_4 electrolyte. These CV curves further highlight the role of potassium doping in enhancing redox activity and charge storage, underscoring the combined impact of material composition and processing conditions on electrochemical performance. Fig. 13(E) displays the electrochemical impedance spectroscopy (EIS) spectra of the same microelectrodes, offering valuable information on their charge transfer resistance and ionic conductivity. This analysis helps in understanding the role of potassium doping in optimizing the electrochemical performance for energy storage applications. The fundamental concept behind hybrid crystals is that modules with distinct compositions, structural symmetries, and, therefore, distinct TE functions may be assembled to construct a complex crystal structure.[231] At the heterointerface between the oxygen-deficient $TiO_{2-\delta}$ and $SrTiO_3$ films, a large concentration of conduction electrons are localized within a unit cell thickness of $SrTiO_3$, which may remove O_2 from the $SrTiO_3$ substrate and inject conduction electrons. Thus, $SrTiO_3$ and TiO_2 are helpful for future titanate-based TE oxide design and selection.[231,233]

5.7 Spintronics

In spintronics, information is also transported by charge and is spun by free charge carriers. Spin-polarized transport can occur when there is an imbalance in the spin population at the Fermi level, as shown in 2D LMOs. The spin polarization-related energy shift between spin-up and spin-down states is the source of the magnetic moment.[5] Two-dimensional layered metal oxides (2D LMOs) are promising materials for spintronics, a relatively new field of electronics that makes use of electron spin, due to their distinctive electromagnetic properties. Due to the Rashba effect, these materials have strong spin–orbit coupling and consequently spin-polarized electronic states. Spin may be effectively managed and controlled. Effective spin realization and information processing are made possible by the spin Hall effect in 2D LMOs. Data storage, computation, and low-power electronics might all be revolutionized by spintronics based on 2D LMOs, which could spur more investigation into the creation of materials and spintronic devices such as magnetic sensors and spin valves. Spin FETs, MRAM, and spin torque oscillators are also included in this list. The spin-polarized carriers tunnel between the two electrodes of the magnetic material, which are separated by a very thin insulating barrier layer. There is no tunneling and the resistance of the device rises because the spin-up electrons can only tunnel into spin-up empty states when the magnetic moment is anti-parallel at both electrodes.[234] By adjusting the carrier density, the 2D systems open up the option of gating and so influencing both electrical and magnetic characteristics. In reality, gated magnetic semiconductor field effect heterostructures have previously shown that such a carrier density manipulation of magnetic semiconductor features is possible.[235–237] A scanning electron microscopy (SEM) picture of a typical device with a 500 nm scale bar is shown in Fig. 14(A). For clarity, the side borders of the IrO_2 wire are shown by the dotted lines. This picture offers a graphic depiction of the nanoscale device construction.[238] The experimental configuration for detecting nonlocal spin valve (NLSV) signals is shown in Fig. 14(B), where a magnetic field (H) is applied along the Py (pyrolytic iron) electrodes' easy axis. The NLSV signals for Py/Ag/Py lateral spin valves (LSVs) with and without an IrO_2 intermediate layer are compared at two distinct temperatures, 300 K and 10 K. The picture also shows the temperature dependency of the NLSV signals, which offers important information on how temperature and the IrO_2 interlayer affect the behavior of spin transport. This analysis aids in comprehending how material composition affects spintronic device performance optimization. Undoubtedly, the development of such 2D structures is essential for a number of upcoming spintronics applications. Whether the magnetic moments are parallel or antiparallel, they will affect the tunneling conductance between the Fe and Co electrodes at 4.2 K separated by an artificial Ge barrier.[239] Given the change in conductance, it is clear that this feature may be used in spintronic devices for quantum information technology. Due to its notable magnetoresistance at very low fields, magnetic tunnel junctions, which consist of two ferromagnetic electrodes separated by an insulating barrier, have garnered a lot of interest recently.[240] Using materials with a higher degree of spin polarization would surely increase the magnetoresistance. It is specifically expected that, at least at low temperatures, half metallic systems with a gap in one spin band
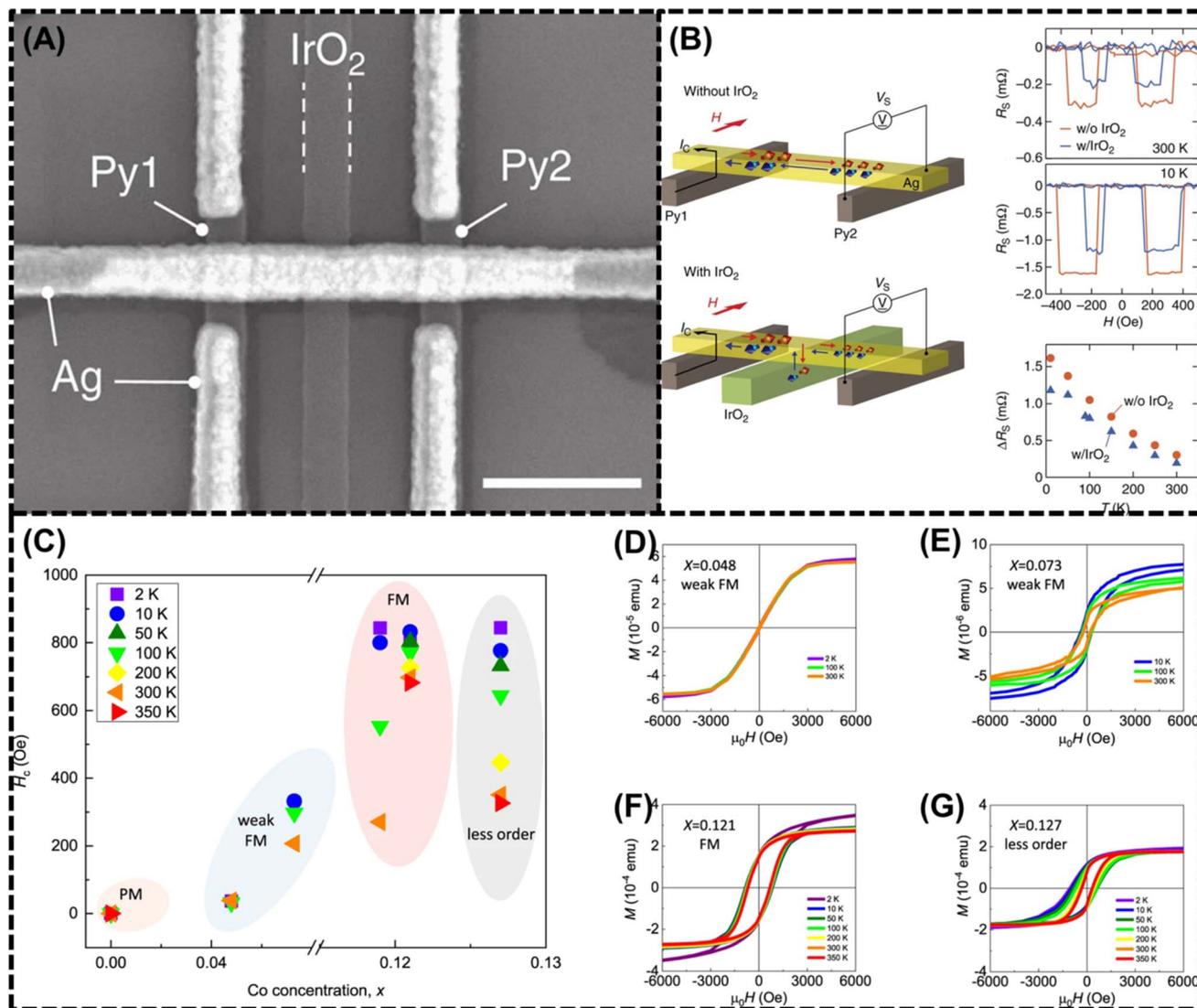
Fig. 14 (A) Scanning electron microscopic image of a typical device, in which the side margins of the IrO$_2$ wire are indicated by dotted lines for clarity, with a scale bar of 500 nm. (B) NLSV signals at 300 K and 10 K for Py/Ag/Py LSVs without and with the IrO$_2$ middlewire, together with the associated temperature dependency of the NLSV signals, displayed schematically in the measurement setup. The Py electrodes' easy axis is where the magnetic field H is applied. Reprinted with permission from ref. 238 copyright of Nature 2013. (C) Temperature and concentration-dependent coercive fields in gZCO obtained by SQUID shows that increased gZCO can be tuned from paramagnetic to ferromagnetic and to less ordered states. M–H curves of (D) Zn$_{0.952}$Co$_{0.048}$O/rGO, (E) Zn$_{0.927}$Co$_{0.073}$O/rGO, (F) Zn$_{0.879}$Co$_{0.121}$O/rGO, and (G) Zn$_{0.873}$Co$_{0.127}$O/rGO on the basis of SQUID measurements. Reprinted with permission from ref. 248 copyright of Nature 2021.

and the Fermi level but no gap in the other will have a spin-polarization value close to 100%.[240,241] Ma *et al.* shows that a 2D amorphous MoO$_{3-x}$/graphene oxide heterostructure exhibits room-temperature ferromagnetism with a Curie temperature > 350 K.[242] Interfacial oxygen migration and charge transfer modulate Mo d-electron states and oxygen vacancies, enhancing the ferromagnetic behavior. This study demonstrates atomic-scale control of magnetism in 2D amorphous oxides for spintronic applications. CVD-grown α-MoO$_3$ microflakes annealed in H$_2$ at 150–350 °C exhibit room-temperature ferromagnetism, with the 250 °C sample reaching 0.087 emu g^{-1} magnetization.[243] Oxygen vacancy concentration shows a one-to-one correlation with magnetic moment, as confirmed

by XPS, EPMA, and DFT calculations. Hydrogen incorporation and partial MoO$_2$ formation further modulate the ferromagnetic behavior, highlighting defect-driven magnetism in MoO$_3$. The Fe/Al$_2$O$_3$/Fe junction also has a strong magnetic tunneling effect, and Miyazaki and Tezuka found that it has a magnetoresistance ratio of 30% at 4.2 K and 18% at 300 K.[244] An inverse link between spin polarization and magnetic moment was discovered by the successful measurement of the spin polarization of electrodes tunneling through Fe, Co, Ni, and Gd films. These results imply that stronger spin polarization is typically found in materials with lower magnetic moments. Consequently, employing magnetic electrodes composed of materials with high magnetization is expected to enhance the formation

of magnetic tunneling junctions with a high magnetoresistance ratio. This insight is crucial for optimizing spintronic devices, where efficient spin transport and high magnetoresistance are key to improving performance.[245] Shivade *et al.* shows that nitrogen-doped WO_3 exhibits room-temperature d^0 ferromagnetism with a magnetic moment of 1.0 μB per N defect.[246] Ferromagnetism arises from spin polarization of N 2p and neighboring O 2p orbitals and persists at room temperature with structural stability. DFT and HSE06 calculations confirm that N-doped WO_3 is a promising candidate for spintronic applications. Zhang *et al.* found in his research that oxygen-vacancy-engineered monoclinic WO_3 exhibits enhanced intrinsic spin Hall conductivity up to ~10 and spin Hall angle (SHA) up to 72.6% at low vacancy concentrations.[247] Vacancies raise the Fermi level into the conduction band, boosting charge-to-spin conversion efficiency while maintaining room-temperature structural stability. This demonstrates WO_3 as a promising spintronic material where defect engineering simultaneously enhances charge conductivity and spin current.

Electron spectroscopy at room temperature with spin and angle resolved was used to study the spin-dependent electronic structure of thin epitaxial magnetite films of various crystallographic orientations. Fe_3O_4 (111) films were discovered to exhibit a maximum spin polarization value of more than −80% close to the Fermi energy, which is consistent with the spin-split band structure.[249] In a half metallic CrO_2-based epitaxial film with a Co counter electrode and tunneling barrier, the resistance of the junction is larger when the electrodes are aligned parallel to one another than when they are aligned perpendicularly. In contrast to when they are positioned perpendicularly, the electrodes are orientated parallel to each other. The coercivities of the two magnetic layers are correlated with the changes in junction resistance with applied field, with a maximum recorded magnetoresistance of 8% at 4.2 K and a negative sign.[240] Jo *et al.*[250] manufactured spin-polarized tunneling devices based on $La_{0.7}Ca_{0.3}MnO_3$ half-metallic magnetites with $NdGaO_3$ as a barrier material. Compared to the value that was directly observed at 4.2 K, the electron polarization derived from the observations at 77 K is greater. $La_{0.7}Ca_{0.3}MnO_3$ thin films and multilayers on $SrTiO_3$ show that these layers contain highly ordered areas, but these regions must also be electrically discontinuous. Since substantial tunneling may only occur between metallic magnetically ordered sections at a tunnel junction, the size and distribution of the ferromagnetic regions will have a considerable impact on the overall tunnel current.[250,251] Fig. 14(C) presents the temperature and Co-concentration-dependent coercive fields in gZCO obtained by SQUID (Superconducting Quantum Interference Device) measurements.[248] The plot demonstrates that gZCO can be tuned from paramagnetic to ferromagnetic and to less ordered states, showcasing the tunability of the magnetic properties. Based on SQUID measurements, Fig. 14(D)–(G) display magnetization against applied magnetic field (M–H) curves for various Zn–Co–O/rGO (reduced graphene oxide) composite compositions. The curves are presented for different Co concentrations (from 4.8% to 12.7%). These curves provide valuable insights into the magnetic behavior of Zn–Co–O/rGO

composites with different compositions. Additionally, another ferromagnetic device, composed of a $CoFe/Al_2O_3/Co$ junction, exhibits fractional changes in resistance under a magnetic field at different temperatures showing increases of 11.8% at 295 K, 20% at 77 K, and 24% at 4.2 K. These findings are consistent with Jullière's concept, which uses the spin polarization of conduction electrons in magnetic films to explain magnetoresistance. The model's dependability in describing the spin-dependent transport characteristics of the junction is confirmed by the consistency with Jullière's predictions at 4.2 K.[239,252] Two-dimensional DMS structures like quantum wells, multilayers, and superlattices are likely to be used in many of the anticipated applications of diluted magnetic semiconductor (DMS) systems, which combine the benefits of ferromagnetic materials and semiconductors with the added flexibility of carrier-mediated ferromagnetism, which allows the tuning of the magnetic properties by applying external gate voltages or optical pulses to control the carrier density,[237,253,254] because 3D systems, which have mostly been studied theoretically in the DMS literature, are expected to have very different magnetic properties than 2D systems.[237,253,254]

5.8 Gas sensing and biosensing

Instead of using the typical metal oxides for gas sensing, 2D LMOs rely on charge transfer processes, where the sensing materials act as either donors or acceptors of charges.[255] Gas sensing and biosensing are two significant applications where 2D LMOs exhibit tremendous promise.[256] These materials have the special ability to detect gases and biomolecules with extreme sensitivity and precision. Two-dimensional LMO gas sensors provide a high sensitivity and selectivity for gas detection. These alterations may be measured and are dependent on the goal gas volume. Effective gas sensing is made possible by the vast surface area and customizable electrical characteristics of 2D LMOs, which leads to effective gas absorption.[257] Environmental monitoring, workplace safety, and toxic or hazardous gas detection screening are some potential uses for 2D LMO-based gas sensors. Due to their high surface-to-volume ratio and surface functionalization, 2D LMOs are ideal for biosensing applications.[258] DNA, proteins, enzymes, and other biomolecules may all be detected using 2D LMO-based biosensors.[259] These biomolecules enable sensitive and precise detection of target biomolecules by inducing changes in the electric, optical, or electrochemical properties when bonded to a 2D LMO. Because of their precise detection accuracy, 2D LMOs are potential candidates for radiation sensing and biosensing applications that enhance environmental monitoring, healthcare, and protection technologies. A charge transfer process occurs between the adsorbed gases and the sensing materials when different gases are exposed. This reaction is followed by various charge transfer directions and amounts, which causes various variations in the material resistance.[255] The majority of semiconductor oxide sensors rely on the phenomena of a change in conductivity or electrical resistance of the material as a result of a contact between the material and the target gas for gas sensing.[260] When 2D materials are exposed to air, oxygen is chemisorbed onto their surfaces, where it interacts with the extra
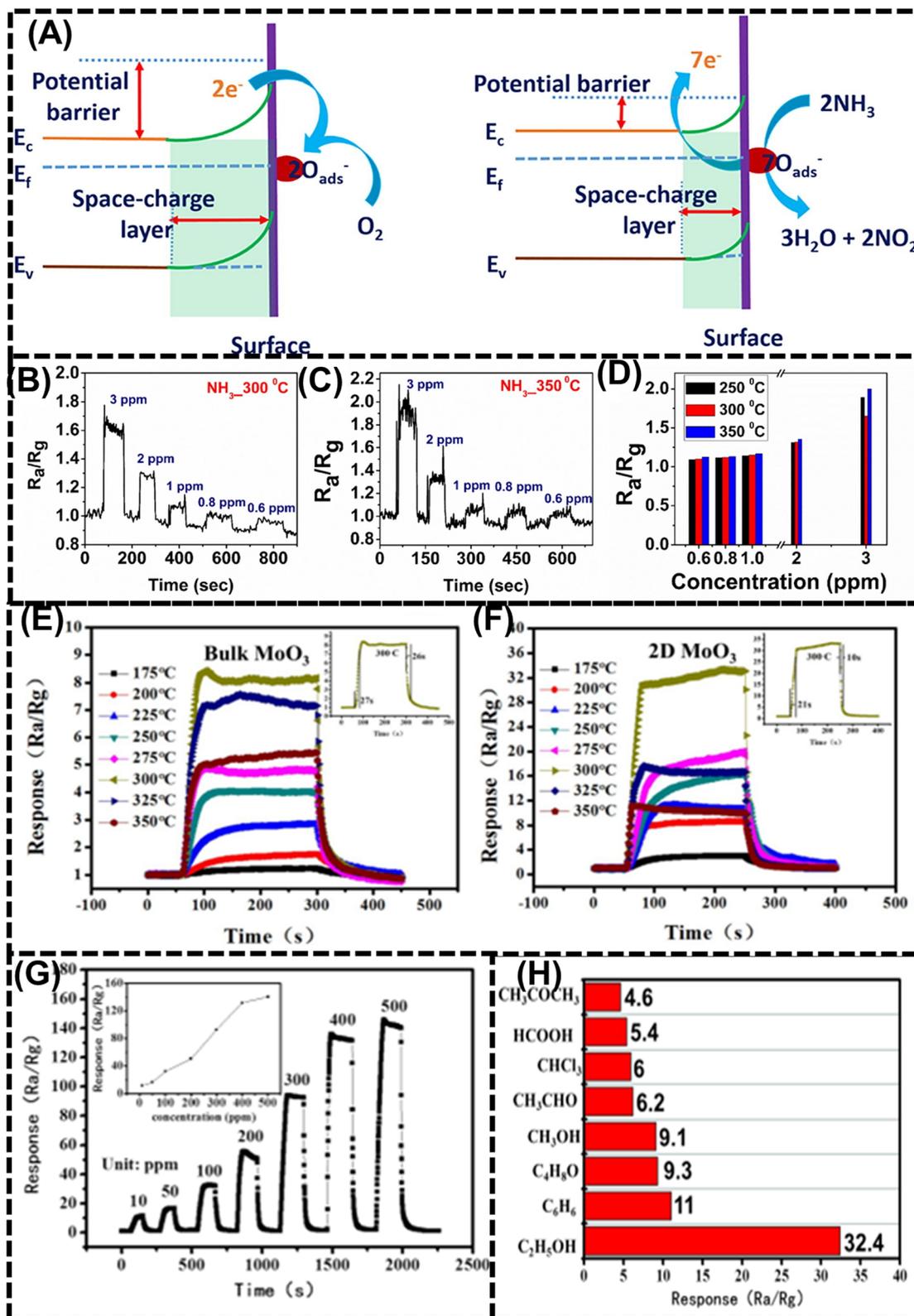
Fig. 15 (A) Principle of gas sensing with ZnO nanoflakes in ambient air and in an NH_3 environment. (B and C) Dynamic sensing characteristics of the 2D ZnO sensor at 300 °C and at 350 °C. (D) Comparison of sensor responses with temperatures. Reprinted with permission from ref. 263 copyright of Elsevier B.V. 2020. The results of sensor response using MoO_3 towards 100 ppm alcohol vapor at different operating temperatures for (E) bulk MoO_3 and (F) 2D MoO_3. (G) Sensor response at different concentrations. (H) Selectivity studies for the 2D MoO_3 sensor. Reprinted with permission from ref. 158 copyright of the Royal Society of Chemistry 2016.

electrons to produce oxygen species (O^{2-}, O^-, and O^{2-}). On the surface of 2D WO_3 nanoplates, a space charge layer develops, causing the carrier concentration to drop.[260] As the heat of oxide production per gram of oxygen atoms increased, adsorbed oxygen tended to decrease ($-\Delta H_f$).[261] The poor stability (low $-\Delta H_f$) of multivalent transition metal oxides can promote oxygen adsorption in the materials. In light of the limited stability of oxides linked to redox processes facilitated by fluctuating oxidation states, it is possible to understand the significant quantity of oxygen adsorbed in p-type transition metal oxides.[261] DFT analysis carried out by Huan et al. reveals that introducing oxygen vacancies in monolayer α-MoO_3 creates a defect state 0.59 eV below the CBM, lowers the work function, and enhances H_2O adsorption energy to −0.75 eV about 2.5 times stronger than on a perfect site.[262] These vacancies induce in-gap states, broaden NIR absorption, and enable efficient moisture sensing and optoelectronic applications. Since most 2D LMOs are multivalent, they can be used in technologies based on metal oxides to replace them as superior sensing elements.

Fig. 15(A) illustrates the principle of gas sensing with ZnO nanoflakes, both in ambient air and in an NH_3 environment.[263] Fig. 15(B) and (C) display the dynamic sensing characteristics of a 2D ZnO sensor at two different temperatures, 300 °C and 350 °C. These graphs show how the sensor response changes over time at different operating temperatures. Fig. 15(D) compares the sensor responses with temperatures. This plot provides a direct comparison of how the sensor response varies at different temperatures, offering insights into the temperature dependence of the ZnO sensor. Few inorganic graphene equivalents exist; among these, 2D oxides like TiO_2, MoO_3, and WO_3 are among the most researched for their stability in air at high temperatures.[2] They are ideal candidates for chemical sensors for volatile organic compounds (VOCs) because they are potent adsorbents to organic molecules and have a tendency to become oxygen-deficient at high temperatures due to partial oxygen loss.[158] MoO_3, a broad bandgap semiconductor with a 2D layered structure and a strong sensor response to different VOCs, is a model oxide in this category. Furthermore, it is demonstrated that 2D MoO_3 nanosheets outperform bulk MoO_3 powder in applications requiring chemical sensors. In comparison to the sensor used with bulk MoO_3, the sensor's reactivity to ethanol increases from 7 to 33.[2,158] To allow the efficient and logical construction of nanostructures using nanosheets, it is essential to develop a library of nanosheets with a range of compositions, topologies, and properties. For example, nanosheets with holes may result in new functionalities and advantages as it is projected that such a nanomesh structure will let the passage of small molecules or ions across the sheet. Superior H_2S sensing characteristics, such as increased sensor responsiveness, enhanced selectivity, and long-term stability, were demonstrated using the net-like 2D SnO_2/ZnO heterostructure. At a working temperature of just 100 °C, the SnO_2/ZnO-based H_2S sensor can also detect 10 parts per billion of gas.[264] The necessary pure or mixed nanostructured WO_3 polymorphs, such as monoclinic, triclinic, hexagonal, or orthorhombic, may be obtained by annealing WO_3 sheets. These polymorphs can then be utilized straight away as hydrated WO_3. This gives some latitude in altering the physical and chemical properties of the treated material.

Breedon et al. shows how to utilize this material to create an inexpensive NO_2 gas sensor that can detect NO_2 concentrations below ppb at a low operating temperature of 175 °C.[265]

One of the 2D LMOs with intriguing electrical, optical, and magnetic characteristics associated with this 2D layered structure is MoO_3, which can be produced into atomically thin layers.[266] In order to create field effect transistors with big grains, this 2D MoO_3 exhibits exceptional ion intercalation capabilities, and its high permittivity property can mitigate the effects of coulomb scattering on free charge carriers.[266] Shendage et al. constructed NO_2 gas sensor which shows the sensor response of 10 at 5 ppm.[260] Without the need of a seed layer, WO_3 may be directly grown on glass via a hydrothermal procedure and these WO_3 nanoplates show a promising potential for the development of low-consumption gas sensors. Using a solvothermal approach, Liu et al. created ultrathin 2D ZnO nanosheets that were just a few nanometers thick after coating them with CuO using pulsed laser ablation.[267] At a working temperature of 320 °C, an outstanding response of 97 was observed for 200 ppm of ethanol. ZnO nanosheets coated with CuO nanoparticles provide improved ethanol detection because of the creation of p–n junctions, which raise the density of active sites for ethanol adsorption. This sensing device also shows a two-fold increased responsiveness to ethanol vapour.[267] Fig. 15(E)–(G) show the results of sensor response using MoO_3 towards 100 ppm alcohol vapor at different operating temperatures for bulk MoO_3 (Fig. 15(E)) and 2D MoO_3 (Fig. 15(F)).[158] Additionally, Fig. 15(G) presents a sensor response at different concentrations.[158] These results provide information on the sensitivity of both bulk and 2D MoO_3 sensors to alcohol vapor at different concentrations and temperatures. Fig. 15(H) shows the selectivity studies for the 2D MoO_3 sensor. This part of the figure explores the ability of the 2D MoO_3 sensor to selectively respond to a particular gas (alcohol vapor) in the presence of other potentially interfering gases.

5.9 AI-enabled discovery of high-performance 2D LMOs

Artificial intelligence (AI) and machine learning (ML) are transforming the discovery of novel 2D LMOs with targeted optical, electronic, and catalytic properties.[268,269] Traditional trial-and-error synthesis and density functional theory (DFT) calculations are impeded by computational cost and vast compositional spaces.[270] AI-enabled frameworks enable high-throughput screening and prediction by learning from existing materials databases such as Materials Project, AFLOW, and JARVIS.[28,271–273] ML models trained from band structures computed with DFT have been shown to reproduce the band gap of complicated oxides to within a mean absolute error (MAE) of 0.25–0.35 eV with a speed-up in computational time by nearly 80–90% compared to full DFT workflows.[274,275] Using these tools, researchers have found promising 2D LMOs such as TiO_2, MoO_3, and V_2O_5 nanosheets, whose calculated electronic band gaps (≈ 3.0, 2.8, and 2.4 eV, respectively) agree with experimentally reported values for optoelectronic and photocatalytic applications.[276,277]

AI-powered generative models (like variational autoencoders and graph neural networks) can automatically design LMOs with target properties.[278,279] For example, a graph convolutional

neural network (GCNN) model was used to screen hypothetical oxide compounds, and identified stable layered oxides for visible-light harvesting.[280,281] Reinforcement learning approaches have also been used to optimize structural motifs for enhanced phonon–polariton coupling in materials like α-MoO_3 and Ti_2O_5, predicting light–matter confinement (up to λ/100) larger than in conventionally designed systems.[282,283] Beyond electronic structure prediction, AI can even guide synthesis conditions.[284] Bayesian optimization protocols have been demonstrated to identify the optimal sputtering power, annealing temperature, and oxygen partial pressure to synthesize phase-pure nanosheets with desired crystallinity.[285] Similarly, deep learning-assisted spectroscopy (DLS) was used to extract local defect chemistry 2D LMO thin films, correlating optical responses with defect density variations.[286]

Further, explainable AI techniques can reveal structure–property relationships that lie beyond human intuition.[287] Feature-importance mapping indicated that metal–oxygen coordination number, electronegativity difference and interlayer spacing are the most predictive parameters of dielectric permittivity and exciton binding energy within LMOs.[288] Guided by these correlations, AI-assisted inverse design platforms can now propose new 2D oxides with computed exciton binding energies and optical absorption edges, suitable for electronic devices.[289] AI-accelerated materials discovery revolutionizes the discovery and optimization of 2D LMOs by integrating data-driven prediction, automated synthesis, and characterization. The interaction between AI prediction, high-throughput computation, and experimental validation can collapse discovery timelines from years to months and enable faster development of high-performance 2D oxide materials for next-generation optoelectronics, sensors, and energy technologies.

5.10 Other applications

Two-dimensional metal oxides have potential uses beyond electronics and sensors in a wide range of industries. Due to its large surface area and capacity to store and release charge, 2D metal oxides such as TiO_2, MoO_3, and MnO_2 have demonstrated potential for application in energy storage systems such as batteries and supercapacitors. Due to their large surface area and distinctive chemical characteristics, metal oxide nanosheets can be utilized as effective catalysts for a range of chemical processes. Metal oxide nanosheets have demonstrated potential for application in water treatment technologies and can be employed as effective adsorbents to remove pollutants from water. Due to their biocompatibility and distinctive electrical and optical characteristics, metal oxide nanosheets have demonstrated potential for application in drug delivery, biosensing, and imaging. To make thin films and coatings for a range of uses, such as corrosion prevention, optical coatings, and electronic devices, metal oxide nanosheets can be employed.

6. Conclusions

Two-dimensional LMOs hold substantial potential for next-generation electronic, optoelectronic, and spintronic devices due to their tunable electrical and optical properties, high surface area, and mechanical flexibility. However, realizing this potential requires addressing several critical challenges. First, scalable synthesis methods must be developed to produce high-quality, defect-controlled 2D LMOs reproducibly. Second, the integration of 2D LMOs with other functional materials and device architectures demands careful control of interfacial chemistry, charge transport, and lattice compatibility. Third, the environmental and thermal stability of 2D LMOs under operational conditions remains underexplored and must be systematically evaluated. Future research should adopt a multi-faceted strategy: leveraging advanced synthesis approaches such as exfoliation, chemical vapor deposition, and template-assisted growth to tailor morphology and defect density; employing state-of-the-art characterization techniques to elucidate electronic, magnetic, and interfacial phenomena at the atomic scale; and combining computational modeling with experimental validation to guide rational material design. Additionally, electronic tuning strategies including doping, defect engineering, and heterostructure formation should be optimized to achieve targeted device functionalities. By following this roadmap, the field can move beyond proof-of-concept demonstrations toward the practical deployment of 2D LMOs in high-performance, scalable electronic systems, unlocking their full technological potential.

Conflicts of interest

The authors declare that they have no known competing financial interests or personal relationships that could have appeared to influence the work reported in this paper.

Data availability

No new data have been generated in this review.

References

1 G. S. Parkinson, *Nat. Mater.*, 2021, **20**, 1041–1042.
2 S. Z. Butler, S. M. Hollen, L. Cao, Y. Cui, J. A. Gupta, H. R. Gutiérrez, T. F. Heinz, S. S. Hong, J. Huang and A. F. Ismach, *ACS Nano*, 2013, **7**, 2898–2926.
3 D. Jung, L. M. A. Saleh, Z. J. Berkson, M. F. El-Kady, J. Y. Hwang, N. Mohamed, A. I. Wixtrom, E. Titarenko, Y. Shao, K. McCarthy, J. Guo, I. B. Martini, S. Kraemer, E. C. Wegener, P. Saint-Cricq, B. Ruehle, R. R. Langeslay, M. Delferro, J. L. Brosmer, C. H. Hendon, M. Gallagher-Jones, J. Rodriguez, K. W. Chapman, J. T. Miller, X. Duan, R. B. Kaner, J. I. Zink, B. F. Chmelka and A. M. Spokoyny, *Nat. Mater.*, 2018, **17**, 341–348.
4 Y. Ma, M. Wang and T. Zhai, *Adv. Mater.*, 2025, 2416160.
5 K. Kalantar-zadeh, J. Z. Ou, T. Daeneke, A. Mitchell, T. Sasaki and M. S. Fuhrer, *Appl. Mater. Today*, 2016, **5**, 73–89.
6 T. Yang, T. T. Song, M. Callsen, J. Zhou, J. W. Chai, Y. P. Feng, S. J. Wang and M. Yang, *Adv. Mater. Interfaces*, 2019, **6**, 1801160.

7 Q.-H. Wu, A. Fortunelli and G. Granozzi, *Int. Rev. Phys. Chem.*, 2009, **28**, 517–576.

8 D. Hanlon, C. Backes, T. M. Higgins, M. Hughes, A. O'Neill, P. King, N. McEvoy, G. S. Duesberg, B. Mendoza Sanchez and H. Pettersson, *Chem. Mater.*, 2014, **26**, 1751–1763.

9 W. F. Jaynes, Characterization and separation of soil clay minerals using ion exchange, lithium charge reduction, and density gradient techniques, PhD Thesis, The Ohio State University, 1988.

10 R. Ma and T. Sasaki, *Adv. Mater.*, 2010, **22**, 5082–5104.

11 A. Grandin, M. Borel and B. Raveau, *J. Solid State Chem.*, 1985, **60**, 366–375.

12 L. Li, R. Ma, Y. Ebina, K. Fukuda, K. Takada and T. Sasaki, *J. Am. Chem. Soc.*, 2007, **129**, 8000–8007.

13 H. T. Tan, W. Sun, L. Wang and Q. Yan, *ChemNanoMat*, 2016, **2**, 562–577.

14 A. P. Dral and E. Johan, *Sens. Actuators, B*, 2018, **272**, 369–392.

15 H. Xie, Z. Li, L. Cheng, A. A. Haidry, J. Tao, Y. Xu, K. Xu and J. Z. Ou, *Iscience*, 2021, **25**, 103598.

16 Z. Yin, X. Zhang, Y. Cai, J. Chen, J. I. Wong, Y. Y. Tay, J. Chai, J. Wu, Z. Zeng and B. Zheng, *Angew. Chem., Int. Ed.*, 2014, **53**, 12560–12565.

17 H. Liu, Y. Cai, M. Han, S. Guo, M. Lin, M. Zhao, Y. Zhang and D. Chi, *Nano Res.*, 2018, **11**, 1193–1203.

18 Y. Song, B. Xu, T. Liao, J. Guo, Y. Wu and Z. Sun, *Small*, 2021, **17**, 2002240.

19 L. P. Moraes, J. Mei, F. C. Fonseca and Z. Sun, in *2D Nanomaterials for Energy Applications*, Elsevier, 2020, pp. 39–72.

20 M.-Q. Zhao, M. Torelli, C. E. Ren, M. Ghidiu, Z. Ling, B. Anasori, M. W. Barsoum and Y. Gogotsi, *Nano Energy*, 2016, **30**, 603–613.

21 Y. Sun, R. Wang and K. Liu, *Appl. Phys. Rev.*, 2017, **4**, 011301.

22 T. F. Schranghamer, M. Sharma, R. Singh and S. Das, *Chem. Soc. Rev.*, 2021, **50**, 11032–11054.

23 K. Liao, X. Wang, Y. Sun, D. Tang, M. Han, P. He, X. Jiang, T. Zhang and H. Zhou, *Energy Environ. Sci.*, 2015, **8**, 1992–1997.

24 H. Tan, E. Ye and W. Y. Fan, *Adv. Mater.*, 2006, **18**, 619–623.

25 G. B. Saupe, C. C. Waraksa, H.-N. Kim, Y. J. Han, D. M. Kaschak, D. M. Skinner and T. E. Mallouk, *Chem. Mater.*, 2000, **12**, 1556–1562.

26 C. Zhao, H. Zhang, W. Si and H. Wu, *Nat. Commun.*, 2016, **7**, 12543.

27 A. Jain, S. P. Ong, G. Hautier, W. Chen, W. D. Richards, S. Dacek, S. Cholia, D. Gunter, D. Skinner and G. Ceder, *APL Mater.*, 2013, **1**, 011002.

28 M. K. Horton, P. Huck, R. X. Yang, J. M. Munro, S. Dwaraknath, A. M. Ganose, R. S. Kingsbury, M. Wen, J. X. Shen, T. S. Mathis, A. D. Kaplan, K. Berket, J. Riebesell, J. George, A. S. Rosen, E. W. C. Spotte-Smith, M. J. McDermott, O. A. Cohen, A. Dunn, M. C. Kuner, G.-M. Rignanese, G. Petretto, D. Waroquiers, S. M. Griffin, J. B. Neaton, D. C. Chrzan, M. Asta, G. Hautier, S. Cholia, G. Ceder, S. P. Ong, A. Jain and K. A. Persson, *Nat. Mater.*, 2025, **24**, 1522–1532.

29 L. Peng, P. Xiong, L. Ma, Y. Yuan, Y. Zhu, D. Chen, X. Luo, J. Lu, K. Amine and G. Yu, *Nat. Commun.*, 2017, **8**, 15139.

30 R. Kim, J.-S. Jang, D.-H. Kim, J.-Y. Kang, H.-J. Cho, Y. J. Jeong and I.-D. Kim, *Adv. Funct. Mater.*, 2019, **29**, 1903128.

31 N. Kamarulzaman, N. Chayed, N. Badar, M. Kasim, D. Mustaffa, K. Elong, R. Rusdi, T. Oikawa and H. Furukawa, *ECS J. Solid State Sci. Technol.*, 2016, **5**, Q3038.

32 J. Y. Lim, J. S. Oh, B. D. Ko, J. Won Cho, S. O. Kang, G. Cho, H. S. Uhm and E. H. Choi, *J. Appl. Phys.*, 2003, **94**, 764–769.

33 V. Van On, J. Guerrero-Sanchez, R. Ponce-Pérez, T. V. Vu, J. F. Rivas-Silva, G. H. Cocoletzi and D. M. Hoat, *Mater. Sci. Semicond. Process.*, 2022, **149**, 106876.

34 N. Kamarulzaman, N. F. Chayed, N. Badar, M. F. Kasim, D. T. Mustaffa, K. Elong, R. Rusdi, T. Oikawa and H. Furukawa, *ECS J. Solid State Sci. Technol.*, 2016, **5**, Q3038.

35 C. Tang, B. Q. Li, Q. Zhang, L. Zhu, H. F. Wang, J. L. Shi and F. Wei, *Adv. Funct. Mater.*, 2016, **26**, 577–585.

36 M. A. Bolorizadeh, V. A. Sashin, A. S. Kheifets and M. J. J. Ford, *J. Electron Spectrosc. Relat. Phenom.*, 2004, **141**, 27–38.

37 D. M. Hoat, M. Naseri, J. F. Rivas-Silva and G. H. Cocoletzi, *Optik*, 2020, **218**, 165115.

38 L. Sheng, T. Liao, L. Kou and Z. Sun, *Mater. Today Energy*, 2017, **3**, 32–39.

39 S. Kashiwaya, J. Morasch, V. Streibel, T. Toupance, W. Jaegermann and A. Klein, *Surf. Interfaces*, 2018, **1**, 73–89.

40 Z. Xiong, P. Zhang, W. Kang and W. Fang, *Acta. Phys. Sin.*, 2020, **69**, 166301.

41 T. Liu, J. Liu, Y. Yang, X. Wang, T. Zhou, G. Yin, F. Jia and B. Liu, *Surf. Interfaces*, 2023, **38**, 102847.

42 S. Sovizi, S. Tosoni, T. Zdunek and R. Szoszkiewicz, *Appl. Surf. Sci.*, 2024, **669**, 160578.

43 A. Arash, T. Ahmed, A. G. Rajan, S. Walia, F. Rahman, A. Mazumder, R. Ramanathan, S. Sriram, M. Bhaskaran and E. Mayes, *2D Materials*, 2019, **6**, 035031.

44 D. A. Kowalczyk, M. Rogala, K. Szałowski, D. Belic, P. Dąbrowski, P. Krukowski, I. Lutsyk, M. Piskorski, A. Nadolska and P. Krempinski, *ACS Appl. Mater. Interfaces*, 2022, **14**, 44506–44515.

45 Y. Gao, Q. Sun, J. M. Yu, M. Motta, J. McClain, A. F. White, A. J. Minnich and G. K.-L. Chan, *Phys. Rev. B*, 2020, **101**, 165138.

46 F. Shayeganfar, K. S. Vasu, R. R. Nair, F. M. Peeters and M. Neek-Amal, *Phys. Rev. B*, 2017, **95**, 144109.

47 Y. Zheng, Y. Li, R. Huang, Y. Huang, J. Yao, B. Huang and A. A. Dubale, *ACS Appl. Energy Mater.*, 2019, **2**, 8262–8273.

48 M. T. Greiner, M. G. Helander, Z.-B. Wang, W.-M. Tang and Z.-H. Lu, *J. Phys. Chem. C*, 2010, **114**, 19777–19781.

49 M. V. Kumar, S. Muthulakshmi, A. A. Paulfrit, J. Pandiarajan, N. Jeyakumaran and N. Prithivikumaran, *Int. J. ChemTech Res.*, 2014, **6**, 5174–5177.

50 S. Hietzschold, S. Hillebrandt, F. Ullrich, J. Bombsch, V. Rohnacher, S. Ma, W. Liu, A. Köhn, W. Jaegermann and A. Pucci, *ACS Appl. Mater. Interfaces*, 2017, **9**, 39821–39829.

51 Y. Omomo, T. Sasaki, L. Wang and M. Watanabe, *J. Am. Chem. Soc.*, 2003, **125**, 3568–3575.

52 C. S. Yang, D. S. Shang, N. Liu, G. Shi, X. Shen, R. C. Yu, Y. Q. Li and Y. Sun, *Adv. Mater.*, 2017, **29**, 1700906.

53 G. Zhao, J. Li, L. Jiang, H. Dong, X. Wang and W. Hu, *Chem. Sci.*, 2012, **3**, 433–437.

54 S. Balendhran, S. Walia, H. Nili, J. Z. Ou, S. Zhuiykov, R. B. Kaner, S. Sriram, M. Bhaskaran and K. Kalantar-zadeh, *Adv. Funct. Mater.*, 2013, **23**, 3952–3970.

55 F. Rahman, T. Ahmed, S. Walia, E. Mayes, S. Sriram, M. Bhaskaran and S. Balendhran, *2D Materials*, 2017, **4**, 035008.

56 K. Zhou, G. Shang, H. H. Hsu, S. T. Han, V. A. L. Roy and Y. Zhou, *Adv. Mater.*, 2023, **35**, 2207774.

57 J. Mei, T. Liao, L. Kou and Z. Sun, *Adv. Mater.*, 2017, **29**, 1700176.

58 P. He, H. Yu and H. Zhou, *J. Mater. Chem.*, 2012, **22**, 3680–3695.

59 X. Chen, Y. Zhou, Q. Liu, Z. Li, J. Liu and Z. Zou, *ACS Appl. Mater. Interfaces*, 2012, **4**, 3372–3377.

60 X. Rui, Z. Lu, H. Yu, D. Yang, H. H. Hng, T. M. Lim and Q. Yan, *Nanoscale*, 2013, **5**, 556–560.

61 A. Takagaki, D. Lu, J. N. Kondo, M. Hara, S. Hayashi and K. Domen, *Chem. Mater.*, 2005, **17**, 2487–2489.

62 K. Fukuda, I. Nakai, Y. Ebina, R. Ma and T. Sasaki, *Inorg. Chem.*, 2007, **46**, 4787–4789.

63 A. AlMutairi, A. Xhameni, X. Guo, I. Chircă, V. Nicolosi, S. Hofmann and A. Lombardo, *Adv. Mater. Interfaces*, 2025, **12**, 2400481.

64 Z. M. El-Bahy, N. AlMasoud, M. Ali, T. S. Alomar, A. A. Al-wallan and H. M. Tahir, *J. Alloys Compd.*, 2025, **1010**, 178091.

65 H. Yu, H. Zeng, Y. Zhang, Y. Liu, W. ShangGuan, X. Zhang, Z. Zhang and Y. Zhang, *Adv. Funct. Mater.*, 2025, **35**, 2412913.

66 S. Hadke, M.-A. Kang, V. K. Sangwan and M. C. Hersam, *Chem. Rev.*, 2025, **125**, 835–932.

67 Y. Fan, X. Liu, K. Li, X. Zhang, L. Xu and B. Li, *Sep. Purif. Technol.*, 2025, **354**, 128832.

68 A. J. Martinolich and J. R. Neilson, *Chem. Mater.*, 2017, **29**, 479–489.

69 T. H. Yang, Y. Shi, A. Janssen and Y. Xia, *Angew. Chem., Int. Ed.*, 2020, **59**, 15378–15401.

70 M. C. Sigallon, A. Baillard, V. Consonni, F. Aubrit, N. Potrzebowska, R. Grasset, M. Tabellout, N. Gogneau, E. Sarrey and J.-E. Wegrowe, *Nano Trends*, 2025, 100112.

71 A.-H. Lu and F. Schüth, *C. R. Chim.*, 2005, **8**, 609–620.

72 N. Gangwar, C. Gangwar and J. Sarkar, *Heliyon*, 2024, **10**, e36810.

73 S. A. Kurnosenko, I. A. Minich, O. I. Silyukov and I. A. Zvereva, *Nanomaterials*, 2023, **13**, 3052.

74 B. Y. Zhang, K. Xu, Q. Yao, A. Jannat, G. Ren, M. R. Field, X. Wen, C. Zhou, A. Zavabeti and J. Z. Ou, *Nat. Mater.*, 2021, **20**, 1073–1078.

75 B. A. Holler, K. Crowley, M. H. Berger and X. P. A. Gao, *Adv. Electron. Mater.*, 2020, **6**, 2000635.

76 A. J. Molina-Mendoza, J. L. Lado, J. O. Island, M. A. Niño, L. Aballe, M. Foerster, F. Y. Bruno, A. López-Moreno, L. Vaquero-Garzon and H. S. J. Van Der Zant, *Chem. Mater.*, 2016, **28**, 4042–4051.

77 S. Puebla, R. D'Agosta, G. Sanchez-Santolino, R. Frisenda, C. Munuera and A. Castellanos-Gomez, *npj 2D Mater. Appl.*, 2021, **5**, 37.

78 Z. Hai, M. K. Akbari, C. Xue, H. Xu, L. Hyde and S. Zhuiykov, *Appl. Surf. Sci.*, 2017, **405**, 169–177.

79 N. Mahmood, H. Khan, K. Tran, P. Kuppe, A. Zavabeti, P. Atkin, M. B. Ghasemian, J. Yang, C. Xu and S. A. Tawfik, *Mater. Today Energy*, 2021, **44**, 69–77.

80 T. Alkathiri, N. Dhar, A. Jannat, N. Syed, M. Mohiuddin, M. M. Alsaif, R. S. Datta, K. A. Messalea, B. Y. Zhang and M. W. Khan, *Chem. Commun.*, 2020, **56**, 4914–4917.

81 Y. Zhang, Q. He, H. Yang, Z. Li, H. Jiang, Y. Zhang, X. Luo and Y. Zheng, *Nano Lett.*, 2024, **24**, 6247–6254.

82 Y. Omomo, T. Sasaki, W. Wang and M. Watanabe, *J. Am. Chem. Soc.*, 2003, **125**, 3568–3575.

83 F. Wang, X. Yin and X. Wang, *Extreme Mechanics Letters*, 2016, **7**, 64–70.

84 K. Zhou, G. Shang, H. H. Hsu, S. T. Han, V. A. Roy and Y. Zhou, *Adv. Mater.*, 2023, **35**, 2207774.

85 J. Wan, S. D. Lacey, J. Dai, W. Bao, M. S. Fuhrer and L. Hu, *Chem. Soc. Rev.*, 2016, **45**, 6742–6765.

86 A. Pal, S. Zhang, T. Chavan, K. Agashiwala, C. H. Yeh, W. Cao and K. Banerjee, *Adv. Mater.*, 2023, **35**, 2109894.

87 S. Balendhran, J. Deng, J. Z. Ou, S. Walia, J. Scott, J. Tang, K. L. Wang, M. R. Field, S. Russo and S. Zhuiykov, *Adv. Mater.*, 2013, **25**, 109–114.

88 X. Bi, G. Du, D. Sun, M. Zhang, Y. Yu, Q. Su, S. Ding and B. Xu, *Appl. Surf. Sci.*, 2020, **511**, 145617.

89 A. Singh, S. K. Yadav, A. Verma, S. Sikarwar and B. C. Yadav, *ECS Adv.*, 2023, **2**, 016501.

90 A. Giri, G. Park and U. Jeong, *Chem. Rev.*, 2023, **123**, 3329–3442.

91 Y. Qian, Q. Ruan, M. Xue and L. Chen, *J. Energy Chem.*, 2023, **89**, 41–70.

92 J. Duan, G. Álvarez-Pérez, C. Lanza, K. Voronin, A. I. F. Tresguerres-Mata, N. Capote-Robayna, J. Álvarez-Cuervo, A. Tarazaga Martín-Luengo, J. Martín-Sánchez and V. S. Volkov, *Nat. Mater.*, 2023, **22**, 867–872.

93 M. S. Javed, A. Mateen, I. Hussain, S. Ali, S. Asim, A. Ahmad, E. tag Eldin, M. A. Bajaber, T. Najam and W. Han, *Chem. Eng. J.*, 2023, **452**, 139455.

94 C.-H. Oh, R. S. Babu, S.-I. Kim, D.-P. Lee, G. Sim, D.-H. Lee, Y. Je, K. C. Hwi, W. J. Jeong and G. H. Ryu, *Journal of Asian Ceramic Societies*, 2022, **10**, 722–730.

95 S. Karimzadeh, B. Safaei, C. Yuan and T.-C. Jen, *Electrochem. Energy Rev.*, 2023, **6**, 24.

96 Z. Bian, J. Miao, T. Zhang, H. Chen, Q. Zhu, J. Chai, F. Tian, S. Wu, Y. Xu and B. Yu, *Small*, 2023, 2206791.

97 M. Liu, Z. Yang, S. Sha, K. Tang, P. Wan, C. Kan, D. N. Shi and M. Jiang, *ACS Appl. Mater. Interfaces*, 2023, **15**, 54655–54666.

98 A. Verma, P. Chaudhary, R. K. Tripathi and B. C. Yadav, *Sustainable Energy Fuels*, 2021, **5**, 1394–1405.

99 C. Li, Z. Liu, W. Lü, X. R. Wang, A. Annadi, Z. Huang, S. Zeng, A. Ariando and T. Venkatesan, *Sci. Rep.*, 2015, **5**, 13314.

100 I. Y. Kim, Y. K. Jo, J. M. Lee, L. Wang and S.-J. Hwang, *J. Phys. Chem. Lett.*, 2014, **5**, 4149–4161.

101 N. Zhang, Y.-R. Ji, J.-C. Wang, P.-F. Wang, Y.-R. Zhu and T.-F. Yi, *J. Energy Chem.*, 2023, **82**, 423–463.

102 N. Joseph, H. Fei, C. Bubulinca, M. Jurca, M. Micusik, M. Omastova and P. Saha, *ACS Appl. Mater. Interfaces*, 2023, **15**, 54568–54581.

103 S. S. Hoseini, A. Seyedkanani, G. Najafi, A. P. Sasmito and A. Akbarzadeh, *Energy Storage Mater.*, 2023, **59**, 102768.

104 O. A. Kazi, W. Chen, J. G. Eatman, F. Gao, Y. Liu, Y. Wang, Z. Xia and S. B. Darling, *Adv. Mater.*, 2023, **35**, 2300913.

105 A. Zhang, R. Zhao, Y. Wang, J. Yang, C. Wu and Y. Bai, *Energy Environ. Sci.*, 2023, **16**, 3240–3301.

106 P. Wang, Y. Guo, J. Guan and Z. Wang, *Catalysts*, 2023, **13**, 189.

107 M. Yarar, A. Bouziani and D. Uner, *Catal. Commun.*, 2023, **174**, 106580.

108 X. Zhou, X. Zheng, B. Yan, T. Xu and Q. Xu, *Appl. Surf. Sci.*, 2017, **400**, 57–63.

109 G. Zhou, Z. Li, J. Dou, H. Ji, P. Kang, Y. Shen, S. Wang and X. Xu, *RSC Adv.*, 2023, **13**, 10254–10260.

110 S. Cianci, E. Blundo, M. Felici, A. Polimeni and G. Pettinari, *Opt. Mater.*, 2022, **125**, 112087.

111 S. S. Shinde, N. K. Wagh, S. H. Kim and J. H. Lee, *Adv. Sci.*, 2023, **10**, 2304235.

112 J. M. Kim, M. F. Haque, E. Y. Hsieh, S. M. Nahid, I. Zarin, K. Y. Jeong, J. P. So, H. G. Park and S. Nam, *Adv. Mater.*, 2023, **35**, 2107362.

113 A. Verma, P. Chaudhary, R. K. Tripathi and B. C. Yadav, *Sens. Actuators, A*, 2021, **321**, 112600.

114 Z.-H. Yan, Y. Zhang, H. Qiao, L. Duan and L. Ni, *Thin Solid Films*, 2023, **764**, 139626.

115 Z. Hou, C. Cui, Y. Li, Y. Gao, D. Zhu, Y. Gu, G. Pan, Y. Zhu and T. Zhang, *Adv. Mater.*, 2023, 2209876.

116 S. Cao, G. Liu, J. Huang, X. Yu, D. Fan, Y. Ni and Y. Luo, *J. Non-Cryst. Solids*, 2024, **624**, 122726.

117 S. A. Mahmoud, L. G. Amin, A. A. Akl and A. Dhahri, *Phys. B*, 2023, **668**, 415249.

118 K. K. Gleason, *Adv. Mater.*, 2023, 2306665.

119 R. Kumar, S. Sahoo, E. Joanni, R. Pandey and J.-J. Shim, *Chem. Commun.*, 2023, **59**, 6109–6127.

120 C. Liu, Y. Liu, R. Ma, T. Sasaki, X. Wang, P. Xiong and J. Zhu, *Mater. Chem. Front.*, 2023, **7**, 1004–1024.

121 Q. Song, S. Zhou, S. Wang, S. Li, L. Xu and J. Qiu, *Chem. Eng. J.*, 2023, **461**, 142033.

122 X. Hu, J. Fan, R. Wang, M. Li, S. Sun, C. Xu and F. Pan, *Green Energy Environ.*, 2023, **8**, 601–611.

123 H.-J. Liu, M. Ye, C.-Y. Yang, Y.-W. Fang, Y.-Y. Chin, C.-Y. Chen, R. T. Hung, Y. Zhu, L.-C. He, M.-Y. Huang, L. Chen, M. Gu, S. Ke, Y.-F. Liao, K.-D. Tsuei, H.-J. Lin, C.-T. Chen, S. Agrestini, J. Herrero-Martin and C.-H. Lai, *Appl. Mater. Today*, 2021, **24**, 101101.

124 F. Su, F. Xing, X. Wang, F. Liu, L. Zhang and Z.-S. Wu, *Energy Environ. Sci.*, 2023, **16**, 222–230.

125 A. Verma, U. Kumar, P. Chaudhary and B. C. Yadav, *Solid State Commun.*, 2022, **348**, 114723.

126 Y. Liang, H. Li, X. Zhao, L. Xue, L. Tang, F. Xue, T. Yu and Y. Yang, *J. Alloys Compd.*, 2023, **947**, 169503.

127 C.-Y. Zhao, S.-S. Li and Y. Yan, *Chin. Phys. B*, 2023, **32**, 087801.

128 E. Seven, D. Akay, S. B. Ocak and E. Ö. Orhan, *Mater. Sci. Semicond. Process.*, 2024, **169**, 107913.

129 F. Kiani, A. R. Bowman, M. Sabzehparvar, C. O. Karaman, R. Sundararaman and G. Tagliabue, *ACS Energy Lett.*, 2023, **8**, 4242–4250.

130 L. Zhang, R. Ni and Y. Zhou, *J. Appl. Phys.*, 2023, **133**, 080901.

131 M. Osada and T. Sasaki, *J. Mater. Chem.*, 2009, **19**, 2503–2511.

132 N. Sakai, Y. Ebina, K. Takada and T. Sasaki, *J. Phys. Chem. B*, 2005, **109**, 9651–9655.

133 D. W. Bahnemann, M. Hilgendorff and R. Memming, *J. Phys. Chem. B*, 1997, **101**, 4265–4275.

134 N. Sakai, Y. Ebina, K. Takada and T. Sasaki, *J. Am. Chem. Soc.*, 2004, **126**, 5851–5858.

135 M. I. F. Zainuddin, A. L. Ahmad and M. A. Adnan, *J. Chem. Technol. Biotechnol.*, 2025, 654–665.

136 J. Guo, Z. Lin, X. Che, C. Wang, T. Wan, J. Yan, Y. Zhu and Y. Chai, *ACS Nano*, 2025, **19**, 2848–2856.

137 X. Wang, D. Liu, X. Wang, Z. Liu and S. Luo, *Comput. Mater. Sci.*, 2025, **246**, 113346.

138 R. B. dos Santos, R. Rivelino, G. K. Gueorguiev and A. Kakanakova-Georgieva, *CrystEngComm*, 2021, **23**, 6661–6667.

139 D. Forrer and A. Vittadini, *Chem. Phys. Lett.*, 2011, **516**, 72–75.

140 Y. Zhang, H.-X. Chen, L. Duan and J.-B. Fan, *Thin Solid Films*, 2021, **721**, 138549.

141 Y. M. Jahn and A. J. N. Ya'Akobovitz, *Nanoscale*, 2021, **13**, 18458–18466.

142 S. Sucharitakul, G. Ye, W. R. L. Lambrecht, C. Bhandari, A. Gross, R. He, H. Poelman and X. P. A. Gao, *ACS Appl. Mater. Interfaces*, 2017, **9**, 23949–23956.

143 W. Zhang, P. Shen, L. Qian, Y. Wang, H. Arandiyan, H. Mahmoud, X. Liu, J. Wang, X. Wang and Y. Liu, *ACS Appl. Energy Mater.*, 2021, **4**, 4551–4560.

144 A. Majid, A. Jabeen, S. U.-D. Khan and Z. Almutairi, *Mater. Sci. Eng., B*, 2021, **272**, 115349.

145 M. Hasan, H. Q. Ta, S. Ullah, X. Yang, J. Luo, A. Bachmatiuk, T. Gemming, B. Trzebicka, A. Mahmood and M. Zeng, *Arabian J. Chem.*, 2023, **16**, 104973.

146 A. Azam, J. Kim, J. Park, T. G. Novak, A. P. Tiwari, S. H. Song, B. Kim and S. Jeon, *Nano Lett.*, 2018, **18**, 5646–5651.

147 B. Bai, J. Li and J. Hao, *Appl. Catal., B*, 2015, **164**, 241–250.

148 K. V. Larionov, D. G. Kvashnin and P. B. Sorokin, *J. Phys. Chem. C*, 2018, **122**, 17389–17394.

149 Y. Cai, J. Xu, Y. Guo and J. Liu, *ACS Catal.*, 2019, **9**, 2558–2567.

150 R. A. Patil, C.-P. Chang, R. S. Devan, Y. Liou and Y.-R. Ma, *ACS Appl. Mater. Interfaces*, 2016, **8**, 9872–9880.

151 M. S. Krishna, S. Singh, M. Batool, H. M. Fahmy, K. Seku, A. E. Shalan, S. Lanceros-Mendez and M. N. Zafar, *Mater. Adv.*, 2023, **4**, 320–354.

152 D. Hoat, M. Naseri, T. V. Vu, J. Rivas-Silva, N. N. Hieu and G. H. Cocoletzi, *Superlattices Microstruct.*, 2020, **145**, 106644.

153 M.-Y. Lee, F.-S. Yen and H.-I. Hsiang, *Nanomaterials*, 2022, **12**, 2955.

154 U. M. Graham, S. Sharma, M. K. Sunkara and B. H. Davis, *Adv. Funct. Mater.*, 2003, **13**, 576–581.

155 C. Büchner, Z.-J. Wang, K. M. Burson, M.-G. Willinger, M. Heyde, R. Schlögl and H.-J. Freund, *ACS Nano*, 2016, **10**, 7982–7989.

156 A. K. Singh, B. C. Revard, R. Ramanathan, M. Ashton, F. Tavazza and R. G. Hennig, *Phys. Rev. B*, 2017, **95**, 155426.

157 X. Hu, K. Liu, Y. Cai, S.-Q. Zang and T. Zhai, *Small Sci.*, 2022, **2**, 2200008.

158 F. Ji, X. Ren, X. Zheng, Y. Liu, L. Pang, J. Jiang and S. F. Liu, *Nanoscale*, 2016, **8**, 8696–8703.

159 M. Zeng, Y. Xiao, J. Liu, K. Yang and L. Fu, *Chem. Rev.*, 2018, **118**, 6236–6296.

160 C. Gautam, A. Verma, P. Chaudhary and B. C. Yadav, *Opt. Mater.*, 2022, **123**, 111860.

161 A. Singh, P. Chauhan, A. Verma and B. C. Yadav, *Sustainable Energy Fuels*, 2023, **7**, 131–143.

162 H. Liu, L. Duan, K. Xia, Y. Chen, Y. Li, S. Deng, J. Xu and Z. Hou, *Nanomaterials*, 2022, **12**, 3211.

163 H. Yu, Q. Liao, Z. Kang, Z. Wang, B. Liu, X. Zhang, J. Du, Y. Ou, M. Hong and J. Xiao, *Small*, 2020, **16**, 2005520.

164 W. Feng, X. Wang, J. Zhang, L. Wang, W. Zheng, P. Hu, W. Cao and B. Yang, *J. Mater. Chem. C*, 2014, **2**, 3254–3259.

165 D. Xiang, C. Han, J. Zhang and W. Chen, *Sci. Rep.*, 2014, **4**, 4891.

166 C. Yin, C. Gong, J. Chu, X. Wang, C. Yan, S. Qian, Y. Wang, G. Rao, H. Wang and Y. Liu, *Adv. Mater.*, 2020, **32**, 2002237.

167 Q. Chen, Y. Zhang, T. Zheng, Z. Liu, L. Wu, Z. Wang and J. Li, *Nanoscale Adv.*, 2020, **2**, 2705–2712.

168 M. Myvizhia, K. S. Kumarb, P. Kavithac and P. Selvakumard, *J. Ovonic Res.*, 2023, **19**, 265–273.

169 H. S. Patel, V. A. Dabhi and A. M. Vora, *ACS Omega*, 2023, **8**, 43008–43023.

170 J. Li, Y. Jiang, Z. Zhang, M. Tsuji, M. Miyazaki, M. Kitano and H. Hosono, *Adv. Energy Mater.*, 2023, **13**, 2302424.

171 N. Li, Z. Wei, J. Zhao, Q. Wang, C. Shen, S. Wang, J. Tang, R. Yang, D. Shi and G. Zhang, *Adv. Mater. Interfaces*, 2019, **6**, 1802055.

172 W. Wan, Y. Li, X. Ren, Y. Zhao, F. Gao and H. Zhao, *Nanomaterials*, 2018, **8**, 112.

173 B. U. Haq, S. AlFaify, T. Alshahrani, R. Ahmed, F. K. Butt, S. U. Rehman and Z. Tariq, *Sol. Energy*, 2020, **211**, 920–927.

174 A. C. M. Padilha, M. Soares, E. R. Leite and A. Fazzio, *J. Phys. Chem. C*, 2019, **123**, 16359–16365.

175 W. Guo, H. Luo, D. Fang, Z. Jiang, J. Chi and W. Shangguan, *J. Energy Chem.*, 2022, **70**, 373–381.

176 P. V. Pham, S. C. Bodepudi, K. Shehzad, Y. Liu, Y. Xu, B. Yu and X. Duan, *Chem. Rev.*, 2022, **122**, 6514–6613.

177 D. M. Juraschek and P. Narang, *Nano Lett.*, 2021, **21**, 5098–5104.

178 K. Wang, Z. Huang, L. Xiong, K. Wang, Y. Bai, H. Long, N. Deng, B. Wang, G. Hu and P. Lu, *Optica*, 2025, **12**, 343–349.

179 J. Yang, J. Tang, M. B. Ghasemian, M. Mayyas, Q. V. Yu, L. H. Li and K. Kalantar-Zadeh, *ACS Photonics*, 2022, **9**, 905–913.

180 M. Chen, X. Lin, T. H. Dinh, Z. Zheng, J. Shen, Q. Ma, H. Chen, P. Jarillo-Herrero and S. Dai, *Nat. Mater.*, 2020, **19**, 1307–1311.

181 M. Dong, Y. Zhang, J. m. Cao, H. Chen, Q. Lu, H. f. Wang and J. Wu, *Adv. Sci.*, 2024, **11**, 2408329.

182 P. Qiao, Y. Zhang, J. Wang, Z. Peng, D. Wu, X. Chao, Z. Yang and P. Liang, *Ceram. Int.*, 2024, **50**, 2242–2248.

183 P. Shekhar, J. Atkinson and Z. Jacob, *Nano Convergence*, 2014, **1**, 14.

184 Y. Zhang, H. Wu, C. Wang, G. Yuan, L. Zou, Q. Wang, Q. J. Wang and Y. Luo, *Adv. Opt. Mater.*, 2025, 2500128.

185 J. Jiang, Z. Zheng, W. Huang, Z. Cao, N. Xu, H. Chen and S. Deng, *Nano Lett.*, 2025, **25**, 10953–10961.

186 T. D. Ngo, T. D. Dao, N. T. Cuong, N. Umezawa and T. Nagao, *Phys. Rev. Mater.*, 2020, **4**, 055201.

187 W. Lyu, H. Teng, C. Wu, X. Zhang, X. Guo, X. Yang and Q. Dai, *Nanoscale*, 2021, **13**, 12720–12726.

188 A. Yadav, R. Kumari, S. K. Varshney and B. Lahiri, *Opt. Express*, 2021, **29**, 33171–33183.

189 M. Liu, Z. Xue, C. Jiang, H. Zhu, S. Zhou, Y. Xiao, X. Wang, X. Xi, H. Teng and N. Chen, *Nanoscale*, 2025, **17**, 16333–16341.

190 F. Toffoletti and E. Collini, *Journal of Physics: Materials*, 2025, **8**, 022002.

191 F. Macheda, T. Sohier, P. Barone and F. Mauri, *Phys. Rev. B*, 2023, **107**, 094308.

192 C. Bhandari and W. R. L. Lambrecht, *Phys. Rev. B:Condens. Matter Mater. Phys.*, 2014, **89**, 045109.

193 D. N. Basov, M. M. Fogler and F. J. García de Abajo, *Science*, 2016, **354**, aag1992.

194 E. Abrahams, S. V. Kravchenko and M. P. Sarachik, *Rev. Mod. Phys.*, 2001, **73**, 251.

195 K. v. Klitzing, G. Dorda and M. Pepper, *Phys. Rev. Lett.*, 1980, **45**, 494.

196 R. Willett, J. P. Eisenstein, H. L. Störmer, D. C. Tsui, A. C. Gossard and J. H. English, *Phys. Rev. Lett.*, 1987, **59**, 1776.

197 Y. Kozuka, A. Tsukazaki, D. Maryenko, J. Falson, S. Akasaka, K. Nakahara, S. Nakamura, S. Awaji, K. Ueno and M. Kawasaki, *Phys. Rev. B:Condens. Matter Mater. Phys.*, 2011, **84**, 033304.

198 W.-B. Zhang, Q. Qu and K. Lai, *ACS Appl. Mater. Interfaces*, 2017, **9**, 1702–1709.

199 J. G. Labram, Y. H. Lin and T. D. Anthopoulos, *Small*, 2015, **11**, 5472–5482.

200 K. Nomura, H. Ohta, A. Takagi, T. Kamiya, M. Hirano and H. Hosono, *Nature*, 2004, **432**, 488–492.

201 E. Fortunato, P. Barquinha and R. Martins, *Adv. Mater.*, 2012, **24**, 2945–2986.

202 C. Wei Shih, A. Chin, C. Fu Lu and W. Fang Su, *Sci. Rep.*, 2016, **6**, 19023.

203 M. Osada and T. Sasaki, *Adv. Mater.*, 2012, **24**, 210–228.

204 G. D. Wilk, R. M. Wallace and J. M. Anthony, *J. Appl. Phys.*, 2001, **89**, 5243–5275.

205 R. M. Fleming, D. V. Lang, C. D. W. Jones, M. L. Steigerwald, D. W. Murphy, G. B. Alers, Y.-H. Wong, R. B. Van Dover, J. R. Kwo and A. M. Sergent, *J. Appl. Phys.*, 2000, **88**, 850–862.

206 D. I. Shahin, M. J. Tadjer, V. D. Wheeler, A. D. Koehler, T. J. Anderson, C. R. Eddy and A. Christou, *Appl. Phys. Lett.*, 2018, **112**, 042107.

207 K. Kukli, M. Ritala and M. Leskelä, *J. Electrochem. Soc.*, 2001, **148**, F35.

208 V. E. Henrich, *MRS Online Proc. Libr.*, 1999, **567**, 435–444.

209 M. Osada, Y. Ebina, H. Funakubo, S. Yokoyama, T. Kiguchi, K. Takada and T. Sasaki, *Adv. Mater.*, 2006, **18**, 1023–1027.

210 M. Depas, R. L. Van Meirhaeghe, W. H. Laflere and F. Cardon, *Solid-State Electron.*, 1994, **37**, 433–441.

211 D. Andres-Penares, M. Brotons-Gisbert, C. Bonato, J. F. Sánchez-Royo and B. D. Gerardot, *Appl. Phys. Lett.*, 2021, **119**, 223104.

212 S. K. Kim, W.-D. Kim, K.-M. Kim, C. S. Hwang and J. Jeong, *Appl. Phys. Lett.*, 2004, **85**, 4112–4114.

213 U. Diebold, *Surf. Sci. Rep.*, 2003, **48**, 53–229.

214 H. Sato, K. Ono, T. Sasaki and A. Yamagishi, *J. Phys. Chem. B*, 2003, **107**, 9824–9828.

215 M. Held, S. P. Schießl, D. Miehler, F. Gannott and J. Zaumseil, *Appl. Phys. Lett.*, 2015, **107**, 083301.

216 R. Ge, X. Wu, L. Liang, S. M. Hus, Y. Gu, E. Okogbue, H. Chou, J. Shi, Y. Zhang and S. K. Banerjee, *Adv. Mater.*, 2021, **33**, 2007792.

217 K. Zhang, J. Wang, Y. Huang, L.-Q. Chen, P. Ganesh and Y. Cao, *npj Comput. Mater.*, 2020, **6**, 198.

218 R. Ge, X. Wu, M. Kim, J. Shi, S. Sonde, L. Tao, Y. Zhang, J. C. Lee and D. Akinwande, *Nano Lett.*, 2018, **18**, 434–441.

219 X. Wu, R. Ge, P. A. Chen, H. Chou, Z. Zhang, Y. Zhang, S. Banerjee, M. H. Chiang, J. C. Lee and D. Akinwande, *Adv. Mater.*, 2019, **31**, 1806790.

220 A. Rana, C. Li, G. Koster and H. Hilgenkamp, *Sci. Rep.*, 2020, **10**, 3293.

221 J. Wang, F. Wang, L. Yin, M. G. Sendeku, Y. Zhang, R. Cheng, Z. Wang, N. Li, W. Huang and J. He, *Nanoscale*, 2019, **11**, 20497–20506.

222 M. K. Yang, J.-W. Park, T. K. Ko and J.-K. Lee, *Appl. Phys. Lett.*, 2009, **95**, 042105.

223 D. Miron, D. Cohen-Azarzar, B. Hoffer, M. Baskin, S. Kvatinsky, E. Yalon and L. Kornblum, *Appl. Phys. Lett.*, 2020, **116**, 223503.

224 J. R. Contreras, H. Kohlstedt, U. Poppe, R. Waser, C. Buchal and N. A. Pertsev, *Appl. Phys. Lett.*, 2003, **83**, 4595–4597.

225 Q. H. Qin, L. Äkäslompolo, N. Tuomisto, L. Yao, S. Majumdar, J. Vijayakumar, A. Casiraghi, S. Inkinen, B. Chen and A. Zugarramurdi, *Adv. Mater.*, 2016, **28**, 6852–6859.

226 G. Chen, C. Song, C. Chen, S. Gao, F. Zeng and F. Pan, *Adv. Mater.*, 2012, **24**, 3515–3520.

227 C. Huan, Z. Lu, S. Tang, Y. Cai and Q. Ke, *Sci. China:Phys., Mech. Astron.*, 2024, **67**, 227311.

228 M. Saxena, P. Roy, M. Acharya, I. Bose, K. Tanwar and T. Maiti, *Appl. Phys. Lett.*, 2016, **109**, 263903.

229 S. Walia, S. Balendhran, H. Nili, S. Zhuiykov, G. Rosengarten, Q. H. Wang, M. Bhaskaran, S. Sriram, M. S. Strano and K. Kalantar-zadeh, *Prog. Mater. Sci.*, 2013, **58**, 1443–1489.

230 Y. Liu, Y. H. Lin, B. P. Zhang, H. M. Zhu, C. W. Nan, J. Lan and J. F. Li, *J. Am. Ceram. Soc.*, 2009, **92**, 934–937.

231 J. He, Y. Liu and R. Funahashi, *J. Mater. Res.*, 2011, **26**, 1762–1772.

232 Y.-Q. Li, H. Shi, S.-B. Wang, Y.-T. Zhou, Z. Wen, X.-Y. Lang and Q. Jiang, *Nat. Commun.*, 2019, **10**, 4292.

233 H. Ohta, K. Sugiura and K. Koumoto, *Inorg. Chem.*, 2008, **47**, 8429–8436.

234 A. M. Haghiri-Gosnet, T. Arnal, R. Soulimane, M. Koubaa and J. P. Renard, *Phys. Status Solidi*, 2004, **201**, 1392–1397.

235 A. M. Nazmul, S. Sugahara and M. Tanaka, *Phys. Rev. B:Condens. Matter Mater. Phys.*, 2003, **67**, 241308.

236 Y. Ohno, D. K. Young, B. a. Beschoten, F. Matsukura, H. Ohno and D. D. Awschalom, *Nature*, 1999, **402**, 790–792.

237 D. J. Priour Jr, E. H. Hwang and S. D. Sarma, *Phys. Rev. Lett.*, 2005, **95**, 037201.

238 K. Fujiwara, Y. Fukuma, J. Matsuno, H. Idzuchi, Y. Niimi, Y. Otani and H. Takagi, *Nat. Commun.*, 2013, **4**, 2893.

239 M. Julliere, *Phys. Lett. A*, 1975, **54**, 225–226.

240 A. Gupta, X. Li and G. Xiao, *Appl. Phys. Lett.*, 2001, **78**, 1894–1896.

241 A. Gupta and J. Z. Sun, *J. Magn. Magn. Mater.*, 1999, **200**, 24–43.

242 Z. Ma, P. Yan, W. Liu, W. Wu, Q. Tian, G. Chen and Q. Xu, *J. Phys. Chem. C*, 2025, **129**, 9903–9911.

243 S. Dey, V. Mishra, N. Dhakar, S. Kumar, P. Srivastava and S. Ghosh, *J. Alloys Compd.*, 2024, **980**, 173650.

244 T. Miyazaki and N. Tezuka, *J. Magn. Magn. Mater.*, 1995, **139**, L231–L234.

245 P. M. Tedrow and R. Meservey, *Phys. Rev. B*, 1973, **7**, 318.

246 R. K. Shivade, A. Kundu and B. Chakraborty, *Chem. Phys. Lett.*, 2021, **762**, 138075.

247 W. Zhang, M. Zheng, Y. Liu, R. Xiong, C. Zuo, M. Chen, Z. Zhang and Z. Lu, *J. Phys. D: Appl. Phys.*, 2025, **58**, 405002.

248 R. Chen, F. Luo, Y. Liu, Y. Song, Y. Dong, S. Wu, J. Cao, F. Yang, A. N'Diaye and P. Shafer, *Nat. Commun.*, 2021, **12**, 3952.

249 M. Fonin, Y. S. Dedkov, R. Pentcheva, U. Rüdiger and G. Güntherodt, *J. Phys.: Condens. Matter*, 2007, **19**, 315217.

250 M.-H. Jo, N. D. Mathur, N. K. Todd and M. G. Blamire, *Phys. Rev. B:Condens. Matter Mater. Phys.*, 2000, **61**, R14905.

251 M. Uehara, S. Mori, C. H. Chen and S.-W. Cheong, *Nature*, 1999, **399**, 560–563.

252 J. S. Moodera, L. R. Kinder, T. M. Wong and R. Meservey, *Phys. Rev. Lett.*, 1995, **74**, 3273.

253 T. Dietl, H. Ohno and F. Matsukura, *Phys. Rev. B:Condens. Matter Mater. Phys.*, 2001, **63**, 195205.

254 C. Timm, *J. Phys.: Condens. Matter*, 2003, **15**, R1865.

255 S. Yang, C. Jiang and S.-h. Wei, *Appl. Phys. Rev.*, 2017, **4**, 021304.

256 A. Verma and B. C. Yadav, *ACS Appl. Nano Mater.*, 2023, **6**, 5493–5507.

257 M. Gupta, P. Chaudhary, A. Singh, A. Verma, D. Yadav and B. C. Yadav, *Sens. Actuators, B*, 2022, **368**, 132102.

258 M. Mathur, A. Verma, A. Singh, B. C. Yadav and V. Chaudhary, *Environ. Res.*, 2023, **229**, 115931.

259 A. Verma, D. Yadav, A. Singh, M. Gupta, K. B. Thapa and B. C. Yadav, *Sens. Actuators, B*, 2022, **361**, 131708.

260 S. S. Shendage, V. L. Patil, S. A. Vanalakar, S. P. Patil, N. S. Harale, J. Bhosale, J. H. Kim and P. S. Patil, *Sens. Actuators, B*, 2017, **240**, 426–433.

261 H.-J. Kim and J.-H. Lee, *Sens. Actuators, B*, 2014, **192**, 607–627.

262 C. Huan, P. Wang, B. He, Y. Cai and Q. Ke, *J. Mater. Chem. C*, 2022, **10**, 1839–1849.

263 S. Kanaparthi and S. Govind Singh, *Mater. Sci. Energy Technol.*, 2020, **3**, 91–96.

264 D. Fu, C. Zhu, X. Zhang, C. Li and Y. Chen, *J. Mater. Chem. A*, 2016, **4**, 1390–1398.

265 M. Breedon, P. Spizzirri, M. Taylor, J. Du Plessis, D. McCulloch, J. Zhu, L. Yu, Z. Hu, C. Rix and W. Wlodarski, *Cryst. Growth Des.*, 2010, **10**, 430–439.

266 M. M. Alsaif, S. Balendhran, M. R. Field, K. Latham, W. Wlodarski, J. Z. Ou and K. Kalantar-Zadeh, *Sens. Actuators, B*, 2014, **192**, 196–204.

267 X. Liu, Y. Sun, M. Yu, Y. Yin, B. Du, W. Tang, T. Jiang, B. Yang, W. Cao and M. N. R. Ashfold, *Sens. Actuators, B*, 2018, **255**, 3384–3390.

268 X. Liang, S. Yu, B. Meng, Y. Ju, S. Wang and Y. Wang, *Nanomaterials*, 2025, **15**, 948.

269 S. Das, H. Mazumdar, K. R. Khondakar and A. Kaushik, *ACS Appl. Nano Mater.*, 2024, **7**, 13893–13918.

270 B. Kaduk, T. Kowalczyk and T. Van Voorhis, *Chem. Rev.*, 2012, **112**, 321–370.

271 A. Jain, S. P. Ong, G. Hautier, W. Chen, W. D. Richards, S. Dacek, S. Cholia, D. Gunter, D. Skinner, G. Ceder and K. A. Persson, *APL Mater.*, 2013, **1**.

272 S. Curtarolo, W. Setyawan, S. Wang, J. Xue, K. Yang, R. H. Taylor, L. J. Nelson, G. L. W. Hart, S. Sanvito, M. Buongiorno-Nardelli, N. Mingo and O. Levy, *Comput. Mater. Sci.*, 2012, **58**, 227–235.

273 K. Choudhary, *Comput. Mater. Sci.*, 2025, **259**, 114063.

274 C. Ezeakunne, B. Lamichhane and S. Kattel, *Phys. Chem. Chem. Phys.*, 2025, **27**, 5338–5358.

275 T. Wang, X. Tan, Y. Wei and H. Jin, *Mater. Today Commun.*, 2021, **29**, 102932.

276 E. Pavoni, M. G. Modreanu, E. Mohebbi, D. Mencarelli, P. Stipa, E. Laudadio and L. Pierantoni, *Nanomaterials*, 2023, **13**, 1319.

277 S. Correal, D. Hernández-Gómez, A. S. Esquivel, A. Cardona-Rodríguez, A. Reiber, Y. Hernandez, R. González-Hernández and J. G. Ramírez, *Sci. Rep.*, 2023, **13**, 6752.

278 H. Park, Z. Li and A. Walsh, *Matter*, 2024, **7**, 2355–2367.

279 D. Menon and R. Ranganathan, *ACS Omega*, 2022, **7**, 25958–25973.

280 E. J. Gurniak, S. Yuan, X. Ren and P. S. Branicio, *Comput. Mater. Sci.*, 2024, **244**, 113257.

281 W. Wei, G. Min, Q. Fan, D. Liang, M. Ye and S. Yun, *Vacuum*, 2025, **231**, 113732.

282 J. Taboada-Gutiérrez, Y. Zhou, A. I. Tresguerres-Mata, C. Lanza, A. Martínez-Suárez, G. Álvarez-Pérez, J. Duan, J. I. Martín, M. Vélez and I. Prieto, *ACS Photonics*, 2024, **11**, 3570–3577.

283 C. Schäfer, J. Fojt, E. Lindgren and P. Erhart, *J. Am. Chem. Soc.*, 2024, **146**, 5402–5413.

284 H. Wahab, J. Heil, A. S. Tyrrell, T. Muller, J. Ackerman, L. Kotthoff and P. A. Johnson, *Ceram. Int.*, 2024, **50**, 9114–9124.

285 H. Xu, R. Nakayama, T. Kimura, R. Shimizu, Y. Ando, S. Kobayashi, N. Yasuo, M. Sekijima and T. Hitosugi, *Sci. Technol. Adv. Mater.:Methods*, 2023, **3**, 2210251.

286 T. K. Patra, F. Zhang, D. S. Schulman, H. Chan, M. J. Cherukara, M. Terrones, S. Das, B. Narayanan and S. K. R. S. Sankaranarayanan, *ACS Nano*, 2018, **12**, 8006–8016.

287 G. P. Wellawatte and P. Schwaller, *Commun. Chem.*, 2025, **8**, 11.

288 P. Friederich, M. Krenn, I. Tamblyn and A. Aspuru-Guzik, *Machine Learning: Science and Technology*, 2021, **2**, 025027.

289 T. Biswas, A. Gupta and A. K. Singh, *RSC Adv.*, 2025, **15**, 8253–8261.

© 2026 The Author(s). Published by the Royal Society of Chemistry